Simulation of Soot Formation in Turbulent Diffusion Flames Using Conditional Source-term Estimation

by

Seyed Mehdi Ashrafizadeh

A thesis
presented to the University of Waterloo
in fulfillment of the
thesis requirement for the degree of
Doctor of Philosophy
in
Mechanical and Mechatronics Engineering

Waterloo, Ontario, Canada, 2022

Examining Committee Membership

The following served on the Examining Committee for this thesis. The decision of the Examining Committee is by majority vote.

External Examiner:	Fengshan Liu Senior Research Officer, Black Carbon Metrology, Metrology Research Centre, National Research Council Canada
Supervisor(s):	Cecile B. Devaud Professor, Mechanical and Mechatronics Engineering, University of Waterloo
Internal Member:	Fue-Sang Lien Professor, Mechanical and Mechatronics Engineering, University of Waterloo
Internal Member:	John Wen Professor, Mechanical and Mechatronics Engineering, University of Waterloo
Internal-External Member:	Francis Poulin Professor, Applied Mathematics, University of Waterloo

Author's Declaration

I hereby declare that I am the sole author of this thesis. This is a true copy of the thesis, including any required final revisions, as accepted by my examiners.

I understand that my thesis may be made electronically available to the public.

Abstract

Conditional Source-term Estimation (CSE) is a turbulent combustion model which uses the conditional averages of scalars for calculating the mean reaction source term in the species transport equation. CSE has been shown to be a very efficient and accurate method for simulating turbulent flames without being limited to certain conditions and regimes.
In this study, for the first time, CSE is used for the simulation of soot formation in turbulent diffusion flames. The objective of the present research is to develop a CSE code for simulating soot formation in turbulent diffusion flames. The modeling of soot formation is investigated for two turbulent flames, at atmospheric and 3 atm pressure conditions. A semi-empirical soot formulation that accounts for soot inception, coagulation, surface growth, and oxidation processes is coupled with the CSE turbulent combustion model using Reynolds Averaged Navier Stokes equations. Detailed chemistry is included and an optically thin radiation model is considered. Good agreement with the experiments is found for turbulent mixing and temperature fields in both flames, with some discrepancies believed to be due to the turbulence model. The predicted soot volume fraction values match the experimental data well at 1 atm with some under prediction in the range of experimental uncertainty. At higher pressure, the predicted level of soot increases, as expected. At 3 atm, underpredictions can be noticed in the predicted soot volume fraction.
In the current work, the CSE framework is extended to include the effect of radiation in the chemistry tables and to have better predictions for species mass fractions and reaction rates. This is applied to the turbulent methane-air flame at 3 atm pressure and significant improvements are observed for the temperature and soot predictions.
A detailed soot model that takes into account the soot aerosol dynamics, the Quadrature based Method of Moments (QMOM) is added to the CSE code as an advanced model after promising results were observed from the semi-empirical soot model. The CSE-QMOM method is applied to an ethylene turbulent flame. The results show very good predictions of soot volume fraction.
Finally, a Poly cyclic Aromatic Hydrocarbon (PAH) based model is implemented into the CSE-soot framework. PAH based inception models are known to provide more accurate predictions compared to the conventional acetylene based models. The CSE-soot model is capable of providing good predictions for soot volume fraction. Possible sources of discrepancies and limitations of the model are discussed and future improvements are explained.

Acknowledgements

First I would like to express my profound appreciation and sincere gratitude to my supervisor Prof. Cecile Devaud for her guidance and counsel throughout my years of study and work at the University of Waterloo. I am very grateful for her patience, support and advice.

I would like to thank my committee members: Prof. Fengshan Liu, Prof. Fue-Sang Lien, Prof. John Wen and Prof. Francis Poulin for consenting to be members of the thesis committee and for reading and commenting on this thesis. The financial support of the Natural Science and Engineering Research Council of Canada (NSERC) and Pratt and Whitney Canada (P&WC) is gratefully acknowledged. Also Compute Canada is acknowledged for providing the computational resources that are used in the present work. I would like to thank all my colleagues at the turbulent combustion modelling lab for their valuable support, especially Mohammad Mortada, Daniel Wilson, Ahmed Hussien, Samaneh Zareian, Alexandra McGowen, and Ahmed Abdalhamid. I also like to thank my friends from the University of Waterloo, especially Seyed Hossein Mirjahanmardi, Amir Yazdanmehr, Hamed Shahrokhi, and Hamed Jamshidifar for their sincere friendship. Also, I would like to thank my friends Amir Atoufi and Hamid Mirzaei for the great scientific disccusions we had during our graduate courses. I would like to thank Prof. Clinton Groth and Jacques Xing for their help and the fruitful sharing of experience and the knowledge of QMOM.

Finally, I would like to thank my parents and brother whose endless love, kindness and sacrifice enabled all my life achivements. Their inspiring compassion, support, and encouragement can not be described or thanked in words.

Last but not the least, I would like to thank the love of my life, Maedeh, for her love, sacrifice, patience, and endless support throughout these years. The greatest gifts that I was blessed with during my Ph.D. were my daughter, Noura, and my son, Sadra. I also thank them for bringing sweetness to my life.

Dedication

This work is dedicated to my family.

Table of Contents

List of Figures

List of Tables

Chapter 1

Introduction

1.1 Motivation

Increasing demand for energy in the world has motivated many researchers to work in the field of energy conversion. Energy demand is expected to increase from 12.5 Giga tons of oil equivalents (GTOE) in 2015 to 25 GTOE by 2035 [1]. There have been considerable developments in the application of renewable energy resources. However, combustion of fossil fuels is still the main source of energy in the foreseeable future. As reported in the International Energy Outlook [2], it is estimated that fossil fuels will continue to supply approximately 80% of the world's energy until 2040. Oil will continue to play an important role in the future of energy, even though substantial resources have been devoted to increasing the use of renewable sources of energy in recent years [3]. The fossil fuels account for about 86% of the worldwide primary energy demand which is increasing gradually. At present, oil, gas, coal, renewable and alternative energy resources have a portion of 36%, 27%, 23% and 14%, respectively, in the global energy consumption statistics [1]. While solar, wind, geothermal, biomass and hydroelectric have a share of 8% and nuclear power only has a fragment of 6%. One of the drawbacks of combustion systems is that they have a negative impact on the environment due to the pollutants produced in combustion such as carbon monoxide (CO), nitric oxides (NO_x), and particulate matters. Solid carbon particulate matters are emitted during combustion of hydrocarbon fuels in the form of smoke or soot, if these solid matters are not fully oxidized during combustion. Soot formation is one of the most complex and yet, not well comprehended phenomena in combustion. Depending on the application, soot formation can be detrimental or advantageous. The carbonaceous particulate matter has carcinogenic effects and can cause respiratory system

diseases [4, 5]. Further, after carbon dioxide (CO_2), soot is considered to be the leading cause of climate change [6]. Soot alters the radiative properties of the atmosphere due to their strongly light absorbing ability, i.e., they absorb more UV and visible radiation from the sun than they reflect solar radiation back to space. Furthermore, the deposition of soot on snow and ice reduces the reflection of sunlight and causes further global warming [7]. Additionally, soot particles can damage combustion devices. Soot can deposit on the combustion chambers and turbine blades of jet engines and damage them. Black soot particles can accumulate on the surface of combustors or components of engines, increasing the thermal load of these parts and as a result, reduce the service life of these components. Due to the negative impacts of soot mentioned above, designers are doing their best to avoid soot emission.

However, soot is not always an unwanted byproduct of combustion. Soot formation in flames has a positive role in enhancing the radiative heat transfer. Increasing radiative heat transfer is beneficial for furnaces, heat generators and boilers, which aim to transfer heat from the flame to the furnace walls. Further, sometimes soot is deliberately produced in the form of carbon black that is widely used as filler for elastomers, in tire manufacturing, and in toners for photocopy machines and laser printers [8].

Combustion processes are commonly divided into two categories depending on how the fuel and oxidizer are mixed: premixed and non-premixed combustion. A premixed flame is found when the fuel and oxidizer are mixed before reaction occurs, while a non-premixed flame is present when the fuel and oxidizer are not mixed prior to reacting and both fuel and air enter the combustion zone separately. Non-premixed flames are also called diffusion flames since mixing of fuel and oxidizer occurs simultaneously with combustion, making diffusion the rate-controlling process. Turbulent non-premixed flames appear in many industrial applications such as furnaces, diesel engines and gas turbines. In a gas turbine or jet engine, the fuel is sprayed in the compressed hot air inside the combustion chamber leading to ignition. Ignition will typically occur when the local mixture is still rich. This will inevitably lead to soot formation. Therefore, soot formation in gas turbines and aircraft jet engines is an important issue and manufacturers are attempting to improve their designs and reduce the amount of soot produced.

In recent years, due to the increasingly stringent regulations for pollutant emissions, designing efficient aircraft jet engines which consume less fuel and produce less pollutants, in particular soot, has become necessary. The design process is iterative and requires numerous tests and building various prototypes. In order to lower the design costs, numerical simulations are employed in the design process to reduce the number of expensive experimental tests. In most industrial combustion devices where the flow is turbulent, numerical modelling of turbulent combustion flows has demonstrated to be an effective approach towards providing detailed information about the process and the flow field [9].

Soot formation and oxidation are complex processes, involving a large number of chemical reactions and other physical processes such as coagulation and agglomeration some of which are not well understood. The most comprehensive soot models presented, attempt to describe all of these effects. These detailed models are able to predict soot in laminar flames with high accuracy but at the same time require high computational cost [10, 11]. In order to use these detailed models in turbulent combustion flames the computational costs increase significantly and in some cases, due to the computational resource limits, the utilization of the model becomes unfeasible. Many approaches to soot modelling exist, but there is always a trade off between the amount of details provided by the soot model and the computational costs. Therefore, the need for further development of effective soot modelling approaches exist which can predict soot at a good level of accuracy and at the same time have reasonable computational costs.

1.2 Objectives

The current work aims to extend a conditional source-term estimation (CSE) formulation, to be capable of simulating soot formation in turbulent flames.

Conditional Source-term Estimation (CSE) is a turbulent combustion model (further details will be given in Chapter 2) which has been shown to perform well in many turbulent combustion simulations [12, 13, 14]. In contrast to other turbulent combustion models that are restricted to specific types of flows or are very complex, the CSE method can be used for any type of turbulent flame with a relatively simple formulation. Until now, CSE has only been applied to simple hydrocarbon fuels, methane and methanol, without considering soot formation.
The focus of the proposed research is to investigate different soot models with the CSE approach in turbulent combustion simulations. The main objectives of the present study are as follows:

1. **Extension of the pre-existing CSE framework for soot formation modelling and implementation of a semi-empirical two-equation soot model into the CSE turbulent combustion code**: The first major objective of the present research is to develop a CSE code to take into account soot formation in turbulent non-premixed flames. A semi-empirical two-equation soot model will be added to the CSE code in order to predict the amount of soot produced in the flame and compared to the experimental data.

2. **Investigation of CSE-Semi empirical soot model applied to turbulent diffusion flames**: The Brookes and Moss burner with methane-air turbulent non-premixed flame at atmospheric pressure is selected [15]. Before performing any soot simulations, the CSE simulation of a turbulent non-premixed methane-air flame [16, 15] without soot is revisited. Soot formation simulation using CSE approach coupled with a well known semi-empirical soot model with detailed chemistry is done for the selected flame. The numerical predictions are compared with experimental data and the sources of discrepancies are explained. In addition, the effect of some parameters in the soot model are investigated and discussed. In addition, The Brookes and Moss flame at 3 atm pressure is selected [15]. The flame structure, temperature, and soot levels are predicted and compared with the 1 atm burner to obtain the effect of pressure on soot formation levels in turbulent diffusion flames.

3. **Implementation of a detailed soot model into the CSE framework**: After implementing a semi-empirical soot model into the CSE framework, a detailed soot model is coupled with the CSE solver. For this purpose, a quadrature method of moments (QMOM) which is responsible for the solution of particle dynamics and the population balance equation is selected. To test the performance of this method, another turbulent flame that has higher levels of soot formation is selected. Hence, the Sandia ethylene turbulent burner [17] is chosen and numerical predictions are compared with the available experimental data.

The proposed research is expected to make a significant contribution to the turbulent combustion field as well as the soot modelling field as CSE has never been used for soot modelling simulations. The developed method may be used in the future to predict and reduce soot formation for the design of new gas turbines and engines.

1.3 Overview of the study

In Chapter 2, background information is presented including a description of the governing equations that are used in the current study. The different turbulence modelling approaches and the turbulent combustion modelling strategies are described. A review of soot formation and different approaches for soot modelling are explained. Previous investigations of soot formation modelling in turbulent diffusion flames are summarized.
Chapter 3 provides a detailed description for the CSE combustion model coupled with a semi-empirical soot model, that includes its basic concepts and assumptions, the mathematical formulation and how the semi-empirical soot model is implemented in the numerical

code. In addition, the behaviour of the model is investigated and the predicted levels of soot are compared with experimental data.
Chapter 4 outlines the RANS simulations carried out for the turbulent methane-air flame (Brookes and Moss burner), using the non-adiabatic chemistry tables that take into account the effects of temperature loss due to radiation. The method for generating the non-adiabatic chemical kinetic tables are explained and the numerical predictions are presented and compared with adiabatic results.
In Chapter 5, the quadrature method of moments for solving the population balance equation of a disperse particle systems such as soot is described and the details for the implementation are explained. The results of soot volume fraction obtained from this detailed method are compared with the predictions from the semi-empirical soot model.
Chapter 6 describes another step forward towards a detailed soot modelling. In this chapter, a soot nucleation model that includes poly-cyclic aromatic hydrocarbons (PAHs) as the soot formation precursors are included rather than the simple acetylene based models.
Finally, Chapter 7 summarizes the general conclusions of the present dissertation and the suggestions for future work are presented.

1.4 Author's current contributions

It is acknowledged that parts of the content presented in chapter 3-5 are published in the following articles

- S. M. Ashrafizadeh and C. Devaud. Investigation of Conditional Source-term Estimation coupled with a semi-empirical model for soot predictions in two turbulent flames. Combustion Theory and Modelling, submitted, under review, 2022.
- S. M. Ashrafizadeh, J. Xing, C. Devaud, and C. Groth. Investigation of Conditional Source-term Estimation coupled with a Quadrature Method of Moments (QMOM) model for soot predictions in a non-premixed turbulent ethylene flame. Under preparation.

Chapter 2

Background and literature review

In this chapter, several background topics are discussed, including the governing equations, the turbulence approaches, and the modeling strategies employed to model turbulent combustion. This is followed by a review on soot modelling approaches, as well as a summary of previous investigations for modelling soot formation in turbulent diffusion flames.

2.1 Governing equations

The governing transport equations of mass, momentum, enthalpy (energy) and species mass fractions for simulating turbulent flames are given as

- Conservation of mass

$$\frac{\partial \rho}{\partial t} + \frac{\partial}{\partial x_i}(\rho u_i) = 0, \tag{2.1}$$

where ρ is the density, t time, x_i spatial components and u_i the velocity components for $i = 1$ to 3 in different spatial directions.

- Conservation of momentum (Navier-Stokes equations)

$$\frac{\partial(\rho u_j)}{\partial t} + \frac{\partial(\rho u_i u_j)}{\partial x_i} = -\frac{\partial p}{\partial x_j} + \frac{\partial \tau_{ij}}{\partial x_i} + \rho \sum_{k=1}^{N} Y_k f_{k,j}, \tag{2.2}$$

where p is the pressure, τ_{ij} the viscous stress tensor, Y_k the mass fraction of species k and $f_{k,j}$ the body force in the j direction acting on species k.
The viscous stress tensor, for Newtonian fluids, is expressed as

$$\tau_{ij} = -\frac{2}{3}\mu\frac{\partial u_k}{\partial x_k}\delta_{ij} + \mu\left(\frac{\partial u_i}{\partial x_j} + \frac{\partial u_j}{\partial x_i}\right), \tag{2.3}$$

where μ is the dynamic viscosity and δ_{ij} is the Kronecker's delta.

- The energy equation, given in the form of sensible enthalpy (h_s)

$$\frac{\partial}{\partial t}(\rho h_s) + \frac{\partial}{\partial x_i}(\rho u_i h_s) = \frac{Dp}{Dt} + \tau_{ij}\frac{\partial u_i}{\partial x_j} - \frac{\partial q_i}{\partial x_i} + \dot{Q}_{rad} + \rho\sum_{k=1}^{N} Y_k f_{k,i} V_{k,i}, \tag{2.4}$$

where q_i the energy flux, $\tau_{ij}\frac{\partial u_i}{\partial x_i}$ is the source responsible for friction, the term $\rho\sum_{k=1}^{N} Y_k f_{k,i} V_{k,i}$ is the power generated by volume forces f_k on species k, and $\dot{Q}_{rad}$ the heat source term due to radiation [18].

The sensible enthalpy for a mixture of N species, is given as

$$h_s = \sum_{k=1}^{N} h_{sk} Y_k, \tag{2.5}$$

- The conservation of species k

$$\frac{\partial}{\partial t}(\rho Y_k) + \frac{\partial}{\partial x_i}(\rho u_i Y_k) = -\frac{\partial}{\partial x_i}(\rho V_{k,i} Y_k) + \dot{\omega}_k \qquad k = 1, N, \tag{2.6}$$

where $V_{k,i}$ is the i-component of the diffusion velocity V_k of species k, and $\dot{\omega}_k$ the reaction rate of species k [18].

2.2 Favre-averaged transport equations in RANS

In RANS, the transport equations are averaged to obtain the mean and fluctuating values of the variables of interest (e.g. velocity, species mass fraction, temperature). In RANS,

unclosed terms appear in the governing equations that need closure. For reactive flows, where large variations in density exist, Favre-averaged or density-weighted quantities are used to avoid additional unclosed terms generated in Reynolds averaging.
For any quantity ϕ, the Favre-averaged value of ϕ is calculated as

$$\widetilde{\phi} = \frac{\overline{\rho\phi}}{\overline{\rho}}, \tag{2.7}$$

and the fluctuations of this Favre-averaged quantity are defined as

$$\phi'' = \phi - \widetilde{\phi}. \tag{2.8}$$

The Favre-averaged conservation equations of gas-phase mass, momentum, species, and sensible enthalpy for reactive flows are given by

- Conservation of mass

$$\frac{\partial \overline{\rho}}{\partial t} + \frac{\partial}{\partial x_i}(\overline{\rho}\widetilde{u_i}) = 0, \tag{2.9}$$

- Conservation of momentum

$$\frac{\partial \overline{\rho}\widetilde{u_i}}{\partial t} + \frac{\partial}{\partial x_i}(\overline{\rho}\widetilde{u_i}\widetilde{u_j}) + \frac{\partial \overline{p}}{\partial x_j} = \frac{\partial}{\partial x_i}\Big(\overline{\tau}_{ij} - \overline{\rho}\widetilde{u_i'' u_j''}\Big), \tag{2.10}$$

- Conservation of species mass fractions

$$\frac{\partial \overline{\rho}\widetilde{Y_k}}{\partial t} + \frac{\partial}{\partial x_i}(\overline{\rho}\widetilde{u_j}\widetilde{Y_k}) = \overline{\frac{\partial}{\partial x_i}\rho D_k \frac{\partial Y_k}{\partial x_i}} - \frac{\partial}{\partial x_i}\Big(\overline{\rho}\widetilde{u_i'' Y_k''}\Big) + \overline{\dot{\omega}_k}, \tag{2.11}$$

- Sensible enthalpy equation

$$\begin{aligned}\frac{\partial \overline{\rho}\widetilde{h_s}}{\partial t} + \frac{\partial}{\partial x_i}(\overline{\rho}\widetilde{u_i}\widetilde{h_s}) = \frac{\partial}{\partial x_i}\Big(\overline{\lambda\frac{\partial T}{\partial x_i}} - \overline{\rho}\widetilde{u_i'' h_s''}\Big) \\ + \overline{\tau_{ij}\frac{\partial u_i}{\partial x_j}} + \overline{\dot{q}}_{react} + \overline{\dot{Q}_{rad}},\end{aligned} \tag{2.12}$$

where ρ is the density, u_i is the i-th component of velocity, p is the pressure, τ_{ij} viscous stress tensor, Y_k mass fraction of species k, D_k diffusion coefficient of species k, $\dot{\omega}_k$ chemical

reaction rate of species k, h_s sensible enthalpy, λ the thermal conductivity, $\overline{\dot{q}}_{react}$ the chemical source term of the sensible enthalpy equation, and $\dot{Q}_{rad}$ the radiation source term. The Reynolds stresses $-\overline{\rho}\widetilde{u_i'' u_j''}$ are modelled by the eddy viscosity concept such that

$$-\widetilde{u_i'' u_j''} = \nu_t\Big(\frac{\partial \widetilde{u}_i}{\partial x_j} + \frac{\partial \widetilde{u}_j}{\partial x_i}\Big) - \frac{2}{3}k\delta_{ij}, \tag{2.13}$$

where ν_t is the turbulence eddy viscosity, and k the turbulent kinetic energy. As can be seen in Eqs. (2.9 - 2.12), unclosed terms in the governing transport equations exist that are modeled using different methods. The $k-\varepsilon$ model [19], is used to close the Reynolds stresses, $\widetilde{u_i'' u_j''}$. For the unclosed terms $\overline{\rho}\widetilde{u_i'' Y_k''}$ and $\overline{\rho}\widetilde{u_i'' h_t''}$, in the species and energy transport equations respectively, a gradient assumption is often used. Using the gradient assumption these terms are modeled as

$$\overline{\rho}\widetilde{u_i'' Y_k''} = -\frac{\mu_t}{Sc_t}\frac{\partial \tilde{Y}_k}{\partial x_k} \qquad and \qquad \overline{\rho}\widetilde{u_i'' h_t''} = -\frac{\mu_t}{Pr_t}\frac{\partial \tilde{h}_t}{\partial x_k}, \tag{2.14}$$

where μ_t is the turbulent viscosity, Sc_t the turbulent Schmidt number and Pr_t the turbulent Prandtl number. Assuming unity Lewis number, the turbulent Schmidt number and the turbulent Prandtl number are set to be equal. The laminar diffusion flux, $\overline{\lambda\frac{\partial T}{\partial x_i}}$, and the first term in the right hand side (RHS) of Eq. 2.11 are omitted, as commonly applied in turbulent combustion due to the assumption that at high Reynolds numbers these terms are negligible. Finally, the mean chemical source-term $\overline{\dot{\omega}_k}$, in Eq. 2.11, is closed using turbulent combustion modelling which will be explained in detail in the next section. The mixture fraction is commonly used in turbulent combustion modelling to characterise the turbulent mixing process. It is defined to have a value of unity in pure fuel and zero in pure oxidiser. The Favre-averaged equations of mixture fraction mean and variance are given by

$$\frac{\partial}{\partial t}(\overline{\rho}\widetilde{Z}) + \frac{\partial}{\partial x_i}(\overline{\rho}\widetilde{u}_i\widetilde{Z}) = \frac{\partial}{\partial x_i}\Big(\overline{\rho D\frac{\partial Z}{\partial x_i}}\Big) - \frac{\partial}{\partial x_i}(\overline{\rho}\widetilde{u_i'' Z''}), \tag{2.15}$$

$$\frac{\partial}{\partial t}(\overline{\rho}\widetilde{Z''^2}) + \frac{\partial}{\partial x_i}(\overline{\rho}\widetilde{u}_i\widetilde{Z''^2}) = \frac{\partial}{\partial x_i}\Big(\overline{\rho D\frac{\partial Z''^2}{\partial x_i}}\Big) - \frac{\partial}{\partial x_i}(\overline{\rho}\widetilde{u_i'' Z''^2}) - 2\overline{\rho}\widetilde{u_i'' Z''} - \overline{\rho}\widetilde{\chi}. \tag{2.16}$$

where Z is the mixture fraction, and Z''^2 the mixture fraction variance. The turbulent flux $\widetilde{u_i'' Z''}$, is closed using the gradient assumption. The mean scalar dissipation rate, $\widetilde{\chi}$, is approximated to be equal to $2\frac{\varepsilon}{k}\widetilde{Z''^2}$, where k is the turbulent kinetic energy and ε the dissipation rate of k.

2.2.1 k-ε turbulence model

One of the most popular and widely used models for turbulence modelling is the k-ε model [19]. In this model, the turbulent viscosity is calculated as

$$\mu_t = \overline{\rho} C_\mu \frac{k^2}{\varepsilon}, \tag{2.17}$$

where k and ε are described by the two transport equations

$$\frac{\partial}{\partial t}(\overline{\rho}k) + \frac{\partial}{\partial x_i}(\overline{\rho}\widetilde{u}_i k) = \frac{\partial}{\partial x_i}\left[(\mu + \frac{\mu_t}{\sigma_k})\frac{\partial k}{\partial x_i}\right] + P_k - \overline{\rho}\varepsilon, \tag{2.18}$$

$$\frac{\partial}{\partial t}(\overline{\rho}\varepsilon) + \frac{\partial}{\partial x_i}(\overline{\rho}\widetilde{u}_i \varepsilon) = \frac{\partial}{\partial x_i}\left[(\mu + \frac{\mu_t}{\sigma_\varepsilon})\frac{\partial \varepsilon}{\partial x_i}\right] + C_{\varepsilon 1}\frac{\varepsilon}{k}P_k - C_{\varepsilon 2}\overline{\rho}\frac{\varepsilon^2}{k}, \tag{2.19}$$

The default model constants C_μ, σ_k, σ_ε, $C_{\varepsilon 1}$ and $C_{\varepsilon 2}$ are 0.09, 1.0, 1.3, 1.44 and 1.92, respectively. The source term P_k is calculated as

$$P_k = -\overline{\rho}\widetilde{u_i'' u_j''}\frac{\partial \widetilde{u}_i}{\partial x_j}, \tag{2.20}$$

where Reynolds stress term is obtained by Boussinesq approximation, which assumes the turbulent stresses are related to the mean velocity gradients as

$$\overline{\rho}\widetilde{u_i'' u_j''} = -\mu_t\left(\frac{\partial \widetilde{u}_i}{\partial x_j} + \frac{\partial \widetilde{u}_j}{\partial x_i} - \frac{2}{3}\delta_{ij}\frac{\partial \widetilde{u}_k}{\partial x_k}\right) + \frac{2}{3}\overline{\rho}k, \tag{2.21}$$

where the turbulent kinetic energy (TKE) is obtained by

$$k = \frac{1}{2}\sum_{k=1}^{3}\widetilde{u_k'' u_k''}. \tag{2.22}$$

2.3 Turbulent combustion models

In turbulent combustion, a broad range of length and time scales exist, also different processes control combustion and all these processes have interactions with each other across all scales. Therefore, making it a challenge for combustion to be modeled especially when interaction of turbulence and chemistry exists. In addition, in the RANS averaging process, the Favre-averaged species transport equation produces an unclosed term representing the

mean chemical source-term [20]. According to Arrhenius law [18], the reaction rate of fuel $\dot{\omega}_F$ can be obtained by

$$\dot{\omega}_F = -A\rho^2 T^{\beta} Y_F Y_O e^{\frac{-T_A}{T}}, \tag{2.23}$$

where A is the pre-exponential constant, β the temperature exponent, Y_F fuel mass fraction, Y_O oxidizer mass fraction and T_A the activation temperature. The mean reaction rates cannot by calculated from the averaged scalars because of the nonlinearity of Eq. 2.23. This means that

$$\overline{\dot{\omega}(\rho, T, Y_k)} \neq \dot{\omega}(\overline{\rho}, \overline{T}, \overline{Y_k}), \tag{2.24}$$

because the fluctuations in the scalars can be very significant in turbulent combustion problems leading to large deviations in the reaction rate. The modeling of the mean chemical source term has often been the main problem in turbulent combustion. To understand the difficulties associated with the closure of this term, it can be assumed that coupling relations exist between the chemical species and the temperature. Using detailed chemical schemes will add to the complexity of the problem. However, by the use of simple chemistry with simple estimation of the chemical source-term, such as expanding the temperature fluctuation term using Taylor series, will result into new terms that require to be modelled. Also, since there is no way to provide infinite closures for infinite unclosed terms, a truncation error will appear.

Another approach which is more reliable rather than expanding the temperature term is to use physical assumptions in order to get an estimate for the mean chemical source-term. Some of the well-known approaches are described in Section (2.3.1-2.3.6). Bilger et al. [21] categorized turbulent combustion modelling based on either a 1) separation of scales and/or 2) separation of model elements that address the model description of moments of reactive scalars in terms of scalar description in state-space and model for the distribution (probability density function PDF / Filtered density function FDF) function [20]. For the first category, models based on the separation of scales, examples can be given such as the assumption of fast chemistry that assumes that chemistry is faster than any other physical processes in the flow (e.g. the eddy dissipation model (EDM) [22], the eddy break-up model (EBU) [23]) and the laminar flamelet model [24] which is applicable to flames where the thickness of flames is below the energetic turbulence scales of the flow. For the second strategy, the mean or filtered reaction rate is constructed using a weighted average of the instantaneous reaction rate and the distribution function. For the instantaneous reaction rate term, a 'reactor' model is needed that represents the flame conditions such as a flamelet library or CMC solutions. For the distribution description the mean mixture fraction and its variance may be used to construct the presumed shape PDF functions

for reactive scalars [20]. The advantage of the strategies in the second category such as transported Probability Density Function (PDF), Conditional Moment Closure (CMC), Multiple Mapping Conditioning (MMC) and CSE is that they are not dependent on the physical characteristics of the flame.

2.3.1 Infinitely fast chemistry assumption

In this category of turbulent combustion models, the time scale for chemical reactions is considered to be very much faster in comparison to the mixing time scale. This is an appropriate assumption especially for the case of non premixed (diffusion) flames where chemical reaction time scale is found to be much less than the time scale of the other physical processes, such as convection and diffusion [18]. Two famous models developed based on the infinitely fast chemistry are the eddy dissipation model (EDM) [22], and the eddy break-up model (EBU) [23]. The former is introduced for non-premixed combustion, and the latter is designed for premixed combustion. In the EBU model, the mean reaction rate is a function of the rate of mixing between the reactants and hot products. The mean reaction rate of any product species k is calculated as

$$\overline{\dot{\omega}_k} = C_B \rho \frac{\varepsilon}{k} \widetilde{Y_k''^2}^{\frac{1}{2}}, \tag{2.25}$$

where C_B is a model constant (needs to be set for each case), and $\widetilde{Y_k''^2}$ the variance of the product species k mass fraction. Although the EBU model is simple and fast in terms of computational time required, it usually over-predicts the reactive scalars, and also has the disadvantage that detailed chemistry cannot be included in the model. The EDC model provides a closure for the averaged source term as

$$\overline{\dot{\omega}}_{fu} = C_D \overline{\rho} \frac{\varepsilon}{k} min\left(\widetilde{Y}_{fu}, \frac{\widetilde{Y}_{ox}}{S}, \beta \frac{\widetilde{Y}_{fu}}{1+S}\right), \tag{2.26}$$

where C_D and β are model parameters that need adjustment for any specific case, S the oxidizer-fuel stoichiometric mass ratio, $\widetilde{Y}_{fu}$ and $\widetilde{Y}_{ox}$ the Favre-averaged mass fraction of fuel and oxidizer, respectively. The model is just as simple as that of the EBU model but has the benefit that it can be used with finite rate kinetics by modifying the mixing time scales with chemical time scale data. By using this modification, the EDC model can be coupled with detailed chemistry [25]. Overall, because the model constants need to be investigated and adjusted for each individual case, the EDC model can not be considered as a robust combustion model for different industrial applications.

However, since the model constants need to be studied and adjusted for each individual case, is a drawback and does not make it a robust combustion model for industrial applications.

2.3.2 Laminar flamelet model

This model has been proposed by Peters [24] and Kuznetsov [26], independently. This model is based on the assumption that the turbulent diffusion flame is formed of an ensemble of stretched laminar flamelets, i.e. extremely small, thin flame elements [27]. Because mixing of the fuel and oxidizer determines the flame's behavior in diffusion flames, a conserved scalar Z is introduced to track the mixing process of the reactants and is called mixture fraction. This scalar takes a value between zero and one (0 for pure oxidizer case and 1 for pure fuel). The mixture fraction can be characterized by Bilger's definition

$$Z = \frac{Y_i - Y_{i,O}}{Y_{i,F} - Y_{i,O}}, \tag{2.27}$$

where Y_i the mass fraction of element i in the local mixture, and $Y_{i,O}$ and $Y_{i,F}$ are the mass fraction of the element i in the oxidizer and the fuel streams, respectively. Also, the mixture fraction can be obtained by solving a transport equation for its mean value. Mixture fraction is usually used to describe the variation of other scalars involved in the reactive flow, with the assumption of fast chemistry, zero heat loss and equal diffusivity. The Favre-averaged transport equation of mixture fraction can be expressed as

$$\frac{\partial(\overline{\rho}\widetilde{Z})}{\partial t} + \frac{\partial}{\partial x_i}(\overline{\rho}\widetilde{u_i}\widetilde{Z}) = \frac{\partial}{\partial x_i}\left(\overline{\rho D \frac{\partial Z}{\partial x_i}} - \widetilde{\rho u_i'' Z''}\right), \tag{2.28}$$

where turbulent flux is closed using the gradient assumption as

$$\widetilde{u_i'' Z''} = -D_t \frac{\partial \widetilde{Z}}{\partial x_i}, \tag{2.29}$$

where D_t is the turbulent diffusivity. Also, the transport equation for the variance of mixture fraction $\widetilde{Z''^2}$ is given by

$$\begin{aligned}\frac{\partial(\overline{\rho}\widetilde{Z''^2})}{\partial t} + \frac{\partial}{\partial x_i}(\overline{\rho}\widetilde{u_i}\widetilde{Z''^2}) = \frac{\partial}{\partial x_i}\left(\overline{\rho D \frac{\partial Z''^2}{\partial x_i}} - \overline{\rho u_i'' Z''^2}\right) - 2\overline{Z''\frac{\partial}{\partial x_i}\left(\rho D \frac{\partial Z}{\partial x_i}\right)} \\ -2\overline{\rho u_i'' Z''}\frac{\partial \widetilde{Z}}{\partial x_i} - 2\overline{\rho D \frac{\partial Z''}{\partial x_i}\frac{\partial Z''}{\partial x_i}}.\end{aligned} \tag{2.30}$$

The turbulent transport ($-\frac{\partial}{\partial x_i}\overline{\rho u_i{}'' Z''^2}$) and the production term ($-2\overline{\rho u_i{}'' Z''}\frac{\partial \widetilde{Z}}{\partial x_i}$) are modelled using the gradient assumption similar to Eq. 2.29. The molecular diffusion $\left(\frac{\partial}{\partial x_i}\left(\overline{\rho D\frac{\partial Z''^2}{\partial x_i}}\right) - 2\overline{Z''\frac{\partial}{\partial x_i}\left(\rho D\frac{\partial Z}{\partial x_i}\right)}\right)$ is negligible compared to the turbulent transport for the case of high Reynolds flows. The scalar dissipation rate (SDR) term ($2\overline{\rho D\frac{\partial Z''}{\partial x_i}\frac{\partial Z''}{\partial x_i}}$) dissipates the fluctuations of the mixture fraction analogous to the TKE dissipation rate. This analogy has led to the linear relaxation model of the mixture fraction SDR, $\widetilde{\chi}_Z$, expressed as

$$\widetilde{\chi}_Z = C_{\chi Z}\frac{\widetilde{\varepsilon}}{\widetilde{k}}\widetilde{Z''^2}, \tag{2.31}$$

where $C_{\chi Z}$ is a constant that is usually taken to be 2 [28]. The laminar flamelets are pre-tabulated and stored as a function of the mixture fraction before starting a CFD simulation. The Favre-averaged mass fraction of species k is calculated by integrating the presumed PDF multiplied by the ensemble of laminar flamelets at different strain rates (represents the flame structure), over the mixture fraction sample space, using the equation

$$\widetilde{Y}_k = \int_0^1 Y_k(Z)\widetilde{P}(Z;\vec{x},t)dZ, \tag{2.32}$$

where $Y_k(Z)$ is the tabulated mass fraction of species k as a function of Z.
The assumption of fast chemistry is not used for the case of finite-rate chemistry and an additional tabulation variable is needed to represent the flame away from the equilibrium conditions. The SDR of the mixture fraction is usually used for this reason, since it affects flame structure.
The flamelet model is valid for the flamelet regime, i.e. the flamelets are assumed to be smaller than the Kolmogorov scales. The flamelet model can also be used for premixed flames but in this case, a different key scalar rather than the mixture fraction must be selected. To describe the degree of combustion completion, a progress variable is selected or G-equation approach is used [18]. To make the progress variable similar to the mixture fraction, usually a normalized progress variable c is selected so that its value can vary from 0 for no combustion to 1 for complete combustion. The progress variable transport equation is given as

$$\frac{\partial(\overline{\rho}\widetilde{c})}{\partial t} + \frac{\partial}{\partial x_i}(\overline{\rho}\widetilde{u}_i\widetilde{c}) = \frac{\partial}{\partial x_i}\left(\overline{\rho D\frac{\partial c}{\partial x_i}} - \widetilde{\rho u_i{}'' c''}\right) + \overline{\dot{\omega}}_c. \tag{2.33}$$

The progress variable is not a conserved scalar, like the mixture fraction, and therefore has a source-term that needs closure. The source term can be modelled with different closures that include Bray-Moss-Libby (BML) model [29] and the flame surface density (FSD) model [18]. As a result, the flamelet model has a better capability to include detailed chemistry description than the EDC or EBU models and at the same time have a reasonable computational cost. The disadvantage of this model is however, the fact that it is only valid for the flamelet regime where turbulent eddies are not expected to affect the flame structure.

2.3.3 Conditional Moment Closure (CMC)

CMC model is based on the fact that once the scalars are conditioned on a specific scalar, such as mixture fraction, their fluctuations about the mean are significantly reduced. This model was first proposed by by Bilger [30] and Klimenko [31], independently. The advantage of CMC is that unlike the flamelet model, it is not limited to a specific turbulent combustion regime and can be coupled with finite-rate kinetic mechanisms. As mentioned, in non-premixed combustion, the scalars of interest are often conditioned on mixture fraction, while in premixed combustion, a progress variable is selected as a conditioning variable.

The mean conditional value of any scalar f is obtained by the following integral

$$\widetilde{f} = \int_0^1 \overline{f|\eta}\widetilde{P}(\eta)d\eta, \tag{2.34}$$

where $\overline{f|\eta}$ is the conditional average of f that is conditioned on a given value of mixture fraction, η. To obtain the the conditional scalars, a transport equation of the scalar has to be solved over the CMC grid which is usually similar to the CFD grid but much coarser. The mixture fraction should also be discretized into different bins for which the scalars are conditioned. The transport equations of conditional scalars will contain some unclosed terms that need to be closed such as the conditional chemical reaction rate, conditional velocity, and conditional turbulent flux. First order closure, which means that the fluctuations about the conditional averages are negligible, is common in CMC simulations. In this case, the chemical source term can be estimated as

$$\overline{\dot{\omega}_k|\eta} \approx \dot{\omega}(\overline{T|\eta}, \overline{\rho|\eta}, \overline{Y_k|\eta}). \tag{2.35}$$

In the cases such as in autoignition or extinction cases, where the fluctuations cannot be neglected, second order closure should be used, which means, closure should be provided for the fluctuations as well [32]. CMC provides very good predictions at different combustion regimes and transient phenomena [33, 20, 34].

2.3.4 PDF transport equation model

In The PDF transport equation method, a transport equation for the joint PDF of velocity, viscous dissipation and reaction scalars is solved. In contrast to the flamelet or CMC models that consider a presumed PDF or joined PDF, a transport equation is solved for the joint PDF of velocity, viscous dissipation and reactive scalars [35].
PDF methods can be used for both premixed and non-premixed flames. Since the PDF methods do not contain any information on the mixing time, an unclosed term arises which requires modelling. modelling this unclosed mixing term can be done using scalar gradients but increases the dimensionality of the model and as a result increases the computational cost. Pope [36] developed the Monte-Carlo Lagrangian method to reduce the computational cost. In this method, a large number of stochastic particles are used as the flow representation in the domain, and their evolution in the flow field helps determine the evolution of the joint PDF. Another approach is developed, independently, by Valino [37] and Sabelnikov and Soulard [38] which uses stochastic fields instead of particles.
Overall, the PDF methods provide the best description of turbulent reacting flows [25] because they provide a closed form for the chemical reaction source term and no closure model is required. Another advantage of the PDF methods is that they are not limited to a specific combustion regime. However, they are computationally expensive compared to the other models and the modelling of the mixing term is complex.

2.3.5 Multiple Mapping Conditioning

The Multiple Mapping Conditioning (MMC) method is proposed by Klimenko and Pope [39] which is derived as a combination of the CMC model and the PDF transport approach, taking advantage of these two models. In this hybrid method, the joint PDF of the conditioning scalars is obtained implicitly by being consistent with the conditional dissipation rates of the species. Then the concentration of the species and the dissipation rates are found using this joint PDF. A combination of two reliable models makes the MMC method one of the most promising methods, despite the high computational cost. MMC has been successfully used in the simulation of non-premixed [40, 41], premixed [42] and partially premixed flames [43].

2.3.6 Conditional Source-term Estimation (CSE)

This model was initially proposed by Bushe and Steiner [44]. It is based on the same concepts used in the CMC approach, but in contrast, the conditional averages are not obtained by solving transport equations for the conditional quantities. The conditional averages are instead obtained by integral inversion. Further details about this method and its formulation are given in Chapter 3. CSE has been successfully used in premixed flames [45], non-premixed flames [46] and partially premixed flames [47]. Different chemistry mechanisms have been used with CSE, starting from simple chemistry [48] to flamelet tabulation [49], and detailed tabulated chemistry [50]. Overall, CSE provides the advantage of not being limited to any specific turbulent combustion regime and having a reasonable computational cost, which makes it a promising approach for further study.

2.4 Soot Formation

Combustion systems may produce particulate emissions, known as soot. Soot is a mass of carbonaceous particles, resulting from incomplete combustion of hydrocarbon fuels under fuel-rich conditions. Soot formation is a very complex process consisting of different stages of the transformation of gas-phase unburned hydrocarbon fuel molecules to solid phase carbonaceous particles containing a few millions of carbon atoms [8]. The initial studies on the structure of soot was performed by Williams and coworkers [51, 52, 53]. They used thermophoretic and molecular beam sampling on premixed flames of acetylene (C_2H_2), benzene (C_6H_6), and propane (C_3H_8) and further analysis with transmission electron microscopy (TEM). They showed that soot was consisted of small spherical primary particles with almost constant diameters, formed in aggregated structures that had wide distributions for the number of primary primary particles in each aggregate. In Fig. 2.1 two TEM pictures of soot are shown. Fig. 2.1(a), shows soot in a premixed methane-oxygen (CH_4/O_2) flame along the flame axis at at a distance 22.5 mm above the burner. As shown in Fig. 2.1(a) the soot aggregate structure and that the soot particles have approximately the same diameters. In Fig. 2.1(b) which shows a laminar co-flow ethylene-air (C_2H_4/air) diffusion flame, the higher tendency of soot formation and the structure of soot can be seen.

For soot that is generated in flames, the number of primary particles per aggregate varies from a few up to several thousands [55]. Also, the diameter of the primary particles is generally less than 60 nm, with largest diameters associated with heavily sooting flames [56].

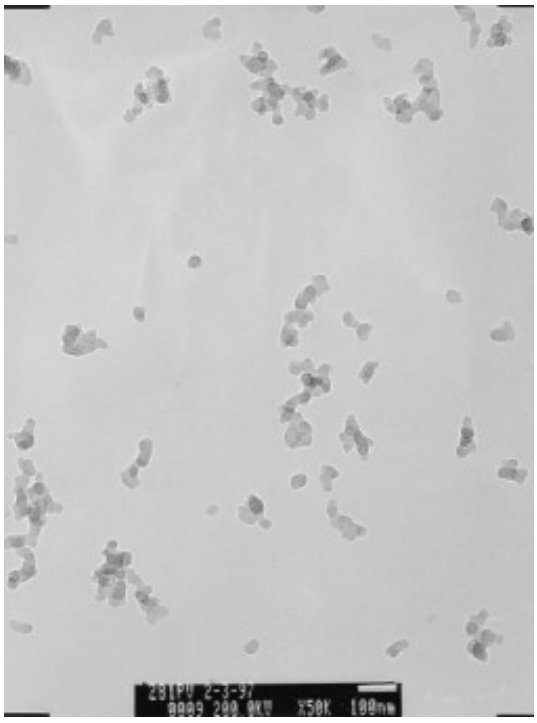

(a) Soot in a premixed flame, taken from [54]

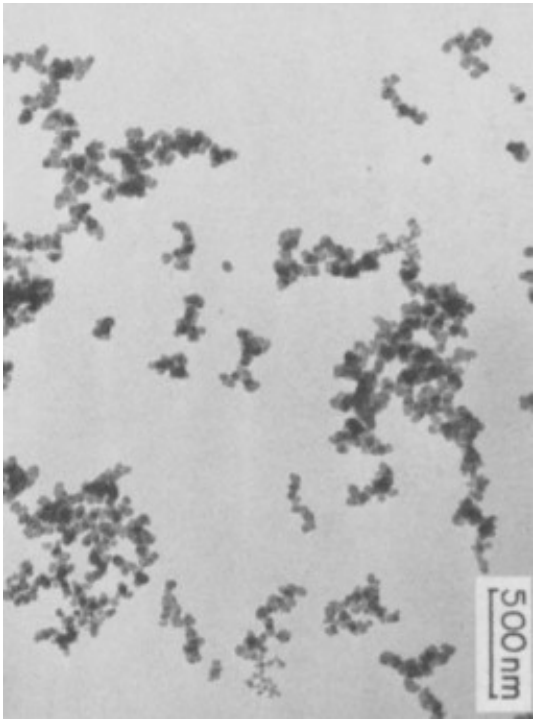

(b) Soot in a diffusion flame, taken from [55]

Figure 2.1: TEM pictures of soot in flames

Soot formation has been studied for many years and detailed review studies on soot formation have been presented by Glassman [57], Kennedy [58], Palmer and Cullis [59], Haynes and Wagner [60], and Frenklach [61]. Soot formation occurs incorporating different complex and simultaneous chemical and physical processes. The general soot formation processes in diffusion flames can be summarized into the following steps, and illustrated in Fig. 2.2 [62]:

1. Formation of soot precursor molecules
2. Nucleation of precursor molecules to form particles
3. Surface growth and coagulation of soot particles
4. Soot particle oxidation

Also, different stages of the formation of soot particles are shown in Fig. 2.3.

Fuel pyrolysis and Formation of soot precursor molecules

The first step in soot formation is the pyrolysis of the fuel, mostly at fuel-rich mixtures, leading to the formation of soot precursors. Different point of views for the precursors of soot exist in the soot scientific community, but among those, acetylene (C_2H_2) and benzene (C_6H_6) have received the most approval. The process of the break down and the pyrolysis of the fuel which leads to the formation of soot precursors is a chemical phenomenon and is described by a gas-phase chemical kinetic mechanism which provides species that are required for subsequent soot formation processes. Later, the precursors interact with each other, grow, and eventually lead to soot nucleation to form nascent soot particles. Nucleation is undoubtedly one of the least understood soot formation processes [65]. There have been different theories for the soot particle nucleation step, which includes polyacetylenes [66], ionic species [67], or PAHs [60] as the soot nucleation species. The most widely accepted theory up to this date, supported by numerous experimental and modelling studies, is that soot particles form via PAHs [61]. For PAH-based soot formation pathways, the formation and growth of aromatic species seems to be of great importance. Different studies have been concentrating on the formation of the first aromatic ring (benzene or phenyl) from small aliphatics, because this step is known to be the rate-limiting step in the reaction sequence to larger aromatics. On the formation pathway of the first aromatic ring, debate still exists among researchers. Frenklach [61] suggested the even-carbon-atom pathways that involve reactions of $n-C_4H_i$ (i= 3,5) species with C_2H_2. In contrast, Miller and

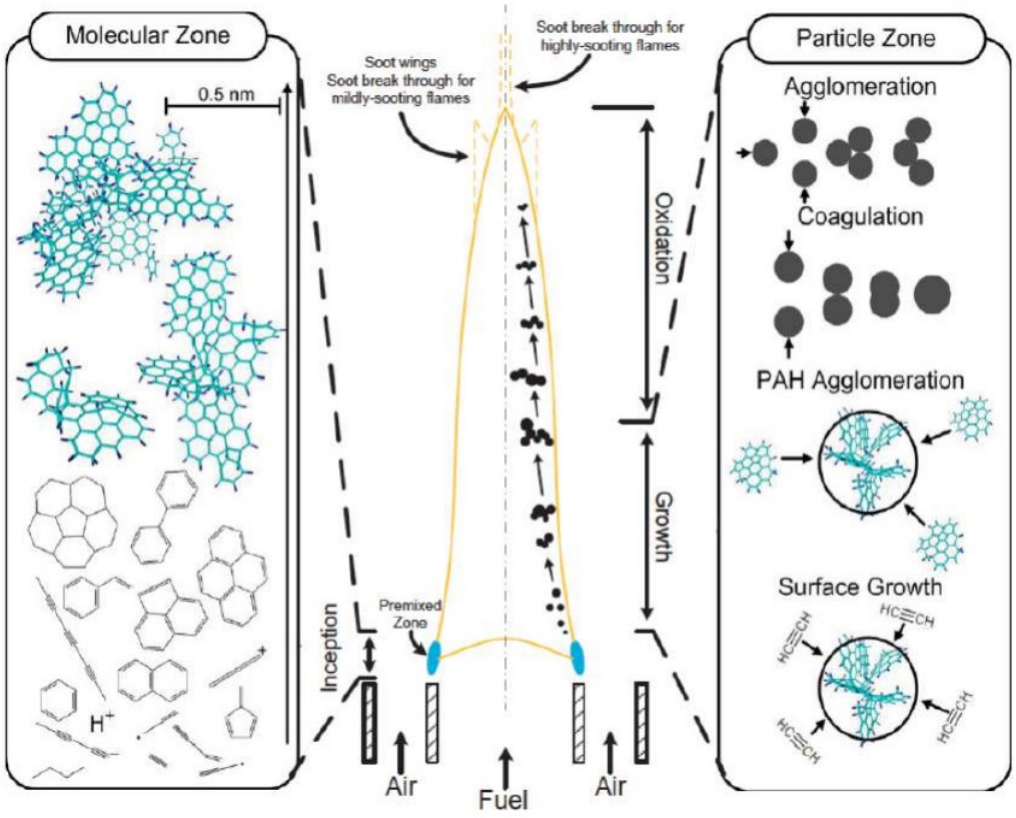

Figure 2.2: Schematic of soot formation process in a co-flow diffusion flame, taken from [63]

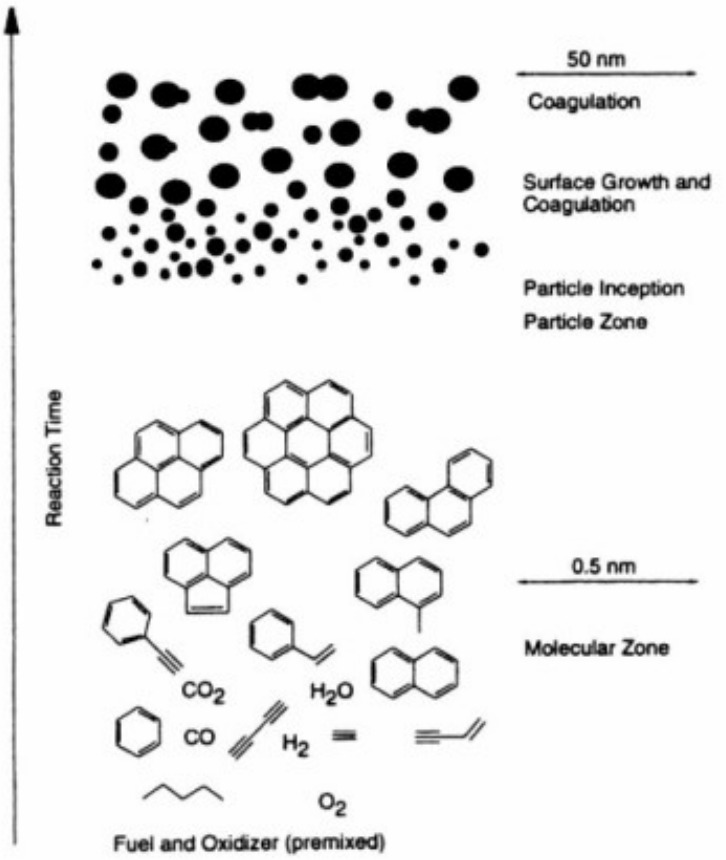

Figure 2.3: Different steps of soot formation in flames, taken from [64]

Melius [68] suggested that $n-C_4H_3$ and $n-C_4H_5$ could not be present in sufficiently high concentrations because they transform rapidly to their corresponding resonantly stabilized isomers, iso-C_4H_3 and iso-C_4H_5. Therefore, they proposed an odd-carbon-atom pathway via combination of propargyl radicals (C_3H_3); This is also proposed by other researchers [69, 70]. Other odd-carbon-atom pathways have also been suggested, including the reaction of C_5H_5 with CH_3 to form benzene [71] and the reaction of C_3H_3 with C_2H_2 to form a cyclopentadienyl radical which reacts rapidly to form benzene [71]. Furthermore, the self-combination of C_3H_3 has been found to be a very important pathway leading to the formation of benzene [72]. The above-mentioned different pathways to the first single-ring aromatic species, are summarized as [61]:

- Even-carbon-atom pathway via addition of acetylene to $n-C_4H_3$ and $n-C_4H_5$:

$$\text{n}-C_4H_5 + C_2H_2 \longrightarrow \text{phenyl} \tag{2.36}$$
$$\text{n}-C_4H_5 + C_2H_2 \longrightarrow \text{benzene} + H \tag{2.37}$$

- Odd-carbon-atom pathway via combination of propargyl radicals:

$$C_3H_3 + C_2H_2 \longrightarrow \text{benzene/phenyl} + H \tag{2.38}$$

- Reaction between propargyl and acetylene to form a cyclopentadienyl radical:

$$C_3H_3 + C_2H_2 \longrightarrow C - C_5H_5 \tag{2.39}$$

  which then forms an alternative odd-carbon pathway:

$$C_5H_5 + CH_3 \longrightarrow \text{benzene} + H + H \tag{2.40}$$
$$C_5H_5 + C_5H_5 \longrightarrow \text{naphthalene} + H + H \tag{2.41}$$

During the pyrolysis of aromatic fuels, large concentrations of acetylene and other active reactants are formed that contribute to the formation of the first benzene ring. However, for aliphatic fuels such as methane, ethylene or acetylene, lower concentrations of reactants required for aromatic formation are available, hence they are formed from decomposition products by a sequence of elementary reactions [63]. This can be the reason for why aromatic fuels tend to have higher sooting tendencies than aliphatic fuels.
Once the first aromatic ring is formed, it can grow to larger multi-ringed aromatic species (PAHs) via the H-abstraction-C_2H_2-addition (HACA) reaction mechanism [73] along with ring-ring condensation [74]. It is widely accepted that the dominant process responsible for the growth from aromatic species to larger PAHs is the HACA mechanism [61, 75]. HACA mechanism is consisted of a reversible sequence of hydrogen atom abstraction from PAH molecules, followed by acetylene molecule addition to the radical reaction site formed [76]:

$$A_i + H \longrightarrow A_i^- + H_2 \tag{2.42}$$
$$A_i^- + C_2H_2 \longrightarrow \text{products} \tag{2.43}$$

Here A_i denotes an aromatic molecule with i peri-condensed rings, and A_i^- is its radical. The reverse of HACA mechanism is also important in soot formation process[76]:

$$A_i^- + H_2 \longrightarrow A_i + H \tag{2.44}$$
$$A_i^- + H \longrightarrow A_i \tag{2.45}$$
$$A_i^- + C_2H_2 \longrightarrow \text{products} + H \tag{2.46}$$

Nucleation of precursor molecules to form particles

In the second step, PAH molecules undergo transition from gas phase to solid phase to form nascent soot particles with approximately molecular mass of 2000 amu and diameter of 1.5 nm [63]. by further growth of PAH species, large PAH structures are formed. Once PAH species become larger, at some size, PAH species begin to stick to each other after collision, forming PAH dimers (dimerization). PAH dimers can collide with each other or can grow via chemical growth reactions. Therefore, The PAH clusters continue to grow until eventually they evolve into solid soot particles.

Surface growth and coagulation of soot particles

In the third step, the generated soot particles undergo surface reactions which causes further growth of the nucleated particles. They experience surface chemical reactions with gaseous molecules as well as colliding with other soot particles that cause them to stick together and form larger chain-like aggregates. It is believed that surface growth of soot particles is similar to that of HACA mechanism in the molecular level [61], increasing the amount of soot mass. Particle growth by surface reaction increases the amount of soot, but the number of particles remain constant. Another mechanism that soot particles undergo and interact with each other is called coagulation. Once soot particles are formed, they can collide with each other due to their Brownian motion, forming larger particles. This physical process is termed coagulation. Coagulation does not change the total mass of soot particles, but it changes soot morphology, soot number density, and soot particle size distribution.

Soot particle oxidation

As soot particles are formed and advected up to the tip of the flame, they experience oxidation. The process converts the solid soot particles back into gases due to oxidizing

species such as O, O_2, and OH [62]. If soot oxidation occurs completely, there will be no soot emitted from the flame, but mostly this does not happen. Among various species, O_2 and OH are known to be the most important soot oxidizing species because of their abundance and reactivity. O_2 has the highest contribution in fuel-lean regions, while OH has the highest contribution in fuel-rich regions [65].

2.5 Soot Modelling

A wide range of soot models are available that can include soot formation and oxidation with different levels of accuracy and complexity [58]. There are empirical models which are the simplest ones and use correlations of experimental data to predict soot levels. they are usually based on the operating conditions of a flame and once the operating conditions of a flame change, produce very poor results. Another category is the detailed soot models which are more complex and require higher computational efforts. These models usually contain additional major components: detailed chemistry of soot, and soot aerosol dynamics that takes soot particle interactions and particle size distribution into account. Detailed soot models employ detailed chemistry steps to predict Poly Cyclic Aromatic hydrocarbons (PAH) formation. Frenklach and Wang [77, 78] presented detailed models that start from fuel pyrolysis, followed by tracking PAH formation, growth and agglomeration of particles. They have presented the H abstraction/C_2H_2 addition (HACA) mechanism for soot surface growth as well as soot oxidation via O_2 and OH pathways. Furthermore, soot aerosol dynamics are solved to keep track of particle agglomeration into aggregate structures. The particle size distribution function is generally treated in one of the three common methods: 1) Monte Carlo stochastic processes [79], 2) Sectional methods [80, 81], 3) Method of moments [82, 83, 84, 85, 86]. A detailed discussion about these three techniques can be found in [85]. These detailed models are very complex and computationally expensive. In contrast, another category of soot models exist which are called the semi-empirical models and have less complexity. Semi-empirical models are widely used and have shown to be a reasonable choice for complex turbulent combustion simulations [33, 87, 88]. The semi-empirical soot models provide global reaction steps based on the qualitative understanding of the soot formation mechanism, making them easy for implementation into turbulent combustion models.

Soot formation modeling in turbulent flames has been done for different flames using semi-empirical models. Brookes and Moss studied soot formation in methane-air combustion at atmospheric and elevated pressures [87]. They presented quantities such as mixture fraction, temperature, and soot volume fraction. They also published another paper pre-

senting their numerical results for their flames using an extended flamelet approach and a semi-empirical soot model [87]. Their predictions are in good agreement with experimental results for 1 atm flame with approximately 13% under prediction for the peak soot volume fraction. But for the 3 atm flame, the predicted soot volume fractions are three times higher when using a first-order dependence of the soot growth term on acetylene concentrations. Therefore, modifications to the model, calibrated for the 1 atm pressure, were done and the best agreement between measurements and predictions was achieved by using a factor of 0.4 for the power dependence of soot surface growth term on acetylene concentrations. Kronenburg et al. [33] studied soot modeling in the same flames by using the CMC approach. They used the semi-empirical model of Lindstedt [89] and considered differential diffusion in their simulations. Good predictions were achieved at atmospheric and elevated pressure when they included the effect of differential diffusion. For the 1 atm pressure flame, the peak soot volume fraction was under predicted by about 17% when differential diffusion was considered, while the equal diffusivity calculations gave soot volume fractions about 60% below the measured values. Also, for the 3 atm flame, unity Lewis number assumption under predicted soot volume fractions by approximately 40%, However, the differential diffusion assumption resulted in excellent predictions at mid-flame locations and slightly under predictions at far downstream locations. Wen et al. [88] studied soot formation in turbulent kerosene/air diffusion flames. They compared two different inception models for their flames; an acetylene based inception model, and a PAH based inception model (Hall et al.'s model [90]). They claimed that for simple aliphatic hydrocarbon fuels such as methane, the acetylene based models are reasonable but for more complex fuels such as kerosene which contain aromatics, the PAH models show significant improvements in predicting soot volume fractions. Their numerical results predicted the peak centerline soot volume fraction much closer to the fuel inlet than the experimental measurements resulting in an under prediction of soot volume fraction by a factor of three at the actual peak centerline soot location. Bolla et al. [91] also used the semi-empirical soot model of Leung et al. [92] to predict soot formation of n-heptane sprays under diesel engine conditions using Conditional Moment Closure (CMC) method. They used the RNG $k-\epsilon$ model for turbulence modeling and used an optical-thin formulation for radiation. They used the relatively simple soot model because the focus was not on the soot model, but rather on the predictive capability of the CMC approach. Their findings also suggest that the conditional moment closure method is a promising framework for soot modeling. It was found that despite the simpicity of the soot model employed, the model was able to to predict soot distributions semi-quantitatively with a discrepancy within a factor of 2 for most cases. It can be seen that soot models have been implemented with different combustion models such as CMC, flamelet, and Eddy Dissipation Concept (EDC) to simulate soot formation in turbulent flames. For validation of numerical modelling, different

sooting turbulent flames have also been experimentally investigated. Qamar et al. used Planar laser-induced incandescence (LII) technique to measure soot volume fraction in a piloted, turbulent non-premixed flame of natural gas known as the "Delft Flame III" [93]. Coppalle and Joyeux [94] investigated temperature and soot volume fraction distribution in an ethylene turbulent diffusion flame. There are also different flames, turbulent and laminar, that are presented as benchmarks and are very well characterised in the International Sooting Flame (ISF) workshop which provide very good data for model validation and comparison with numerical investigations [95].
In this research, the methane-air flames of Brookes and Moss [15] are selected because they are well documented, used by previous researchers, and very good chemistry reaction mechanisms exist for methane combustion. Also, methane is a lightly sooting flame, making it a good choice for a start point in the process of modeling soot formation. Also, the turbulent ethylene/air Sandia burner [17] is selected as another benchmark for further investigations. In the present research, soot modelling approaches will be built on and coupled with Conditional source-term estimation (CSE) model [96]. Since CSE has been shown to perform well in a wide range of premixed, non-premixed and partially premixed turbulent flames [97, 12, 98, 99], it makes it a good candidate for turbulent combustion modelling in more complicated cases such as soot modelling or spray flames. Up to now, no other research has been done in the field of soot modeling using the CSE approach and this is the first study that attempts to investigate soot formation in turbulent flames using the CSE turbulent combustion model.

2.6 Summary

This chapter provides the background information for soot modelling in turbulent flames. The governing equations are presented and the different approaches required for closing the unclosed terms are explained. Different turbulent combustion modelling strategies are explained and the benefits and disadvantages of each approach is mentioned. Then soot formation and its characteristics, as well as different processes in soot formation are discussed. Finally different strategies for soot modelling are presented and previous numerical studies in the field of turbulent flames are reviewed.

Chapter 3

Soot formation simulation using CSE and a semi-empirical soot model

The present chapter discusses the foundations of CSE, the formulation of CSE and how the chemistry tables are used to close the mean chemical source term in the species transport equations. A description for the beta PDF of the mixture fraction is provided. Also, a semi-empirical soot model, to model soot formation is described which is coupled with the CSE turbulent model. In addition, details on the TGLDM chemistry tabulation are provided. Finally, the quality of CSE in conjunction with a semi-empirical soot model is assessed.

3.1 CSE Formulation

The concept of CSE turbulent combustion model was proposed by Bushe and Steiner [100] and is based on the same fundamental concepts that CMC is built on [32]: the turbulent fluctuations found in the species mass fractions and temperature are correlated with the fluctuations of a conditioning parameter. In non-premixed combustion, mixture fraction (Z) is mostly selected as this key parameter. Therefore, if the scalars of interest, species mass fractions and temperature, are conditionally averaged on specific values of mixture fraction, the fluctuations about the resulting conditional averages would be negligible compared to the turbulent fluctuations about the unconditional averages; this is known as first order closure for the conditional chemical source terms. First order closure has shown to be valid for non-premixed flames without any significant ignition or extinction [32]. This

also implies that additional sample spaces and averaging are introduced. In other words, the conditional average of the scalars of interest are calculated at a particular value of η, in mixture fraction space. The major advantage of this approach is that the mean chemical source term needed in the species transport equation may be determined by directly using the conditional averages.

In CSE, the conditional chemical reaction rate for any species k, is calculated as function of conditional scalars (species mass fractions and temperature): $\langle \dot{\omega}_k|\eta \rangle \simeq \dot{\omega}\big(\langle Y_i|\eta \rangle, \langle T|\eta \rangle\big)$, here $\langle Y_i|\eta \rangle$ is the conditional mass fraction of species i, and $\langle T|\eta \rangle$ is the conditional temperature. The conditional mass fraction of species is achieved from integral inversion of the favre-averaged values of species mass fraction. Theoretically, all the species mass fractions can be obtained from integral inversion, but since the computational cost would be extremely high, the inversion process would be done for only a few species and the other scalars would be found based on these species from chemistry lookup tables. In CSE, the mass fractions of CO_2 and H_2O are selected as the species because of their long formation time, making them good candidates for inputs of the chemistry tables. Before starting the CFD simulations, chemical look-up tables are generated to save time and reduce the numerical effort. In the current study, Trajectory Generated Low Dimensional Manifold (TGLDM) method [101], which will be explained in more details in the next section, is used for tabulation. In the present study, the tabulation is carried out using the technique developed by Huang and Bushe [102] and Van Oigen and de Goey [103]. The chemistry tables are based on three variables: mixture fraction, $\langle Y_{CO_2}|\eta \rangle$ and $\langle Y_{H_2O}|\eta \rangle$. The TGLDM method uses chemical kinetic mechanism such as GRI-MECH version 3.0 including 53 species and 325 reactions and stores all the species mass fractions and chemical reaction rates as a function of only a few parameters which will be used during numerical simulations. Finally, the mean unconditional reaction rate for each species is calculated using

$$\overline{\dot{\omega}_k}(x_j, t) = \int_0^1 \frac{\langle \dot{\omega}_k|\eta \rangle}{\langle \rho|\eta \rangle}(\eta, x_j, t)\widetilde{P}(\eta, x_j, t)d\eta, \tag{3.1}$$

where x_j is the spatial coordinate, t the time and $\widetilde{P}(\eta)$ the Favre-averaged probability density function (pdf) of mixture fraction. In this study, the presumed beta-pdf distribution is used [104]. As mentioned earlier, the conditional averages of the mass fractions for CO_2 and H_2O are needed, which are obtained by inverting the following equation:

$$\widetilde{Y_k}(x_j, t) = \int_0^1 \langle Y_k|\eta \rangle(\eta, x_j, t)\widetilde{P}(\eta, x_j, t)d\eta, \tag{3.2}$$

where $\widetilde{Y_k}$ and $\widetilde{P}(\eta)$ are known quantities determined by solving a transport equation and the beta-pdf function respectively. Therefore, the only unknown in Eq. (3.2) is $\langle Y_k|\eta \rangle$ for

CO_2 and H_2O that is obtained by inverting Eq. (3.2).

3.2 Inversion process

The conditional averages are found to vary much less in space than unconditional averages [31]. For inverting Eq. 3.2, a group of cells in the domain should be selected to perform the inversion process on these cells, which are called CSE ensembles. The conditional averages are assumed to be homogeneous within a selected ensemble of points. Thus, the computational domain is divided into multiple ensembles where all the computational cells on each ensemble have the same conditional averages, while each computational cell has its own PDF based on the mixture fraction mean and mixture fraction variance. Therefore, Eq. 3.2 for a given ensemble, can be simplified as

$$\widetilde{Y_k}(x_j,t) = \int_0^1 \big\langle Y_k|\eta\big\rangle(\eta,t)\widetilde{P}(\eta,x_j,t)d\eta. \tag{3.3}$$

Eq. (3.3) is for one particular ensemble in which the conditional averages are not functions of space, whereas Eq. (3.2) is for any point in space. Selecting the shape and distribution of CSE ensembles depends on the flame being studied. For axisymmetric jet flames, the computational domain is usually divided by a set of planes in the axial direction to take advantage of the weak radial dependence of the conditional averages [105, 32]. Eq. (3.3) is a Fredholm integral of the first kind. Using a numerical quadrature, Eq. (3.3) can be given in the form of

$$A \cdot \vec{\alpha} = \vec{b}, \tag{3.4}$$

where A is the matrix of integrated PDF over a mixture fraction interval (bin) and is of size (N x M). N is the number of grid nodes in a given ensemble, and M is the number of bins in mixture fraction space. $\overrightarrow{\alpha}$ is the conditional average scalar vector of size M for a given ensemble, and $\overrightarrow{b}$ is the vector of size N, containing unconditional averages of $\big\langle Y_k|\eta\big\rangle$ at each mixture fraction bin (η_m). The matrix A can be calculated as

$$A_{jm} = \int_{\eta_1}^{\eta_2} \widetilde{P}(\eta_m,x_j,t)d\eta, \tag{3.5}$$

where j is the spatial coordinate index, η_1, and η_2 are the lower and upper bounds of the mixture fraction bin. The solution of Eq. (3.4) is ill-posed which means it is sensitive to

any small perturbation in the system [106]. Therefore, a regularisation method is required to obtain a stable, and unique solution. In a previous study [107], it has been shown that the zeroth order Tikhonov regularization method [108] provides a good approximation of the exact solution. Therefore, in this study this regularization method is used and it can be implemented in the CSE framework based on the least-square technique as

$$\vec{\alpha} = \arg\min\left\{ \left\| \mathbf{A}\vec{\alpha} - \vec{b} \right\|_2 + \lambda^2 \left\| \vec{\alpha} - \vec{\alpha}_0 \right\|_2 \right\}, \tag{3.6}$$

where λ is the regularization parameter, I is the identity matrix, $\vec{\alpha}_0$ *a priori* knowledge of the solution, and $\|..\|_2$ represents the L-2 norm operator. The *a priori* knowledge can be selected to be a one-dimensional unstrained laminar premixed flame solution [109, 110], or the solution from the previous time step [49]. Since the final solution is found to be independent of the *a priori* knowledge, the latter is selected in the current study for simplicity. In addition, an initial value of zero is set when the simulation begins. The regularization parameter λ is defined as

$$\lambda^2 = \frac{Tr(A^T A)}{Tr(I)}, \tag{3.7}$$

where Tr is the trace of the matrix. The LU-decomposition method is commonly used with Tikhonov regularization method in CSE simulations [111, 45, 46], and therefore selected in the current simulations.

3.3 Chemistry tabulation

In turbulent reacting flows chemical kinetic mechanisms are very important for accurately calculating the chemical source terms required in the species transport equation. For methane-air combustion, GRI-MECH 3.0 kinetic mechanism [112] is considered very common and well-known. It includes 53 species and 325 elementary reactions. Using detailed chemistry can provide very high accuracy in predicting the flames, but will cause a drastic increase in the computational time because it requires solving the chemical source term for each reactive cell at each time step. Moreover, in turbulent combustion problems different time scales exist for different reactions present in the flame. In order to accurately resolve all of these time scales, a very small time step is required to guarantee the numerical stability [113]. To overcome this issue, the chemistry is tabulated before the simulations to reduce

the dimensions of the mechanism while taking use of detailed mechanisms. In tabulated chemistries, the mechanism is represented as a function of lower number of parameters. In the current study the Trajectory Generated Low Dimensional Manifold (TGLDM), Initially proposed by Pope and Maas [114] and later modified by Huang and Bushe [102] is used for tabulation. The detailed kinetic mechanism is reduced to low-dimensional manifolds in composition space. A TGLDM manifold for each mixture fraction is generated and stored in tables using the mass fraction of CO_2 and H_2O due to their long formation times [102]. The manifold is consisted of reaction trajectories that are generated from the boundaries of the manifold. Each trajectory evolves, until it reaches the chemical equilibrium condition. The trajectories are constructed based on solving the following differential equation using numerical integration,

$$\frac{\partial}{\partial t} Y_k = \dot{\omega}_k, \tag{3.8}$$

A stiff Ordinary Differential Equation (ODE) system solver is used to solve Eq. (3.8) starting at each boundary point. The calculations continue until chemical equilibrium is reached. The initial conditions for Eq. 3.8 can be calculated by applying a mass balance of the elements and the concept of the "extreme-value-of-major-species", which is used by Pope and Maas [114]. Using this, the maximum values of each species mass fraction can be calculated using

$$Y_e(j) = \sum_{i=1}^{n_e+2} Y(i) f_{j/i}, j = 1...n_e, \tag{3.9}$$

where $f_{j/i}$ is the mass fraction of element j in species i and $Y_e(j)$ is the mass fraction of element j. Then, by using linear programming techniques [115], the realizable region of the manifold can be identified as well as the initial points of the trajectories.

For illustration, Fig. (3.1) shows the trajectories generated for a particular mixture fraction value. All of the trajectories with the corresponding species mass fractions and reaction rates form one manifold. As shown in Fig. (3.1), the trajectories start from different initial points and the evolution of each trajectory is stored towards the equilibrium point. After all the trajectories are identified, the redundant points are removed to reduce the size of the table. Also, Delaunay triangulation is used to locate the points in the manifold more easily [117] as seen in Fig. 3.2.

Finally, the generated chemistry tables include three dimensions η, Y_{CO_2} and Y_{H_2O}. The mixture fraction grid includes 100 bins for values of η ranging from 0.00286 to 0.99

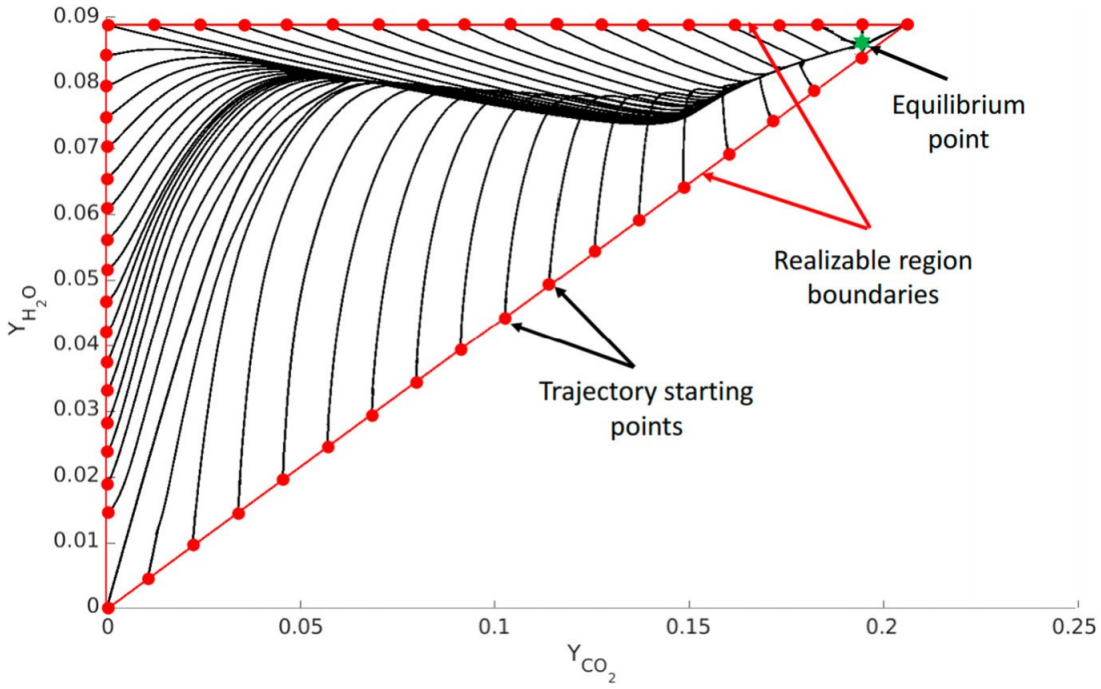

Figure 3.1: Solution points of Eq. 3.8 for each reaction trajectory shown on the manifold. Taken from [116]

.

with bins density being higher around the stoichiometric mixture fraction (η_{st}=0.055), as shown in Fig. 3.3.

In the TGLDM tables, the conditional reaction rates and the conditional mass fractions are stored. Also, the conditional chemical source term of the sensible enthalpy equation (Eq. 2.12) is tabulated. It is calculated based on the conditional reaction rates and the enthalpy of formation as

$$\langle \dot{q}_{react}|\eta\rangle = \sum_{1}^{k} \langle \dot{\omega}_k|\eta\rangle \triangle h^{\circ}_{f,k}, \tag{3.10}$$

where $\triangle h^{\circ}_{f,k}$ is the enthalpy of formation of species k at 298 K. Then, the mean chemical source term of the sensible enthalpy equation can be calculated as

$$\bar{\dot{q}}_{react} = \int_0^1 \frac{\langle \dot{q}_{react}|\eta\rangle}{\langle \rho|\eta\rangle} \widetilde{P}(\eta, x_j, t) d\eta, \tag{3.11}$$

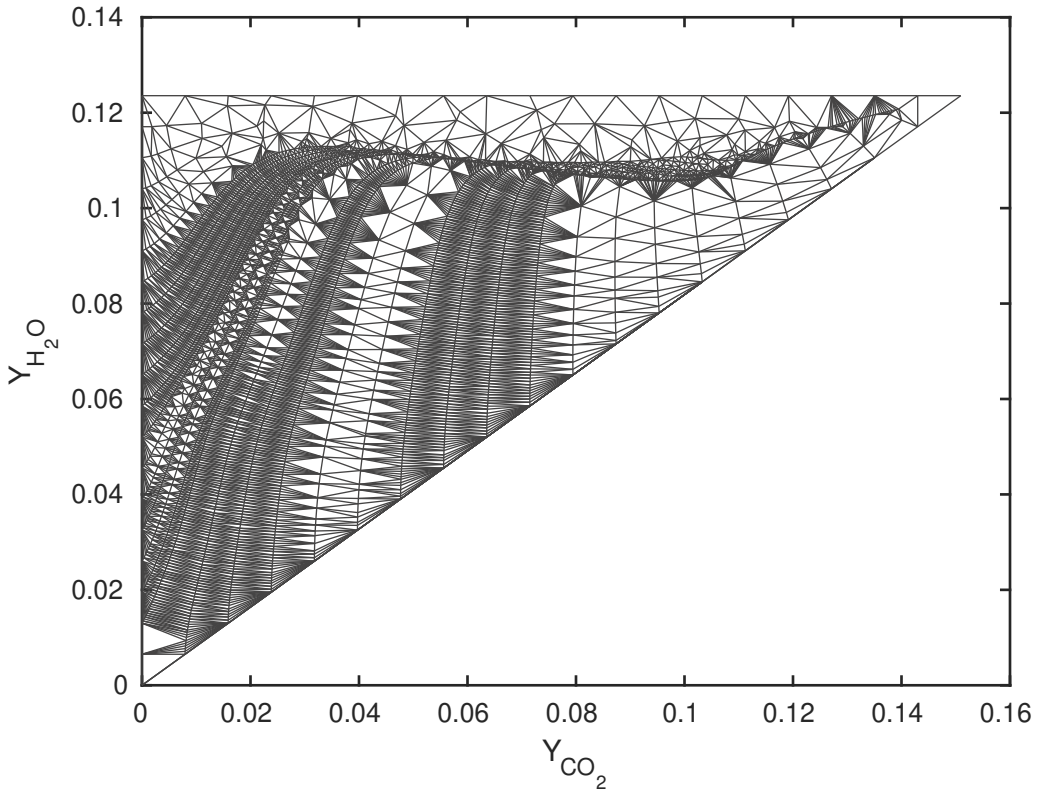

Figure 3.2: Delauney triangulation of the stoichiometric reaction manifold for the methane-air mixture ($\eta = 0.055$)

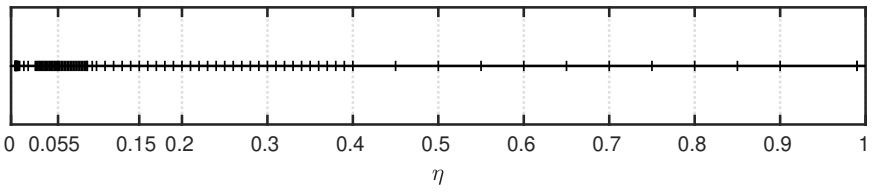

Figure 3.3: Graphical presentation of mixture fraction grid

3.4 Soot Model

In this chapter, a well-known semi-empirical soot model is implemented into the CSE framework. For this purpose, the two-equation semi-empirical soot model by Leung et al. [92] is selected. The soot model includes mechanisms for particle inception, agglomeration, surface growth and oxidation. The model has two transport equations for soot mass fraction (Y_s) and particle number density (N_s) [particles/kg-mixture], given as:

$$\frac{\partial \overline{\rho}\widetilde{Y_S}}{\partial t} + \frac{\partial}{\partial x_i}(\overline{\rho}\widetilde{u_i}\widetilde{Y_S}) = \frac{\partial}{\partial x_i}\Big(\frac{\mu_t}{Sc_{Yt}}\frac{\partial \widetilde{Y_S}}{\partial x_i}\Big) + \overline{\dot{\omega}_{Y_S}}, \tag{3.12}$$

$$\frac{\partial \overline{\rho}\widetilde{N_S}}{\partial t} + \frac{\partial}{\partial x_i}(\overline{\rho}\widetilde{u_i}\widetilde{N_S}) = \frac{\partial}{\partial x_i}\Big(\frac{\mu_t}{Sc_{Nt}}\frac{\partial \widetilde{N_S}}{\partial x_i}\Big) + \overline{\dot{\omega}_{N_S}}, \tag{3.13}$$

where Sc_{Yt} and Sc_{Nt} are the turbulent Schmidt number for soot mass fraction and particle number density equations, respectively. In order to calculate the mean source terms required in Eqs. (3.12 and 3.13), first the conditional source terms are calculated based on the same analogy for calculating the conditional source terms for chemical reaction of species. In other words, the source terms are calculated in η space as a function of conditional averages of species concentrations and temperature, resulting in the conditional values of the reaction rates for soot mass fraction and number density. Once the conditional reaction rates are obtained, the non-conditional averaged values should be calculated and used in Eqs. (3.12) and (3.13). In the present soot model, the source terms are split into different parts corresponding to particle inception, surface growth, oxidation, and agglomeration and given as:

$$\langle \dot{\omega}_{Y_S}|\eta\rangle = \langle \dot{\omega}_{Y_S,inc}|\eta\rangle + \langle \dot{\omega}_{Y_S,gro}|\eta\rangle - \langle \dot{\omega}_{Y_S,oxid}|\eta\rangle, \tag{3.14}$$

$$\langle \dot{\omega}_{N_S}|\eta\rangle = \langle \dot{\omega}_{N_S,inc}|\eta\rangle - \langle \dot{\omega}_{N_S,agglo}|\eta\rangle. \tag{3.15}$$

The soot model is based on the assumption that the soot inception and growth are first-order functions of the acetylene (C_2H_2) concentration. The chemical reaction for soot nucleation and growth are:

$$\mathrm{C_2H_2} \longrightarrow 2\,\mathrm{C_{(s)}} + \mathrm{H_2} \tag{3.16}$$

$$\mathrm{C_2H_2} + \mathrm{nC_{(s)}} \longrightarrow (\mathrm{n}+2)\,\mathrm{C_{(s)}} + \mathrm{H_2} \tag{3.17}$$

with the reaction rates

$$R_n = k_n[C_2H_2] \tag{3.18}$$

and

$$R_g = k_g[C_2H_2] \tag{3.19}$$

$[C_2H_2]$ is the molar concentration in units of [kmol/m^3]. The source terms for different steps include a modified Arrhenius rate constant of the form $k_i = A.T^b e^{-T_\alpha/T}.{A_s}^c$. The values of the different Arrhenius parameters and other model constants are given in Table 3.1.
A_s is the surface area of soot in $[m^2/m^3]$ and is defined as

$$A_s = \pi d_p^2 \rho N_s \tag{3.20}$$

and the soot particle diameter, d_p, given as

$$d_p = \left(\frac{6}{\pi}\frac{\rho}{\rho_s}\frac{Y_s}{\rho N_s}\right)^{1/3} \tag{3.21}$$

The soot surface growth term is proportional to the square root of the soot surface area, because it is necessary to account for the reduced reactivity of soot particles due to the effect of aging throughout the flame [92]. The soot oxidation steps for O_2 and OH are

$$\mathrm{C_{(s)}} + \frac{1}{2}\mathrm{O_2} \longrightarrow \mathrm{CO} \tag{3.22}$$

$$\mathrm{C_{(s)}} + \mathrm{OH} \longrightarrow \mathrm{CO} + \mathrm{H} \tag{3.23}$$

with the reaction rates given by

$$R_{O_2} = k_{O_2}[O_2] \tag{3.24}$$

$$R_{OH} = k_{OH}[OH] \tag{3.25}$$

The oxidation step for O_2 is based on the mechanism by Lee et al. [118]. Reaction rate constants for OH are taken from Bradley et al. [118] and the efficiency of collision is set to 0.04 [119]. There is also another source term in the soot number density equation which takes into account of the decrease in soot particles due to particle agglomeration. This step is modeled as:

$$\mathrm{nC_{(s)}} \longrightarrow \mathrm{C_n(s)}, \tag{3.26}$$

with the reaction rate

$$R_{agglo} = 2C_a {d_p}^{1/2}\left(\frac{6\sigma_b T}{\rho_s}\right)^{1/2}(\rho N_s)^2, \tag{3.27}$$

Table 3.1: Soot model reaction rate constants [92]. (Units are in kg, kmol, m, s, K.)

Number	Condition	k_i	A	b	T_α	c	Reference
1	Nucleation	k_n	1.0×10^4	0	21000	0	[92]
2	Surface growth	k_g	6.0×10^3	0	12100	0.5	[92]
3	Oxidation by O_2	k_{O_2}	1.0×10^4	0.5	19800	1	[92]
4	Oxidation by OH	k_{OH}	0.36	0.5	0	1	[33]

where $\sigma_b = 1.38.10^{-23} J/K$ is the Boltzmann constant, $C_a = 9$ is the agglomeration constant, and ρ_s is the soot density and is considered 2000 kg/m^3. Using the expressions presented for nucleation, growth, oxidation, agglomeration and substituting them in Eqs. 3.14 and 3.15, the reaction rates for soot mass fraction and particle number density, in the conditional space, can be calculated as

$$\dot{\omega}_{Y_s} = 2k_n[C_2H_2]M_s + 2k_g[C_2H_2]M_s - k_{O_2}[O_2]M_s - k_{OH}[OH]M_s, \tag{3.28}$$

and

$$\dot{\omega}_{N_s} = 2k_n[C_2H_2]\frac{N_A}{C_{min}} - 2C_a {d_p}^{1/2}\Big(\frac{6\sigma_b T}{\rho_s}\Big)^{1/2}(\rho N_s)^2, \tag{3.29}$$

where $N_A = 6.022.10^{26}$ is the Avogadro number, and $C_{min} = 100$ is the minimum particle number required for nucleation. The soot volume fraction is also calculated as:

$$f_v = Y_s \times \frac{\rho}{\rho_s}. \tag{3.30}$$

After the conditional averages of the source terms are calculated, the unconditional averages of the source terms can be calculated using integral inversion as follows

$$\overline{\dot{\omega}_{Y_S}} = \int_0^1 \langle \dot{\omega}_{Y_S} | \eta \rangle \overline{P}(\eta) d\eta, \tag{3.31}$$

$$\overline{\dot{\omega}_{N_S}} = \int_0^1 \langle \dot{\omega}_{N_S} | \eta \rangle \overline{P}(\eta) d\eta. \tag{3.32}$$

The flow chart of the CSE-soot simulation steps are shown in Fig. 3.4.

3.5 Radiation model

The radiation effects are included in the simulations using an optically thin grey radiation model. In the optically thin (OT) approximation only the emission of radiation is considered, and it is assumed that the radiation passes through the medium without being

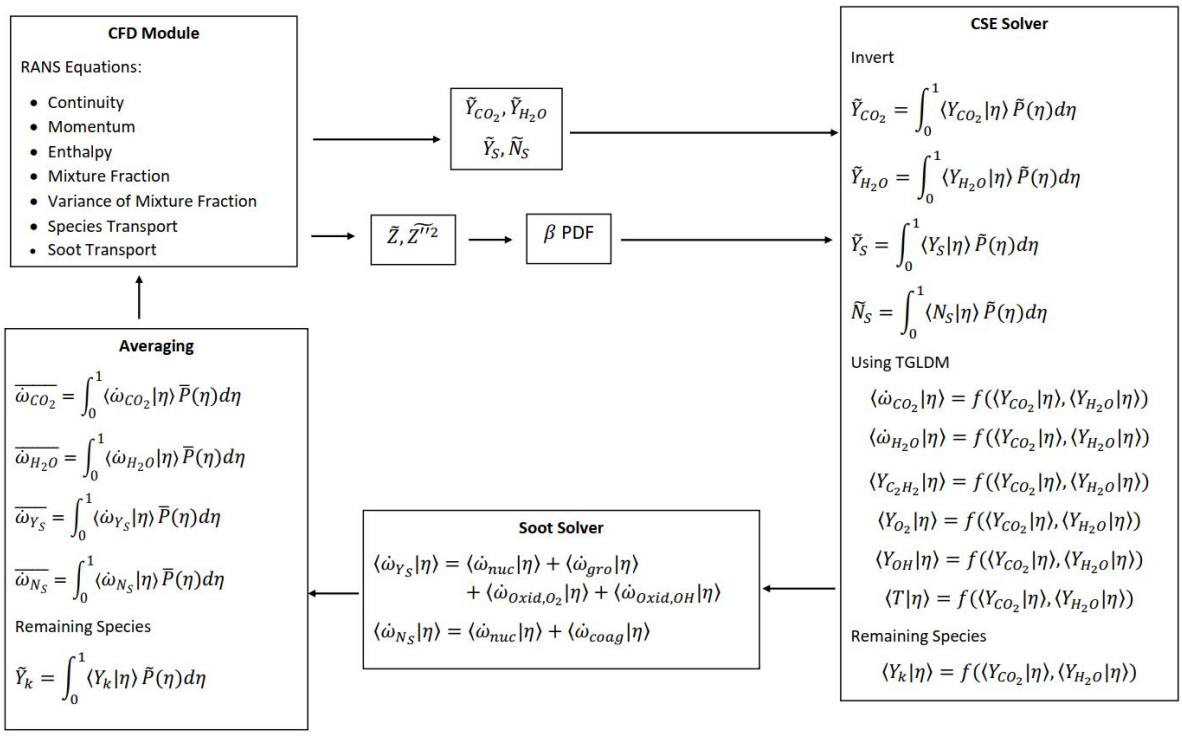

Figure 3.4: CSE-soot flow chart

absorbed, i.e., self-absorption is neglected. The vast majority of combustion studies dealing with turbulent flames have used this simplification. The advantage of optically thin assumption is that it does not require the solution to any radiative transfer equation (RTE), and it does predict the behavior of small-sized laboratory flames fairly well. However, in larger flames for industrial applications the OT model over predicts radiative heat loss. The radiative heat loss due to the main combustion product species H_2O, CO_2 , and CO is considered and curve fitting is to used determine the Planck absorption coefficients, as a function of the mass fractions of H_2O, CO_2 , and CO. The parameters for the curve fitting are found on the Sandia TNF website [120]. The radiative heat loss, $\overline{\dot{Q}_{rad}}$, is calculated as

$$\overline{\dot{Q}_{rad}} = 4\sigma\Big(\sum_{i=1}^{N} p_k K_{P,i} + K_{P,soot}\Big)\big(\tilde{T}^4 - T_\infty^4\big), \tag{3.33}$$

where σ is the Stefan-Boltzmann constant, p_i the partial pressure of species i in atmospheres, T the local flame temperature in K, T_∞ the background temperature, and $K_{P,i}$ is the Planck absorption coefficient of the ith species in the mixture. Further, the Planck mean absorption coefficient for soot can be calculated as [121]:

$$K_{P,soot} = 2370\frac{1}{mK}.f_v.T. \tag{3.34}$$

3.6 Computational details

In the study, the confined turbulent methane-air flames experimentally investigated by Brookes and Moss [15] are selected. The experimental setup consists of a cylindrical nozzle with a diameter of 4.07 mm for the main fuel and an annular pilot nozzle with a width of 160 μm surrounding the main nozzle. Around the main fuel nozzle, a co-flow of air exists with a mass flow rate of 708 g/min [15]. The flame is placed in a 155 mm Pyrex tube. For the 1 atm flame, the velocity of the fuel stream is 20.3 m/s (exit Reynolds number equal to 5000). For the 3 atm flame, the velocity of the fuel stream is 6.77 m/s in order to keep the Re number at 5000. The main fuel flow consists of pure methane, while the pilot flame is a premixed methane/oxygen flame with a flow rate of less than 2% of the main flow rate. The main fuel and co-flow air both have a temperature of 290 K. Experimental data is available for mean mixture fraction, temperature, soot volume fraction and spectral radiation intensity.
The CFD package, OpenFOAM version 7.0 [122] coupled with CSE, is used for conducting the numerical simulations. Eqs. (2.9 - 2.12) and (3.12 - 3.13) are solved using finite

volume pressure-based approach. In the CFD solver, seven reactive species are defined, methane (CH_4), carbon dioxide (CO_2), water (H_2O), carbon monoxide (CO), hydroxide (OH), hydrogen (H_2), oxygen (O_2) and two inert species, nitrogen (N_2) and argon (Ar). The governing equations of (CH_4), O_2, CO_2 and H_2O are solved and their chemical source terms are obtained using the conditional reactions from the TGLDM chemistry tables. In contrast, the mass fractions of C_2H_2, CO, OH and H_2 are obtained using the conditional mass fraction from the TGLDM tables

$$\underbrace{\langle Y_k|\eta\rangle}_{\text{from TGLDM}} = f(\langle Y_{CO_2}|\eta\rangle, \langle Y_{H_2O}|\eta\rangle), \tag{3.35}$$

and the integration following Eq. 3.2. It should be noted that an inversion could be performed for all species mass fractions. Inversion of all species is not considered due to considerable computational time that would be needed and the present inversion technique (zeroth order Tikhonov method) does not enforce conservation of mass in the inversion process. Hence, the inversion is only performed for two species carbon dioxide (CO_2) and water (H_2O).

In the simulations, time derivatives are discretised using an implicit second-order backward scheme. Gauss limited linear scheme is used for the divergence terms and a Gauss linear scheme is used for gradients. Also, Gauss Linear limited scheme, which is a second-order scheme is chosen for diffusion term.

The k-ε turbulence model [123] is selected with $C_{\varepsilon 1}$=1.47. To correct the standard k-ε over prediction of spreading rate in round jets, different $C_{\varepsilon 1}$ values have been tested for the flame under investigation and the predictions for mixture fraction and temperature using $C_{\varepsilon 1}$=1.47 showed best agreement with experimental results. The computational domain is cylindrical with a radius of 77.5 mm and a length of 1000 mm. A small angle wedge (4^o) is defined with only one cell in the θ direction, creating a 2D domain and reducing the computational cost. The grid is non uniform with a finer grid close to the nozzle and in the radial direction where the flame develops. The current mesh consists of 58,800 cells. Mesh refinement was applied to the current grid and the present results are found to be mesh independent. Fuel inlet velocities are set to the experimental values. For the 1 atm flame, the air co-flow velocity is equal to 0.514 m/s and for the 3 atm case, 0.171 m/s. No-slip boundary condition is set for the walls. Also, a sensitivity analysis is performed on the number of ensembles to make sure that the results are independent of the number of ensembles. For this purpose, four sets of simulations are completed using 12, 24, 36, and 48 ensembles. It is found that 24 ensembles show ensemble-independent results and by increasing the number of ensembles no significant changes in the numerical predictions is observed. Therefore, in the current study the computational grid has been divided into

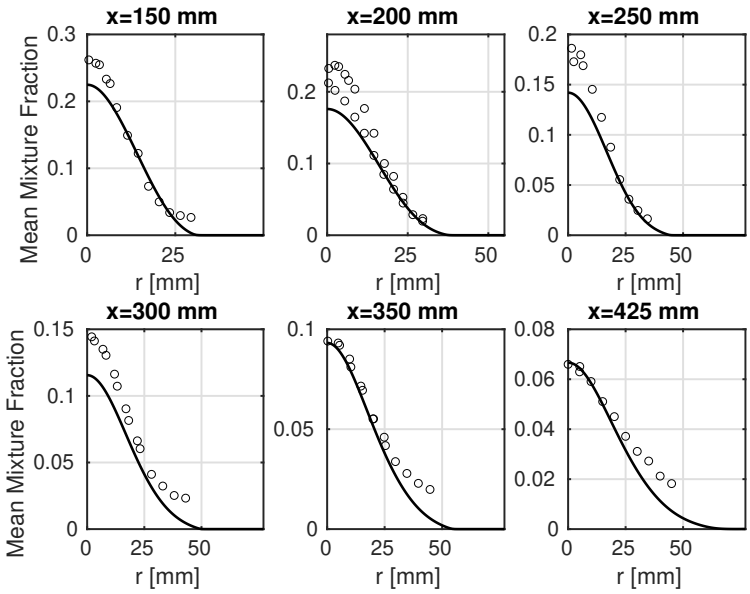

Figure 3.5: Radial mixture fraction at different axial locations - 1 atm. Symbols represent experimental data [15] and the line shows predictions obtained from numerical simulations.

24 CSE ensembles. In the current framework of CSE-soot model, there is no coupling between gas-phase and soot chemistry, i.e., it is assumed that soot nucleation and surface growth processes do not consume C_2H_2. Therefore, the effect of the reduced concentration of C_2H_2 on the gas-phase chemistry is not considered due to the limitations of the TGLDM tabulation method.

3.7 Results

3.7.1 Flame at atmospheric pressure

The radial mixture fraction profiles compared with experimental data [15] at different axial locations are shown in Fig. 3.5. The predicted profiles under predict the experimental results for the mean mixture fraction values close to the centerline below 300 mm, but farther downstream, the numerical simulations show good agreement with the experimental data. However, as we move away from the centerline and towards the edge of the flame the discrepancies decrease. The largest difference between the predictions and experimental

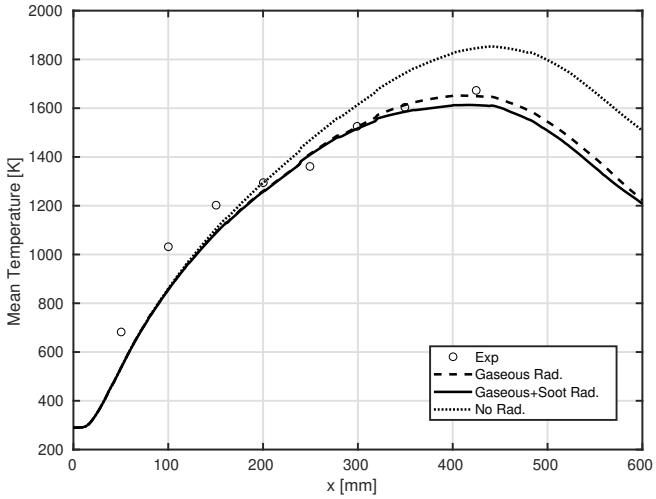

Figure 3.6: Centerline temperature - 1 atm.

values occurs at x = 300 mm with the predicted mixture fraction approximately 20% lower than the experimental values. This cannot be explained by the experimental error alone, reported to be 6% for mean mixture fraction measurements [15]. Possible reasons are likely due to uncertainties introduced by the $k - \varepsilon$ turbulence model and amplification of any temperature prediction discrepancies through the coupled soot-radiation effects acting on the mean density field and therefore, affecting the turbulent flow and mixing fields.

Figure 3.6 shows the centerline temperatures along the flame axis compared with experimental data. The temperature profiles with soot and gaseous radiation, with only gaseous radiation (without soot radiation), and without any radiation are presented. It can be seen that radiation decreases the maximum temperature approximately by 240K, and soot radiation portion contributes approximately to 40K (16% of the total temperature decrease due to radiation). As expected, radiation has a larger impact on the temperature profile for axial distances greater than 200 mm where higher temperatures are present with significant concentrations of product species. The predicted radial temperature profiles with the experimental data [15] are shown in Fig. 3.7. It can bee seen that overall, very good predictions are achieved except at x = 150 mm location, where the centerline temperature is slightly under predicted. The centerline predications are also predicted with good accuracy (all centerline values are found within 6% of experimental data), and the peak temperature locations are well resolved. At x = 425 mm, the centerline predicted temperature value has a good agreement with the experimental value, but moving towards the edge of the flame, the numerical temperatures are slightly lower and a thinner flame has been predicted by

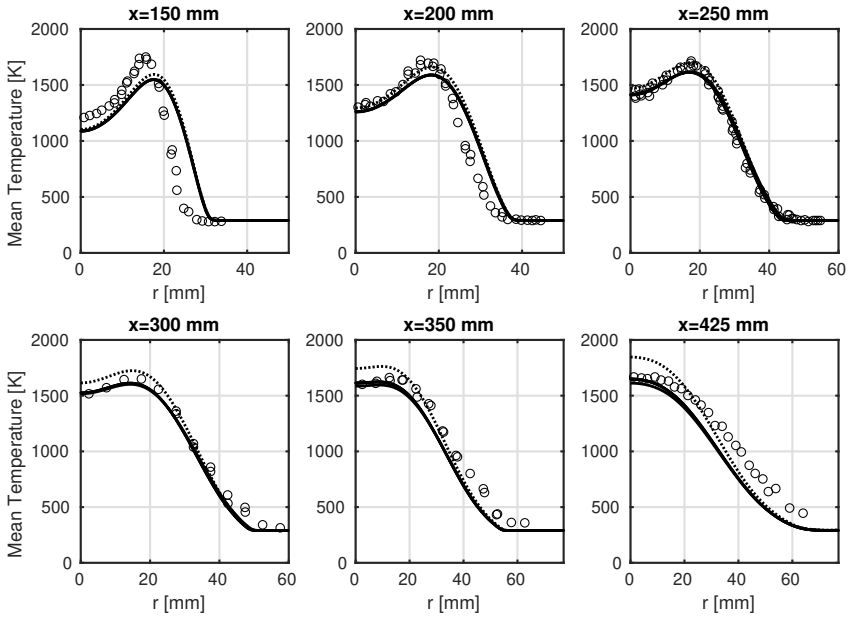

Figure 3.7: Radial temperature - 1 atm. Same legend as in Figure 3.6

the numerical solver.

The centerline soot volume fraction (f_v) is shown in Fig. 3.8. It should be noted that the experimental measurements consist of only three points, therefore it is difficult to know how the experimental distribution is and where f_v reaches its peak. Keeping this in mind, the numerical predictions are seen to be in good agreement with the experimental data. In comparison to the experimental measurements where the highest fv value available is at x = 425 mm, the current simulations yield the peak value located slightly closer to the fuel inlet, at x = 370 mm, with a lower value, approximately 34 % lower. The radial predictions at different axial locations are also shown in Fig. 3.9. The radial profiles show good agreement for different downstream locations with at most 38% discrepancy at x = 425 mm. The predicted soot profiles are similar to what was obtained in the previous RANS-CMC results for the same flame [33]. Kronenburg et al. [33] reported that "The bulky shape of the measured f_v profiles is, however, an artefact of the measurements". They mentioned that the post-processing of the measured data and the conversion into f_v profiles required polynomial curve-fitting. Since the soot concentrations were very low, and the signal-to-noise ratio were high, data allowed a low fourth-order polynomial fit only, and therefore the radial profiles do not accurately reproduce the real shape of f_v in the radial direction. The error in the measurements of mean f_v is reported to be approximately $\pm$ 50% in both (1

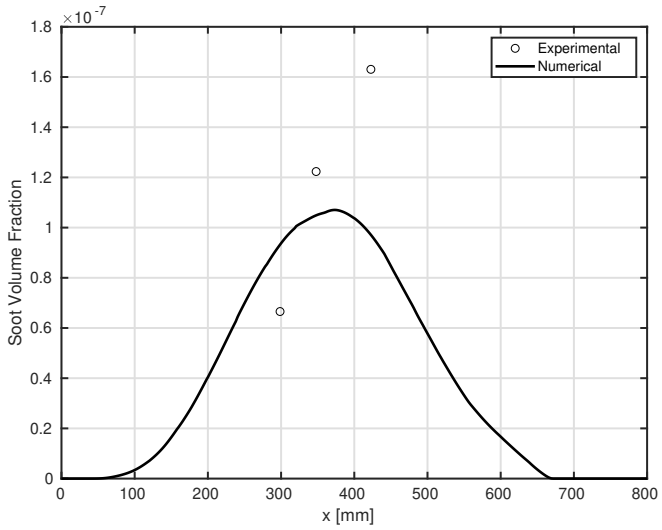

Figure 3.8: Centerline profile for soot volume fraction - 1 atm.

atm and 3 atm) flames [15]. For illustration, the soot volume fraction contour is depicted in Fig. 3.10. No soot contours are given in the experimental study. It can be seen that the peak occurs at an axial location approximately x = 400 mm and the maximum value is close to the centerline. Away from the centerline, f_v decreases. Further, by comparing the contour shape with the contour plot given in [33] it can be seen that both have almost the same distribution. Kronenburg et al. [33] show that soot levels have higher value and extend farther when differential diffusion for soot particles is included compared to the case without the effects of differential diffusion. No further quantitative comparisons are

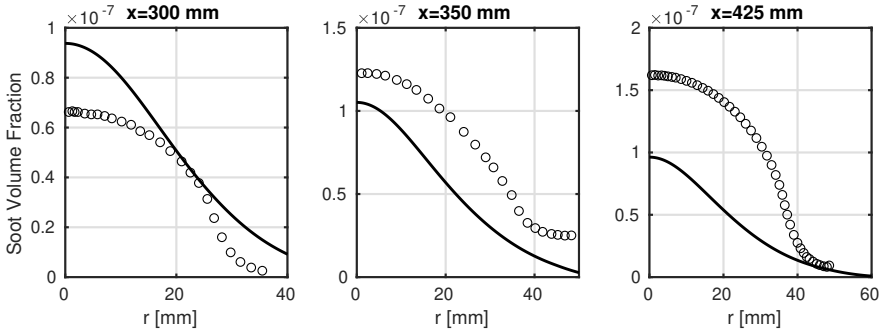

Figure 3.9: Radial profile for soot volume fraction - 1atm. Symbols represent experimental data [15] and the line shows predictions obtained from numerical simulations.

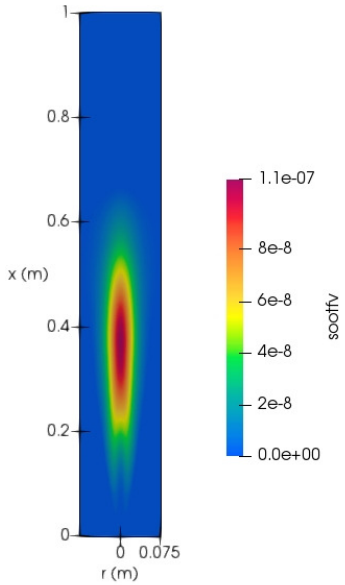

Figure 3.10: Soot volume fraction contour - 1 atm.

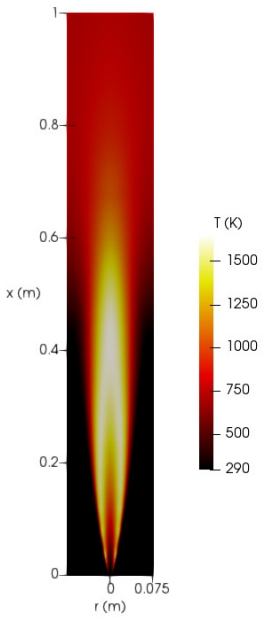

Figure 3.11: Temperature contour - 1 atm.

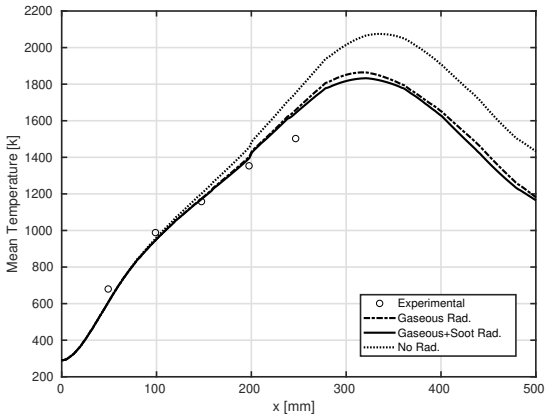

Figure 3.12: Centerline temperature profile - 3 atm.

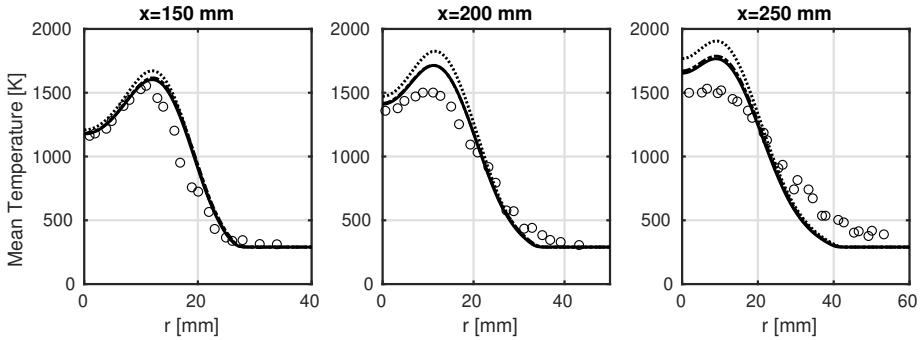

Figure 3.13: Radial temperature profiles - 3 atm. Same legend as in Figure 3.6.

possible with the previously published predictions [33]: published contours do not include a legend showing the levels of f_v obtained.

3.7.2 Flame at 3 atm

No mixture fraction measurements are available, and therefore the predicted mixture fraction profiles are not shown. The centerline temperature predictions can be seen in Fig. 3.12. The total temperature drop due to radiation is approximately 250 K, and the soot radiation portion is approximately 40K (16% of the total temperature decrease due to radiation). The CSE values follow the same trend as what is shown in the experimental data, but the predicted temperature at the last experimental value available (at x=250 mm) is higher by approximately 100K. Further, the predicted flame is longer than the actual flame

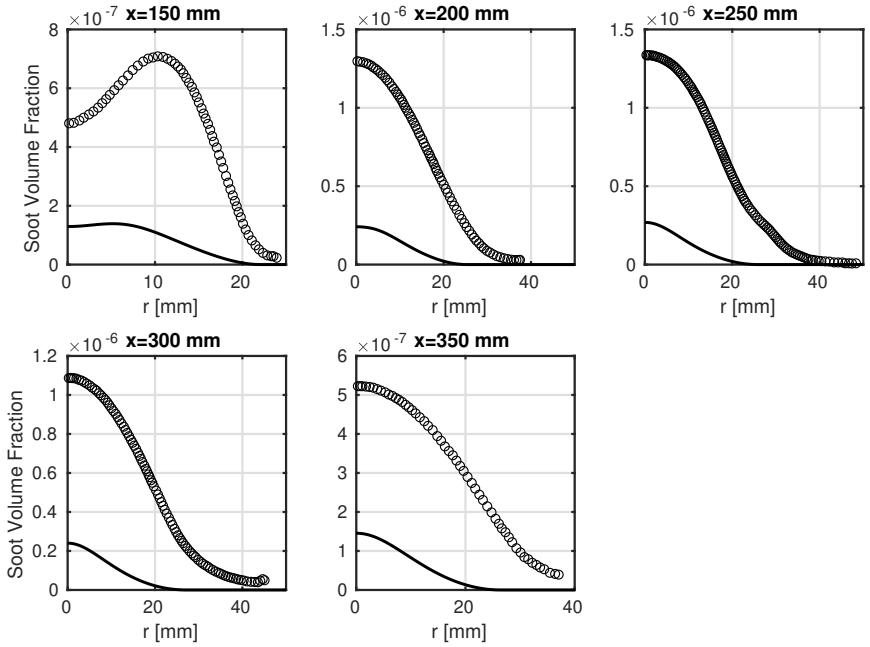

Figure 3.14: Radial soot volume fraction profiles - 3 atm. Symbols represent experimental data [15] and the line shows predictions obtained from numerical simulations.

and the peak temperature occurs at a location farther downstream. The radial temperature predictions are shown in Fig. 3.13. Very good agreement is obtained at x = 150 mm with the centerline and peak temperatures well predicted. However, at x = 200 mm and x = 250 mm the peak temperature is over predicted. The peak temperature location is correctly predicted for these two locations, but the value of the temperature is higher. The temperature discrepancies are believed to be mostly due to the RANS inaccuracies in the turbulent velocity/mixing fields. Inaccuracies in soot concentrations can also have an impact on the predicted temperatures through radiation, as will be seen below, under prediction in soot concentrations would create under prediction of radiative loss and resulting in higher temperature predictions. The radial profiles for f_v are shown in Fig. 3.14. The predictions are all lower than the experimental measurements. The highest discrepancy occurs at the location of x = 250 mm, where the predictions are lower with a factor of 5. The reason can be related to the selection of constants in the soot model as well as the function that relates soot growth term to soot surface area. This semi-empirical model was initially proposed and tested for counterflow ethylene and propane flames and the model constants were determined mostly for ethylene flames. The soot level underprediction is

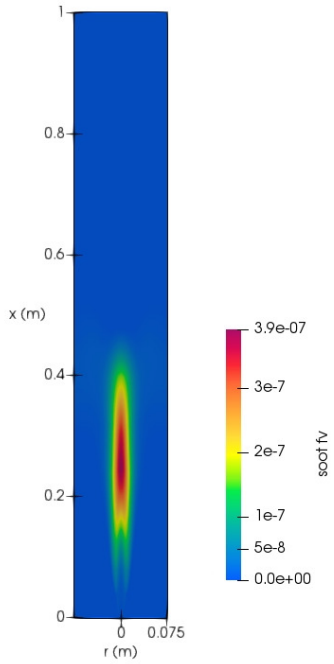

Figure 3.15: Soot volume fraction contour - 3 atm.

also seen for the 1 atm case at axial distances of 350 and 425 mm (Fig. 3.9), but the discrepancies between experimental data and predictions are not high as what is observed in Fig. 3.14. This may also be due to much larger soot levels in the 3 atm flame compared to those at 1 atm. Further, another source of discrepancy may be the neglect of differential diffusion for soot particles in the current study. Kronenburg et al. [33] show that differential diffusion has an impact on the soot volume fraction predictions and improves the simulation results. Many previous investigations also neglected the effect of differential diffusion with reasonable predictions [124, 125, 91]. This needs to be further investigated in the future studies and might be a source of discrepancy in the numerical predictions. For illustration, the soot volume fraction contour (fv) is depicted in Fig. 3.15. The peak value is located on the centerline at an axial distance of approximately 250 mm. Away from the centerline towards the edge of the flame, fv decreases. The temperature contours are shown in Fig. 3.16. By comparing the temperature and soot volume fraction contours with those for 1 atm, it can be seen that the flame is thinner. This is in qualitative agreement with the experimental findings [15]. Soot formation also depends on the concentrations of C_2H_2, O_2, and OH. Therefore, the conditional mass fractions of C_2H_2 and OH which are used in the calculation of the soot source terms, are shown in Fig. 3.17 at the location x

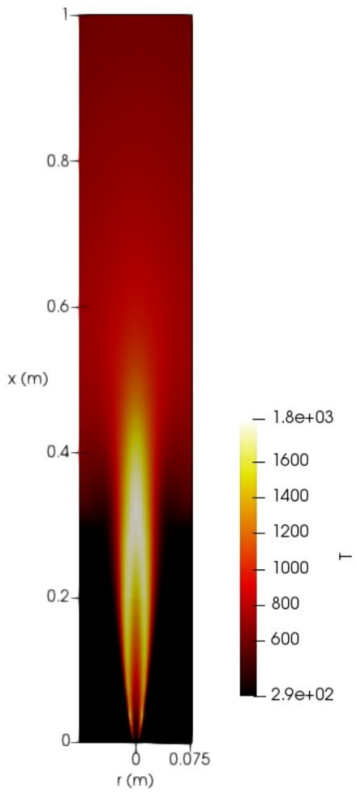

Figure 3.16: Temperature contour - 3 atm.

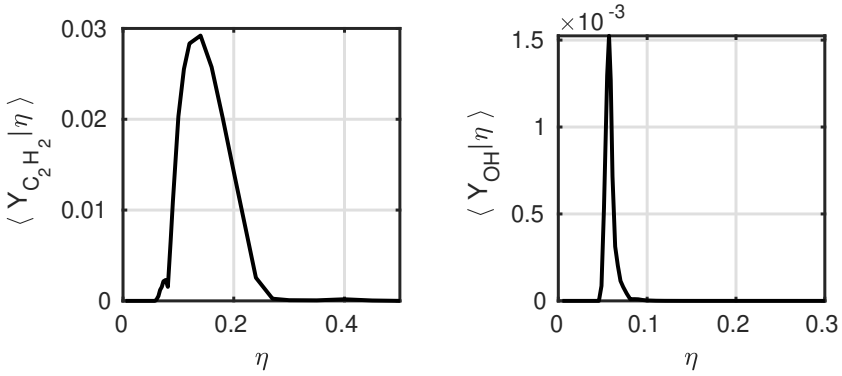

Figure 3.17: Conditional mass fraction of species responsible for soot processes at location x = 250 mm - 3 atm.

= 250 mm. Since experimental results are not provided for species concentrations in [15], the conditional mass fractions of C_2H_2 and OH are qualitatively compared with the results of [33, 126]. The shape of the profiles as well as the maximum values are in the same order of magnitude as that of profiles included in [33]. The peak for C_2H_2 mass fraction is approximately 0.029 at a mixture fraction value of 0.14. Increased soot formation is expected in the fuel rich mixture regions. Therefore, having the peak value for acetylene, the soot precursor, at a mixture fraction greater than stoichiometric, seems to be reasonable. Also, as expected, OH mass fraction reaches its peak of 1.5×10^{-3} at a mixture fraction close to the stoichiometric mixture fraction. These profiles and their values confirm that the calculated conditional mass fractions of the species required for the soot calculations, reproduce the expected trends. Figure 3.18 illustrates the corresponding contributions of the various source terms for the soot mass fraction in conditional space at the peak soot location (x=250 mm). It can be seen that surface growth has the greatest contribution, while the effect of nucleation is very low. This is in agreement with the findings of [91]. The effect of O_2 and OH oxidation source terms are almost the same in terms of their value, although OH oxidation term is present at higher mixture fraction values compared to O_2 oxidation term. Figure 3.19 shows the sensitivity of the soot model to various soot model constants along the centerline of the 3 atm flame. This flame is selected for sensitivity analysis because the levels of soot are higher than those at 1 atm. The pre-exponential factor for nucleation rate, and surface growth rate have been varied by a factor of 10 and 2 respectively, one at a time. Also, considering the effect of soot surface growth as a function of soot surface area (not square root function) is depicted. The soot model is most sensitive to the surface growth rate constant, whereby multiplying the original constant in a factor of two, the peak soot volume fraction increases almost by a factor of two. Nucleation constant does not show strong sensitivity on the soot volume fraction (approximately 7%).

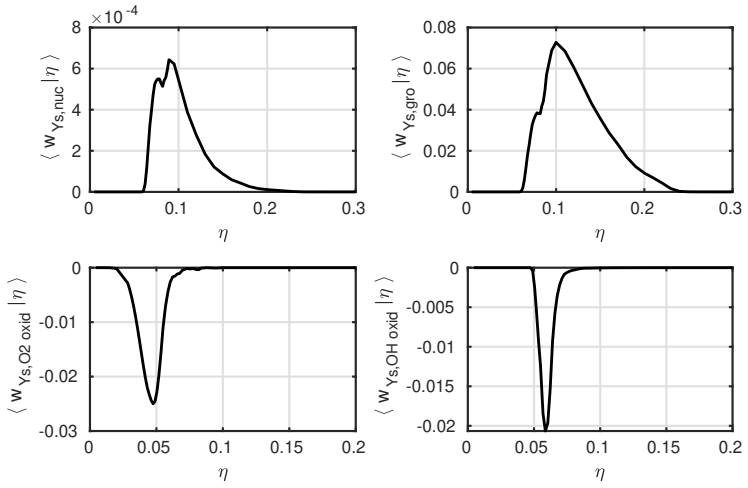

Figure 3.18: Contributions for conditional soot mass fraction at location x = 250 mm $[kg/m^3.s]$ - 3 atm.

By changing the dependency of soot surface growth from square root of soot surface area to surface area, the soot peak soot volume fraction increases approximately 36%. It should be noted that because the aim of this study was not to perform model constant calibration to acquire accurate predictions for all experimental conditions, the results shown for soot volume fraction are simulated using the model constants given in Table 3.1. This approach allows for the assessment of the capability of the CSE framework coupled with the soot model.

3.8 Summary

The semi-empirical model of Leung et al. [92] is coupled with CSE in RANS. Predicted mixture fraction, temperature and soot volume fraction are compared with available measurements for two turbulent flames (1 atm and 3 atm). For mixture fraction and temperature, good agreement with the experimental data is obtained with some discrepancies identified, mostly due to the limitations of RANS to correct the flame spreading rate. At 1 atm, the soot f_v is also in good agreement with the experimental data within the experimental uncertainty. At 3 atm, although reasonable agreement is found between the predicted f_v and measurements and she shape of the soot profile and the location of the peak point for soot volume fraction are well predicted, but under prediction can be seen for soot f_v in all locations. These may be explained by the use of k-ε, experimental errors,

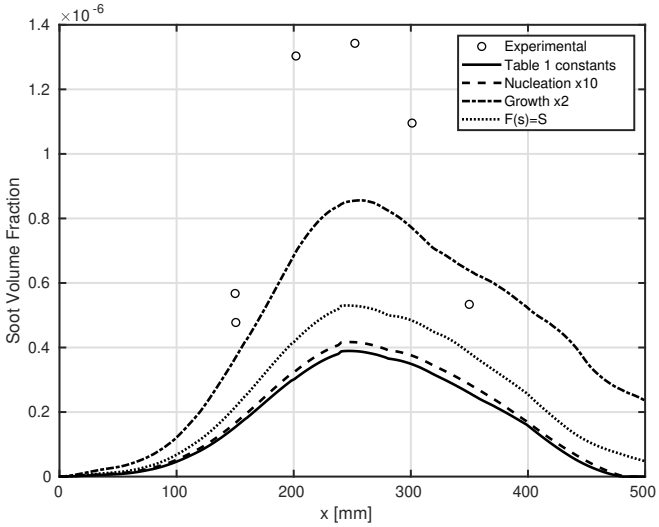

Figure 3.19: Effect of soot model constants on soot volume fraction along the flame centerline in 3 atm flame. Symbols denote experimental measurements, lines denote CSE calculations: predictions using Table 3.1 constants (solid), soot nucleation source term multiplied by 10 (dashed), soot surface growth source term multiplied by 2 (line dot), and soot growth source term as a function of soot surface area (dotted).

lack of differential diffusion in the current model and the pre-exponential rate constants that have not been specifically determined for these two methane-air flames. In the future, a more detailed soot model instead of a simple semi-empirical model will be investigated. The first application of a semi-empirical soot model implemented in the framework of CSE suggests that CSE is a promising approach for soot modeling in turbulent diffusion flames.

Chapter 4

CSE using non-adiabatic chemistry tabulation

In this chapter, the non-premixed CSE-soot formulation from Chapter 3 is extended to include an enthalpy variable in the TGLDM tabulation. In Chapter 3 it was shown that CSE can accurately predict the flame characteristics of non-premixed flames for the Brookes and Moss flames at 1 and 3 atm. The results for temperature prediction were very good for 1 atm flame which has low radiative heat loss but for the 3 atm flame some overpredictions could be observed. This is due to the fact that the 3 atm flame has a high radiative heat loss. The objective of the current chapter is to determine if a CSE-soot formulation including non-adiabatic TGLDM tables provide a better temperature prediction compared to those in adiabatic conditions.

4.1 CSE formulation with radiation

Similar to the CSE formulation from Chapter 3, the conditional mass fractions of CO_2 and H_2O are obtained, as outlined in Section 3.1 and 3.2. In addition, to have another input to the TGLDM tables as a quantity representing the level of radiation, i.e., the enthalpy loss, the conditional enthalpy is selected as the new added parameter to the tables. For this purpose, after the enthalpy is calculated in the CFD solver, the value is taken and the conditional enthalpy is calculated by inverting the following integral

$$\widetilde{h}(x_j,t) = \int_0^1 \big\langle h|\eta \big\rangle(\eta,t)\widetilde{P}(\eta,x_j,t)d\eta, \tag{4.1}$$

where $\widetilde{h}$ and $\widetilde{P}(\eta)$ are known quantities determined by solving a transport equation and the β-PDF function [104] respectively. With the addition of the conditional enthalpy the TGLDM manifolds are tabulated as a function of mixture fraction, CO_2 and H_2O mass fractions, and enthalpy and the mean chemical source term can be retrieved using

$$\overline{\dot{\omega}_k}(x_j,t) = \int_0^1 \frac{\langle \dot{\omega}_k|\eta\rangle(\langle CO_2|\eta\rangle, \langle H_2O|\eta\rangle, \langle h|\eta\rangle)}{\langle \rho|\eta\rangle} \widetilde{P}(\eta, x_j, t)d\eta. \tag{4.2}$$

The flow chart diagram for CSE method using non-adiabatic tables is shown in Fig. (4.1).

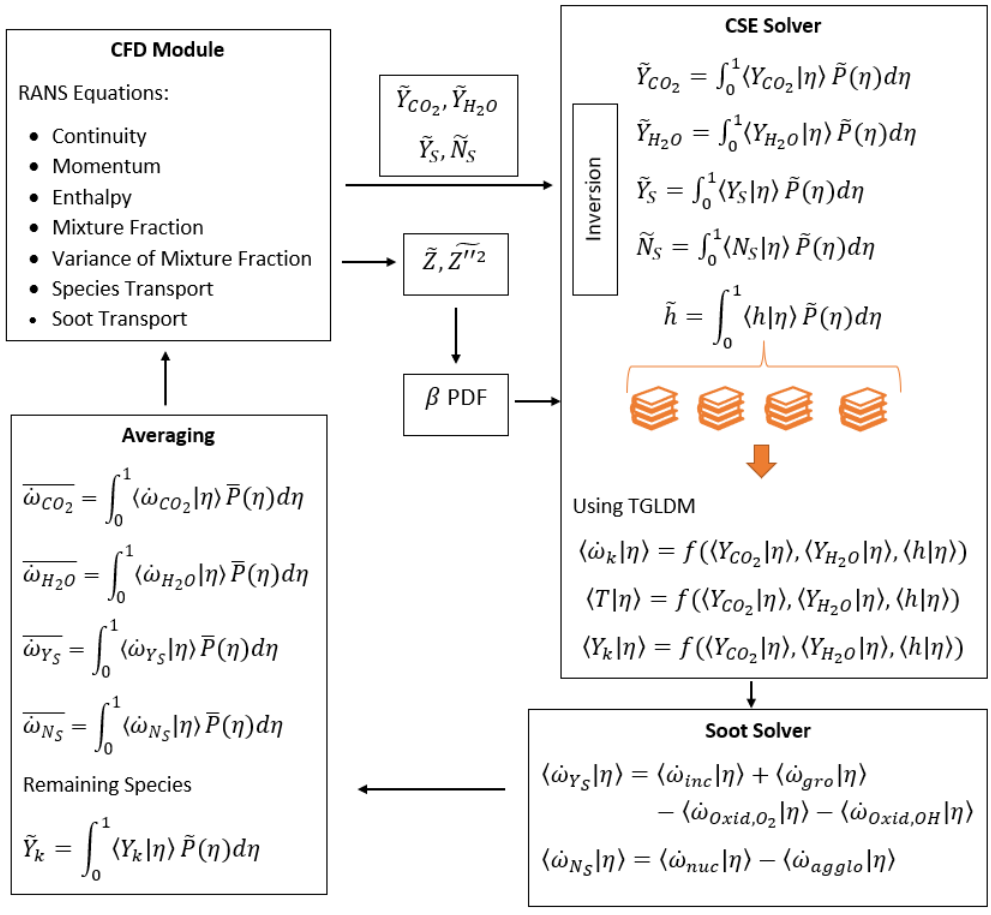

Figure 4.1: flow chart diagram for CSE method using non-adiabatic tables

4.2 Chemistry tabulation

Before starting the simulations, chemistry tables are generated using the TGLDM method [102] for reducing the computational time. This time the manifolds are stored as a function of four variables: mixture fraction, enthalpy, CO_2 and H_2O mass fractions. The detailed kinetic mechanism of GRI 3.0 [112] which is widely used for methane-air combustion is employed. The unconditional chemical source term is obtained using

$$\overline{\dot{\omega}_k}(x_j,t) = \int_0^1 \frac{\langle \dot{\omega}_k^{TGLDM}|\eta\rangle}{\langle \rho|\eta\rangle}(\eta,x_j,t)\widetilde{P}(\eta,x_j,t)d\eta, \tag{4.3}$$

where

$$\langle \dot{\omega}_k^{TGLDM}|\eta\rangle = f(\langle CO_2|\eta\rangle, \langle H_2O|\eta\rangle, \langle h|\eta\rangle). \tag{4.4}$$

In order to have the tables as a function of h, the tables are generated using different values of absolute enthalpy for each value of mixture fraction. To generate a new set of tables, the absolute enthalpy corresponding to adiabatic conditions is no longer used and a modified value of enthalpy is set for the manifold, and the trajectories would be calculated based on this new value of enthalpy. It should be noted that the tables are based on absolute enthalpy and OpenFOAM uses sensible enthalpy for calculating temperature. The relation between absolute and sensible enthalpy is given as

$$h_{abs,i}(T) = h^{\circ}_{f,i}(T_{ref}) + \triangle h_{s,i}, \tag{4.5}$$

where $h_{abs,i}(T)$ is the absolute enthalpy or total enthalpy, $h^{\circ}_{f,i}(T_{ref})$ is the enthalpy of formation at standard reference state (enthalpy that takes into account energy associated with chemical bonds), and $\triangle h_{s,i}$ is the sensible enthalpy change from temperature T_{ref} to T (enthalpy associated only with T). The standard state is considered at T_{Ref}=298.15 K and P=1 atm.

The absolute enthalpy has a negative value, while the sensible enthalpy is positive and becomes greater by increasing the temperature. The absolute enthalpy which is the sum of heat of formation and sensible enthalpy has a negative value. Hence, once the temperature of a product gas of a combustion process reduces (by radiation), its absolute enthalpy would become lower (a larger negative value). Therefore, to include the effect of radiation, the absolute enthalpy in the new tables is multiplied by a factor, to make it less (more negative). For example, for the stoichiometric mixture fraction, η_{st}=0.055, the first set of tables is for the adiabatic case, with no enthalpy loss (as in Chapter 3). The next set of tables is for the case where the absolute enthalpy value for the calculations of the manifold

Table 4.1: Temperature changes for the stoichiometric mixture fraction caused by changing the absolute enthalpy of the mainfold using different multiplication factors

Multiplication factor	$h_{abs}(J/kg)$	Max. temp. (K)	Temp. difference (K)
×1 (adiabatic case)	-253796.26	2322.16	0
×1.5	-380694.39	2238.65	83.51
×2	-507592.52	2154.76	167.4
×2.5	-634490.64	2070.45	251.7
×3	-761388.77	1985.67	336.5

is multiplied by a factor 1.5. In this case, the maximum temperature in the manifold would decrease by 83.51 K. The next set of tables is for the case where a multiplication factor of 2 is used, and so on up to a value of 3. The tables are generated for five different values of enthalpy loss (changing the absolute enthalpy of the mixture) and checked to make sure the inverted enthalpy is not outside the tabulated values. The temperature changes for the stoichiometric mixture fraction caused by changing the absolute enthalpy of the mixture using different multiplication factors is given in Table (4.1).

Fig. (4.2) shows the temperature distribution inside a manifold based on the mass fractions of CO_2 and H_2O. As shown in Fig. (4.2), the temperature starts to rise in the manifold by the increase in the values of CO_2 and H_2O mass fractions. Because radiation takes place mostly at high temperatures, the code for generating the non-adiabatic TGLDM tables is designed in a way that reduces the temperature of a trajectory once it goes above 1000 K. After a certain value along a trajectory, the enthalpy is forced to change to account for the enthalpy loss. This change is by multiplying the original enthalpy (corresponding to adiabatic case) in different constants given in Table (4.1). Therefore, a sudden jump can be see in the temperature distribution of the trajectories. This break (sudden change in enthalpy value) can also be seen in the visualized trajectories in a manifold (4.3).

4.3 Results

4.3.1 Temperature

To see the effect of using non-adiabatic chemistry tables for a high radiating flame, i.e., Brookes and Moss flame operating at 3 atm pressure, the centerline temperature profiles

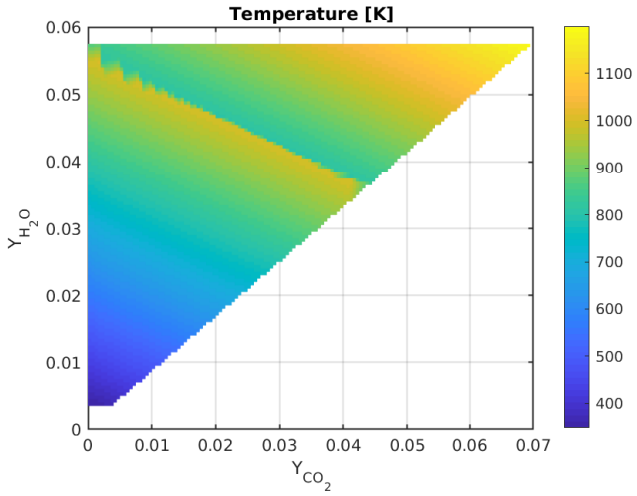

Figure 4.2: Temperature distribution accross the trajectories in a manifold

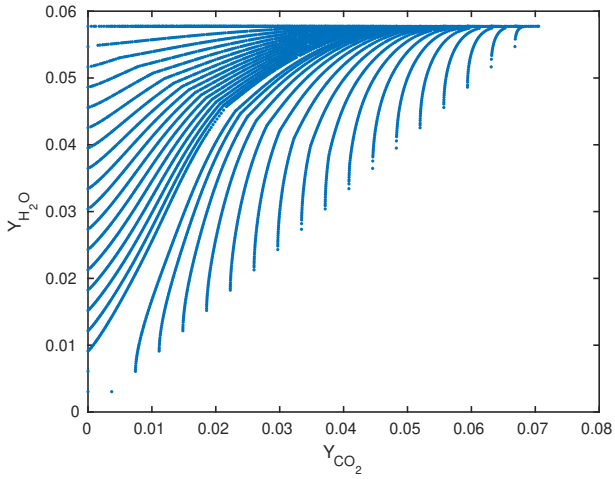

Figure 4.3: Trajectories in a manifold evolving towards the equilibrium point

using adiabatic and non-adiabatic tables are shown in Fig. (4.4).

It can be seen that the temperature predictions have improved significantly using the non-adiabatic chemistry tables. The peak temperature from experimental results is approximately 1500 K and the numerical predictions using adiabatic tables had an overprediction of approximately 300 K. But now using the non-adiabatic tables, the peak temperature

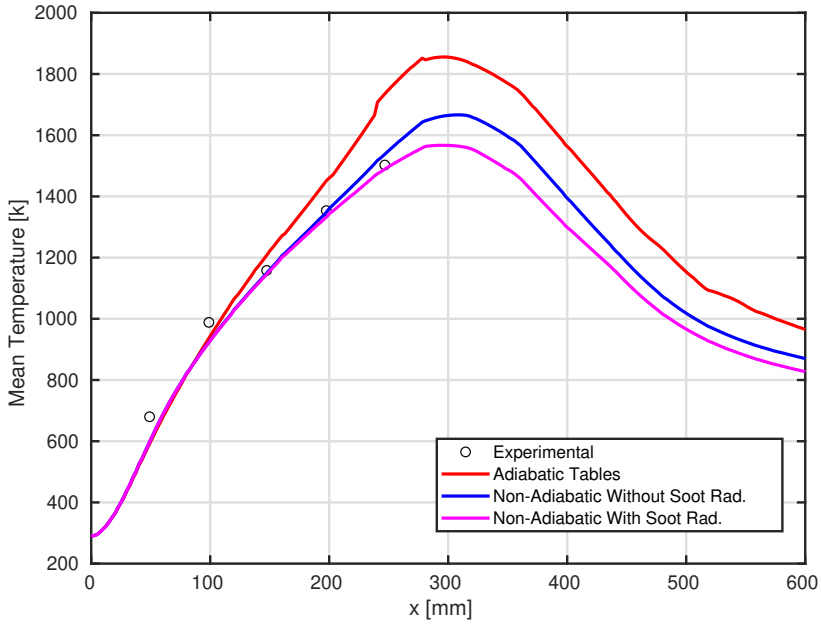

Figure 4.4: Centerline temperature profile using adiabatic and non-adiabatic chemistry tables compared with experimental results [15]. Red line corresponds to predictions using adiabatic tables; Blue line shows predictions using non-adiabatic tables but soot radiation was not included in temperature calculation; purple line shows predictions using non-adiabatic tables and includes the effect of soot radiation in temperature calculations.

prediction (approximately 1560 K) is very close to the experimental value and shows the improvement gained in the temperature prediction. Also, it can be seen that soot radiation has decreased the peak temperature by approximately 100 K. By considering the peak temperature of the flame without any radiation approximately 2100 K, it can be concluded that the portion of soot radiation to the total temperature loss due to radiation is approximately 19 %. Also the radial profiles for temperature predictions at different locations are given in Fig. (4.5). It can also be seen that the radial profiles show significant improvement especially at the regions close to the center of the flame. The numerical predictions are in very good agreement with experimental data for axial locations x=150 mm and 200 mm. At x=250 mm the predictions are very good close to the peak temperature, but moving in the radial direction, away from the centerline, numerical results slightly under predict the temperature values.

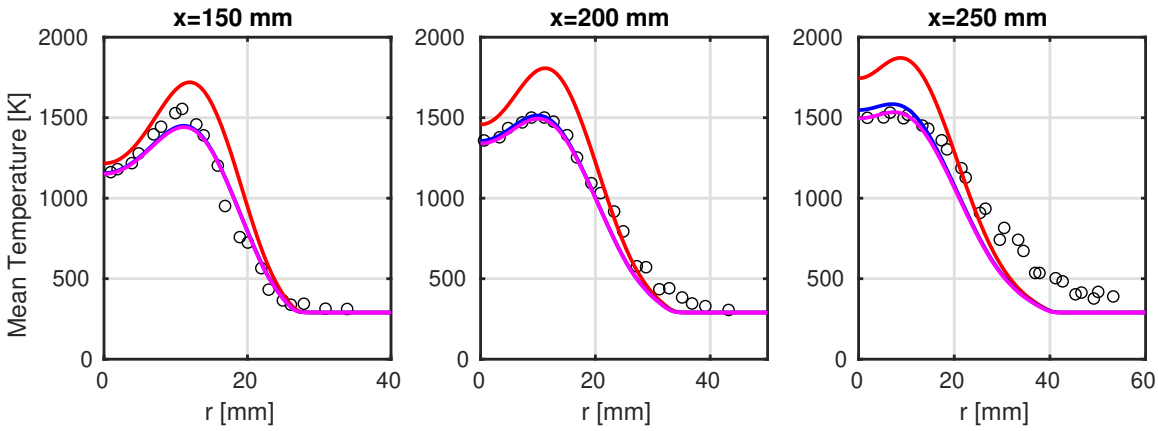

Figure 4.5: Radial temperature profiles using adiabatic and non-adiabatic chemistry tables compared with experimental results [15]. Red line corresponds to predictions using adiabatic tables; Blue line shows predictions using non-adiabatic tables but soot radiation was not included in temperature calculation; purple line shows predictions using non-adiabatic tables and includes the effect of soot radiation in temperature calculations.

4.3.2 Soot volume fraction

In this section the predicted values for soot volume fraction are presented with the implementation of non-adiabatic chemistry tables. The soot volume fraction across the flame centerline is shown in Fig. (4.6).

It can be observed that the predicted centerline soot volume fraction shows good agreement with experimental data. The peak location and value are very well predicted although the location of the peak is predicted at x=300 mm, compared to x = 250 mm in the experimental profile. Moreover, the size of the soot region is slightly larger than what the trend of experimental data shows. This indicates that the soot is not sufficiently oxidized and eliminated from the flame at downstream locations. But the overall predictions for soot are in very good agreement with experimental findings. To better compare the numerical predictions with experimental data, the radial profiles for soot volume fraction are also depicted in Fig. (4.7) for different axial locations in the burner. The predicted radial profiles of soot volume fraction also show very good agreement with experimental data.

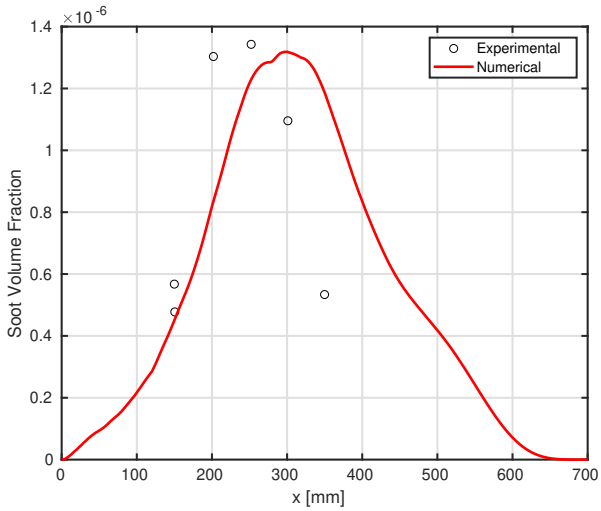

Figure 4.6: Soot volume fraction across the flame centerline using non-adiabatic tables compared with experimental results [15] in 3 atm flame.

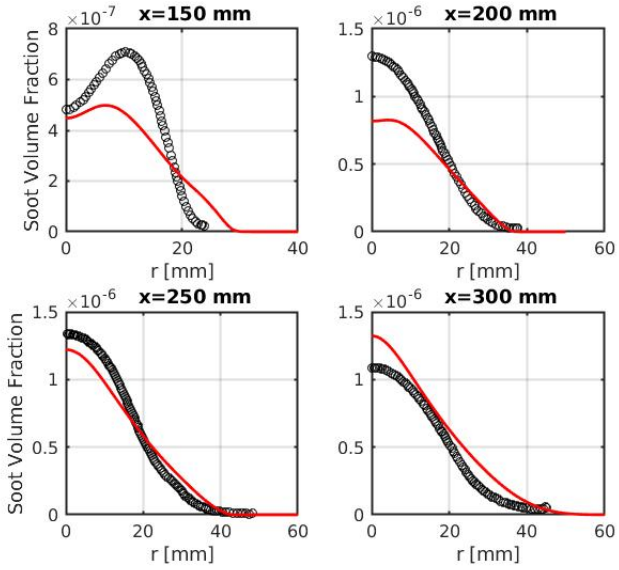

Figure 4.7: Radial soot volume fraction profiles at different locations of the flame using non-adiabatic tables compared with experimental data [15] in 3 atm flame.

4.4 Summary

For flames with high radiation it is necessary to include the effects of soot and gaseous radiation in the chemistry tabulation process for better prediction of the flame characteristics. Since the Brookes and Moss flame at 3 atm pressure [15] has been reported to have high levels of radiation and the temperature values showed over prediction in Chapter 3, it was deemed necessary to investigate the effect of non-adiabatic chemistry tables on the numerical predictions of this flame. For this purpose, the CSE-semi-empirical soot model formulation presented in Chapter 3 is extended to take use of non-adiabatic tables generated prior to the simulations. A new parameter, enthalpy, is added to the TGLDM tables as and extra input to represent the amount of loss due to radiation. Predicted temperature and soot volume fraction are compared with experimental data and also the predictions obtained using adiabatic chemistry tables (without the effects of heat loss from radiation). The predictions for temperature and soot volume fraction show very good agreement with experimental data and compared to adiabatic chemistry, simulations with non-adiabatic tabulation show significant improvement.

Chapter 5

CSE-Quadrature Method of Moments (QMOM) for soot aerosol dynamics

In this chapter, the soot aerosol dynamics and particulate flow is explained. Different strategies for solving the population balance equation that governs the disperse phase of soot particles are compared and described. In particular, Quadrature Method of Moments (QMOM) and Quadrature Method of Moments with fixed quadrature points at the soot particle inception size, so-called QMOM-Radau closures, are explained. The CSE turbulent combustion computational framework for turbulent flames is extended to allow for the treatment and solution of quadrature-based moment closures for describing the soot aerosol dynamics and simulating soot formation in turbulent non-premixed flames.

5.1 Introduction

The simulation of flames with soot requires knowledge of disperse multiphase flows. The development of computational models for disperse multiphase flows has focused on two different aspects [127]: (i) the evolution of the disperse phase (e.g. particle–particle collisions) and (ii) multiphase fluid dynamics. The first category of models, which is the focus of this chapter, deals mainly with the description of the disperse phase, and is based on the solution of the spatially homogeneous population balance equation (PBE). The statistical behavior, distribution and evolution of the disperse phase (soot particles) is governed by

the population balance equation (PBE) [127, 128]. The PBE is a continuity equation that is based on the number density function (n) which is explained in the next section. Solving the PBE is difficult because of the high dimensionality of the problem. It involves modelling of different processes such as the inception (or nucleation) of new particles from the gase-phase chemistry, coalescence of existing particles into larger particles, or aggregation of particles into larger fractal-shaped agglomerates, surface growth by chemical reactions, and the oxidation of soot particles by OH and O_2. There are different methods for solving this complex equation: one strategy for solving the PBE is using particle methods where a number of representative particles are introduced. Such methods are referred to as stochastic or Monte Carlo (MC) methods [79, 129, 130, 131]. Although MC methods are very accurate, but they can only be applied to very simple configurations because of their relatively high computational cost. Another approach used for solving PBE equation is the category known as sectional methods (SM) or class methods (CM) [132, 133, 134]. In this approach, the distribution function is discretized into bins or classes and then a transport equation for each of these discrete parts is solved. Furthermore, moment closure or method of moments (MOM) [82, 83, 135, 84, 136] is another alternative approach that only requires the solution of only a few transport equations for moments of the soot particle distribution function. This method is not as accurate as Monte Carlo and sectional methods, however, in terms of accuracy and computational cost, it offers a good compromise. Such technique may therefore be more suitable for application in turbulent flames and practical engineering applications. Finally, the Quadrature Method of Moments (QMOM) is known as a particular category of moment methods where the closure problem is solved by using a quadrature approximation [137, 135].

5.2 Disperse particulate aerosol dynamics

5.2.1 Population Balance Equation

The description of the disperse phase, i.e, soot particles, is based on the solution of the population balance equation (PBE). A PBE is a continuity governing equation written in terms of a number density function (NDF) [127]. When using an Eulerian approach, the disperse phase is generally described by an NDF. The NDF describes how the population formed from the discrete elements of the disperse phase is distributed over certain characteristic properties (for example size/volume). In other words, the NDF contains information about how the population of particles inside an infinitesimal control volume is distributed over the properties of interest and is given as

$$n = n(x, t, \varepsilon), \tag{5.1}$$

and the population balance equation (PBE) governing the NDF is given as [138]

$$\frac{\partial n(x,t,\varepsilon)}{\partial t} + \frac{\partial}{\partial x_j}\left((u_j + V_{T_j})n(x,t,\varepsilon)\right) - \frac{\partial}{\partial x_j}\left(D_s \frac{\partial n(x,t,\varepsilon)}{\partial x_j}\right) = \left.\frac{\mathrm{d}n(x,t,\varepsilon)}{\mathrm{d}t}\right|_{nuc+sg+coag+oxid} \tag{5.2}$$

where x is the vector of space, ε is the parameter for internal coordinates, characterizing the soot particles (e.g., particle volume, V). u_j is the flow velocity, D_s is the soot diffusion coefficient, and V_T is the thermophoretic velocity of the particles. On the right-hand side of Eq. (5.2), there is a source term for the PBE that represents various effects including nucleation (nuc), surface growth (sg), coagulation (coag), and oxidation (oxid).
Usually coordinates are classified as internal and external. External coordinates are spatial coordinates (the position of the elements in physical space). Internal coordinates refer to more intimate properties of the elements such as their momenta (or velocities), their enthalpy (or temperatures), or their volumes, surface areas, or sizes. The internal coordinates (ε) allow a description of the characteristic of the aerosol. When only one size parameter is selected (ex: volume or diameter), only spherical particle can be considered while when several parameters are selected (ex: surface and volume), aggregate structure can be considered.
As described in the Introduction, since the resolution of the PBE is difficult, a good and efficient strategy for solving this complex equation may be the method of moments (MOM) that is going to be described in the next section.

5.3 Method of Moments

Solving directly the PBE for getting a solution of the NDF will rarely be possible for complicated industrial and environmental flows. Instead, other models whose solutions are consistent with the moments of the NDF are of interest. MOM methods are formulated in terms of transport equations for the moments of the NDF, and later, accurate closures for the moment transport equations, preferably using only the smallest possible moment set would be required.

Considering a population of disperse solid particles inside an infinitesimal control volume located at the physical point $x = (x_1, x_2, x_3)$ and of measure $dx = dx_1.dx_2.dx_3$. Let

$\varepsilon(\varepsilon_1, \varepsilon_2, ..., \varepsilon_M)$ be the internal coordinate vector, namely the vector containing the M internal coordinates of interest. The NDF $n_\varepsilon(t, x, \varepsilon)$ is defined as the expected number of entities in the infinitesimal physical volume dx and in the infinitesimal phase-space volume $d\varepsilon$. A very common internal coordinate for particulate systems is the particle volume. Therefore, the volume based NDF would be the number of particles with volume between V and $V + dV$. In this study the internal coordinate will be considered the volume of particles, $\varepsilon = V$. Therefore, the NDF will be

$$n = n_V(t, x, V). \tag{5.3}$$

If the NDF is integrated over all possible values of the internal-coordinate (V), the total number concentration would be obtained by

$$N = M_{V,0} = \int n_V(V) dV, \tag{5.4}$$

which is the total number of particles per unit volume located at time t and point x, and corresponds to the zeroth-order moment of the density function. In a similar way, the k-order moment of the NDF is given as

$$M_{V,k} = \int V^k n_V(V) dV, \tag{5.5}$$

MOM is a method that consists of integrating the population balance equation in phase (internal coordinates) space and solving transport equations of the moments rather than solving the PBE itself. Such approaches are computationally less expensive, making them the choice for turbulent flame calculations. The method of moments is very popular in the literature and many different methods have been introduced, such as the Method of Moments with Interpolative Closure (MOMIC) [82, 83], the Quadrature Method of Moments (QMOM) [137, 135], the Extended Quadrature Method of Moments (EQMOM) [139, 140], and the Conditional Method of Moments (CQMOM) [141]. While several of these moment methods have been used for soot prediction, in this study the focus will be on QMOM methods. Recently Xing et al. [138] performed comparisons of the predictive capabilities of the various moment techniques to each other and other methods used for aerosol dynamics. They have proposed both univariate Quadrature Method of Moments (QMOM) and bivariate Conditional Quadrature Method of Moments in terms of fractional-order soot particle size moments with fixed quadrature points at the soot particle inception

size, so-called QMOM-Radau and CQMOM-Radau moment closures, and have shown that such closures can significantly improve the accuracy of the prediction of number density and volume fraction. These recently proposed quadrature-based moment closures involve the solution of just a small system of moment equations (5 and 7 equations for the QMOM-Radau and CQMOM-Radau closures, respectively). Their results show that QMOM-Radau method using 5 moments provides very good results for soot number density and volume fraction. Hence, in this study the QMOM-Radau which is described in the next section will be adopted.

5.4 Quadrature Method of Moments (QMOM)

Quadrature Method of Moments (QMOM) [137, 135] represent the distribution function as a sum of Dirac delta functions and can be used for univariate, bivariate, or multivariate descriptions. For a univariate description with $\varepsilon = V$, the soot is represented as a poly-disperse aerosol of spherical particles and the corresponding approximate distribution is defined by

$$n(V) = \sum_{\alpha=1}^{N_V} n_\alpha \delta(V - V_\alpha), \tag{5.6}$$

and the k^{th}-order volume moment is then given by

$$M_k = \sum_{\alpha=1}^{N_V} n_\alpha V_\alpha^k, \tag{5.7}$$

where N_V is the number of volume Dirac function, n_α are the weights, and V_α are the volume abscissa. The weights and abscissa of the Dirac functions defining the approximated distribution for soot particle size can be evaluated directly from a set of $2N_V$ known moments via a moment-inversion algorithm, which will be explained. Additionally, it would be necessary to solve moment transport equations and then close the source terms of the moment transport equations by direct quadrature.
Also, as described earlier, for univariate MOM, the moments of the NDF will appear as

$$M_k = \int_V V^k n_V(V) dV, \tag{5.8}$$

where n_V is the unknown univariate NDF. The closure problem can be solved by any numerical scheme that is able to accurately calculate the integral equation 5.8. It should

be noted that because the NDF is unknown, and only its moments are transported and therefore known, the numerical scheme for solving the closure must be constructed starting from the transported moments of the NDF. The Gaussian quadrature is one scheme for this purpose. Before discussing the details of the quadrature method some preliminary concepts must be introduced. In Gaussian quadrature theory the NDF is called the weight function. The weight function must be non-negative and non-null in the integration interval and all its moments [127]. Another important definition is the orthogonal polynomials. A set of polynomials given as $P_0(V), P_1(V), ..., P_\alpha(V), ...$ with knowing that

$$P_\alpha(V) = k_{\alpha,0}x^a + k_{\alpha,1}x^{a-1} + ... + K_{\alpha,\alpha}, \tag{5.9}$$

is said to be orthogonal in the integration interval V, with respect to the weight function, if

$$\int_V n(V)P_\alpha(V)P_\beta(V)dV \begin{cases} = 0 & for \quad \alpha = \beta \\ > 0 & for \quad \alpha \neq \beta \end{cases} \tag{5.10}$$

One useful point in terms of polynomials is the fact that any set of orthogonal polynomials $P_\alpha(V)$ has a recurrence formula relating any three consecutive polynomials as [127]

$$P_{\alpha+1}(V) = (V - a_\alpha)P_\alpha(V) - b_\alpha P_{\alpha-1}(V), \quad \alpha = 0, 1, 2, ... \tag{5.11}$$

with $P_{-1}(V) = 0$ and $P_0(V) = 1$ and where

$$a_\alpha = \frac{\int_V n(V)VP_\alpha(V)P_\alpha(V)dV}{\int_V n(V)P_\alpha(V)P_\alpha(V)dV}, \quad \alpha = 0, 1, 2, ..., \tag{5.12}$$

$$b_\alpha = \frac{\int_V n(V)P_\alpha(V)P_\alpha(V)dV}{\int_V n(V)P_{\alpha-1}(V)P_{\alpha-1}(V)dV}, \quad \alpha = 1, 2, ... \tag{5.13}$$

The recursive relation is a very important property for constructing the polynomials and computational purposes. In fact, the zeros of the orthogonal polynomials can be computed and with them the quadrature rule. a_0 can be calculated from Eq. (5.12), then $P_1(V)$ from Eq. (5.11). Knowing $P_0(V)$ and $P_1(V)$, a_1 and b_1 can be calculated from Eqs. (5.12) and (5.13), and so on. Eventually the coefficients a_α and b_α can be written in terms of the moments of the NDF. Also, the coefficients required for the construction of a polynomial of order N can be calculated from the first $2N - 1$ moments of the NDF, that

is $M_0, M_1, ..., M_{2N-1}$. As an example, with M_0, M_1, M_2, and M_3, it is possible to calculate the following coefficients

$$a_0 = \frac{M_1}{M_0}, \tag{5.14}$$

$$a_1 = \frac{M_3 M_0^2 + {M_1}^3 - 2M_2 M_1 M_0}{M_2 M_0 + {M_1}^2 - 2{M_1}^2 M_0}, \tag{5.15}$$

$$b_1 = \frac{M_2 M_0 + M_1^2 - 2M_1^2 M_0}{M_0^2}, \tag{5.16}$$

which suffice for the calculation of the polynomial $P_2(V)$ (of order two) orthogonal to the weight function. The reason for the interest in the orthogonal polynomials is that their roots are the nodes of Gaussian quadrature approximations.

A very simple way to overcome the closure problem in Eq. (5.8), is to resort to an interpolation formula [127]

$$\int_V n(V)g(V)dV \approx \sum_{\alpha=1}^{N} w_\alpha g(V_\alpha), \tag{5.17}$$

where w_α and V_α are respectively, the weights and the nodes of the interpolation formula, N is the number of nodes used for the interpolation, and $g(V)$ is a functional grouping together all the terms appearing in the integral apart from the NDF.
A Gaussian quadrature is an interpolation formula whose N nodes are the roots of the polynomial $P_N(V)$ orthogonal to the weight function $n(V)$ [127].
As a Gaussian quadrature of order N has a degree of accuracy of $2N-1$, it is the only approximation that can capture the first $2N-1$ moments of the weight function. Therefore,

the N weights and N abscissas can be determined by solving the following nonlinear system:

$$M_0 = \sum_{\alpha=1}^{N} w_\alpha, \tag{5.18}$$

$$M_1 = \sum_{\alpha=1}^{N} w_\alpha V_\alpha, \tag{5.19}$$

$$\vdots \tag{5.20}$$

$$M_{2N-2} = \sum_{\alpha=1}^{N} w_\alpha V_\alpha^{2N-2}, \tag{5.21}$$

$$M_{2N-1} = \sum_{\alpha=1}^{N} w_\alpha V_\alpha^{2N-1}. \tag{5.22}$$

This nonlinear system of equations can be solved using the Newton-Raphson method or any other method for solving non-linear equations. Nevertheless, this is not the best approach, as a very good initial guess is needed to ensure convergence. The recursive relationship in Eq. (5.11) for orthogonal polynomials is a more efficient method of finding roots. The sequence of recursive relationships with $\alpha = 0, 1, 2, \ldots, N$ can be expressed in matrix form as

$$V \begin{bmatrix} P_0(V) \\ P_1(V) \\ P_2(V) \\ P_3(V) \\ \vdots \\ P_{N-2}(V) \\ P_{N-1}(V) \end{bmatrix} = \begin{bmatrix} a_0 & 1 & & & & & \\ b_1 & a_1 & 1 & & & & \\ & b_2 & a_2 & 1 & & & \\ & & b_3 & a_3 & \ddots & & \\ & & & \ddots & \ddots & \ddots & \\ & & & & \ddots & a_{N-2} & 1 \\ & & & & & b_{N-1} & a_{N-1} \end{bmatrix} \begin{bmatrix} P_0(V) \\ P_1(V) \\ P_2(V) \\ P_3(V) \\ \vdots \\ P_{N-2}(V) \\ P_{N-1}(V) \end{bmatrix} + \begin{bmatrix} 0 \\ 0 \\ 0 \\ 0 \\ \vdots \\ 0 \\ P_N(V) \end{bmatrix}. \tag{5.23}$$

In Eq. (5.23), the roots of $P_N(V)$, namely the nodes of the quadrature approximation V_α, are the eigenvalues of the tridiagonal matrix shown in the equation. By using a diagonal similarity transformation, this matrix can be made symmetric (preserving the eigenvalues)

and to obtain a Jacobi matrix [127]:

$$J = \begin{bmatrix} a_0 & \sqrt{b_1} & & & & & \\ \sqrt{b_1} & a_1 & \sqrt{b_2} & & & & \\ & \sqrt{b_2} & a_2 & \sqrt{b_3} & & & \\ & & \sqrt{b_3} & a_3 & \ddots & & \\ & & & \ddots & \ddots & \ddots & \\ & & & & \ddots & a_{N-2} & \sqrt{b_{N-1}} \\ & & & & & \sqrt{b_{N-1}} & a_{N-1} \end{bmatrix}, \tag{5.24}$$

By this procedure, the ill-conditioned problem of finding the roots of a polynomial is transformed into the well-conditioned problem of finding the eigenvalues and eigenvectors of a tridiagonal symmetric matrix. The N weigths can then be calculated as $w_\alpha = M_0 \varphi_{\alpha 1}^2$, where $\varphi_{\alpha 1}$ is the first component of the αth eigenvector φ_α of the Jaconbi matrix. Two algorithms for efficiently performing these calculations are the Product-Difference (PD) [142] or Wheeler [143] algorithms.
QMOM for integer-order moments was explained here, however, QMOM methods can be generalized to fractional-order moments by introducing a variable change such that the moments are alternatively defined by

$$M_k = M_x/k_s = \sum_{\alpha=1}^{N_V} n_\alpha V_\alpha^{x/k_s}, \tag{5.25}$$

where x is the corresponding integer moment order, k is the fractional moment order, and k_s is the fraction denominator. The general formulation of Eq. (5.25) becomes similar to integer-order formulation when k_s= 1. Typically, the number of quadrature points, N_V, is chosen to be between 2 to 6 for space homogeneous problems, and N_V = 2–3 for multidimensional flow problems [138]. A variation of the QMOM method, with one fixed quadrature at the inception size V_0, is known as a QMOM-Radau method, proposed by Salenbauch et al. [144]. In QMOM-Radau closure, the method of interest here, one volume quadrature point is directly specified, without computation, and held fixed at the inception size, V_0. This approach has also been implemented and suggested in other studies by Mueller et al. [84] and Salenbauch et al. [144]. As a result, the number of moments needed to be solved in this case are then equal to $2NV - 1$. Xing et al. [138] studied soot formation in laminar flames and showed that QMOM-Radau method with three Dirac functions for the fractional-order volume variable (N_V =3) was sufficient to provide accurate predictions of soot volume fraction. Therefore, in this study, the

QMOM-Radau univariate closure using $N_V = 3$ is considered where the model accounts for nucleation, surface growth, oxidation, and agglomeration. The resulting univariate QMOM-Radau closure corresponds to $N_V = 3$ and involves the following five moments: M_0, M_1, M_2, M_3, and M_4. Note that the five-moment QMOM-Radau closure does not provide information regarding aggregate structures and all particles are assumed to be spherical.
The transport equation for the moments of the soot NDF are given as

$$\frac{\partial}{\partial t}(\overline{\rho}\widetilde{M_k}) + \frac{\partial}{\partial x_j}(\overline{\rho}\widetilde{u_j}\widetilde{M_k}) = \frac{\partial}{\partial x_j}\Big[(\overline{\rho}D_s + \frac{\mu_t}{Sc_t})\frac{\partial \widetilde{M_k}}{\partial x_j}\Big] + \overline{\dot{M}_k}, \tag{5.26}$$

and the source terms of the moment transport equation are split into different mechanisms as

$$\overline{\dot{M}_k} = \overline{\dot{M}}_{k,nuc} + \overline{\dot{M}}_{k,sg} + \overline{\dot{M}}_{k,oxid} + \overline{\dot{M}}_{k,coag}. \tag{5.27}$$

These source terms are computed using direct numerical quadrature from the quadrature weights, N_α values, and the quadrature points (abscissa), V_α, obtained from the inversion of the transported moment sets, M_k.

5.5 Models for Soot Physical and Chemical processes

Another aspect of soot modelling is the accurate representation in the mathematical model of various chemical and physical processes leading to soot formation. In this section the different models used for these different processes are explained.

5.5.1 Nucleation

The first step of soot formation is inception or nucleation which is the formation of the first solid particles from the gas-phase chemistry. The acetylene-based nucleation model of Leung et al. [92] introduced in Chapter 3 is considered for soot nucleation and is used for calculating the nucleation reaction rate. The source terms for nucleation step, are given as

$$\dot{M}_{k,nuc} = r_{nuc} V_0^k, \tag{5.28}$$

where r_{nuc} is calculated as

$$r_{nuc} = k_{nuc} \times [\mathrm{C_2H_2}] \times \frac{N_A}{C_{min}}, \tag{5.29}$$

where C_{min}, the number of carbon atoms in the incipient soot particle, is considered 100. Also, V_0, which is the volume of the incipient soot particles, is calculated as

$$V_0 = V_{min} = \frac{C_{min} \times W_c}{\rho_s \times N_A}. \tag{5.30}$$

5.5.2 Surface growth

The initial soot particles (nuclei) created, then grow due to surface reactions. One of the famous models for this process is the hydrogen-abstraction/C_2H_2-addition (HACA) mechanism [77]. Here, surface growth due to acetylene is modelled through the Blanquart and Pitsch [145] version of the HACA mechanism. The source terms for surface growth process, are given as

$$\dot{M}_{k,sg} = \sum_{i=1}^{N_V} r_{sg} S_i n_i \left(V_{sg}^k - V_i^k\right), \tag{5.31}$$

where V_{sg} is calculated as

$$V_{sg} = V_i + dV_{sg}, \tag{5.32}$$

and dV_{sg} is given as

$$dV_{sg} = \frac{2W_c}{\rho_s \times N_A}. \tag{5.33}$$

5.5.3 Oxidation

The oxidation of the soot particles by O_2 is modelled herein using the reaction rate derived by Lee et al. [118]. Reaction rate constants for OH oxidation acting on soot particles are taken from Bradley et al. [146] with assuming a collision efficiency of 0.04 [119, 33]. The source terms for oxidation step, are given as

$$\dot{M}_{k,oxid} = \sum_{i=1}^{N_V} r_{oxid} S_i n_i \left(V_{oxid}^k - V_i^k\right), \tag{5.34}$$

where V_{oxid} is calculated as

$$V_{oxid} = V_i + dV_{oxid}, \tag{5.35}$$

and dV_{oxid} is given as

$$dV_{oxid} = \frac{-2W_c}{\rho_s \times N_A}. \tag{5.36}$$

5.5.4 Coagulation

Considering univariate case for the internal coordinate of the NDF function, the moment source term for coagulation yields [140]

$$\dot{M}_{k,coag} = \int_0^\infty V^k \Big[1/2 \int_0^\infty \beta(V - V')n(V - V')n(V')dV' - \int_0^\infty \beta(V, V')n(V)n(V')dV'\Big]dV \tag{5.37}$$

Since the coagulation kernel $\beta(V)$ depends on V, the RHS of Eq. (5.37) is unclosed. Closure is acheived using the quadrature-based moment method described. Therefore, the coagulation source term can be written in terms of the quadrature nodes and weights as [140]

$$\dot{M}_{k,coag} = \frac{1}{2} \sum_{i=1}^{N_V} \sum_{j=1}^{N_V} n_i n_j \beta(V_i, V_j) \Big[(V_i + V_j)^k - V_i^k - V_j^k\Big]. \tag{5.38}$$

Soot particle formation, transport, and evolution are the result of a complex set physical-chemical processes that includes nucleation, surface growth, oxidation, coagulation, and aggregation. In the five-moment QMOM-Radau closure of interest here, models for all of these processes are incorporated except for aggregation, because the agglomerate structure of soot particles is not accounted for in the uni-variate approach. The influence of this process will be the subject of other future studies. Once the moments are calculated and found, soot volume fraction (f_v) and the total soot number density (N_{total}) are obtained using

$$N_{total} = M_0 = \sum_{\alpha=1}^{N} n_\alpha, \tag{5.39}$$

$$f_v = M_1 = \sum_{\alpha=1}^{N} n_\alpha V_\alpha. \tag{5.40}$$

The flow chart of the CSE-QMOM method is shown in Fig. (5.1).

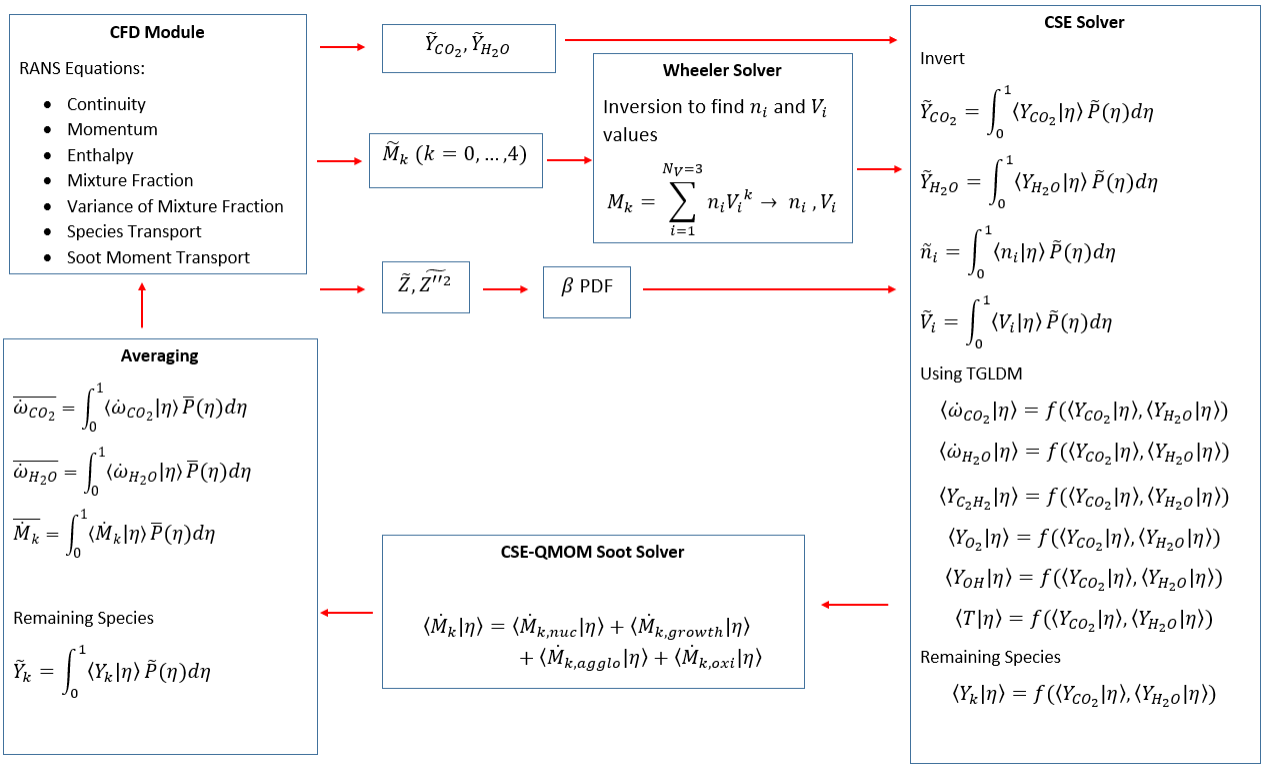

Figure 5.1: CSE-QMOM flowchart diagram

5.6 Burner Configuration and Numerical Setup

The Sandia Ethylene turbulent co-flow flame [17] which is one of the benchmark flames recommended in the International Sooting Flame (ISF) Workshop [95] is considered in the current study for checking the CSE-QMOM method. The experiment data for the Sandia ethylene burner includes soot volume fraction, temperature, OH concentration, PAH radical concentrations, and radiation intensity. This burners simple geometry, well-defined boundary conditions, single-phase pure fuel characteristic, and sufficient data for soot volume fraction, all make it a very good choice for numerical modelling. The burner is shown in Fig. (5.2). A fast-shutter photo of the Sandia ethylene flame is shown in Fig. (5.3). With the 1/1600 s exposure time, the soot-free region is almost invisible but the sooty regions can be seen in orange. The estimated visible flame length is reported 832 mm. Also, another picture showing the complete flame and the experimental setup is given in Fig. (5.4). The configuration and parameters for the Sandia burner are summarized in

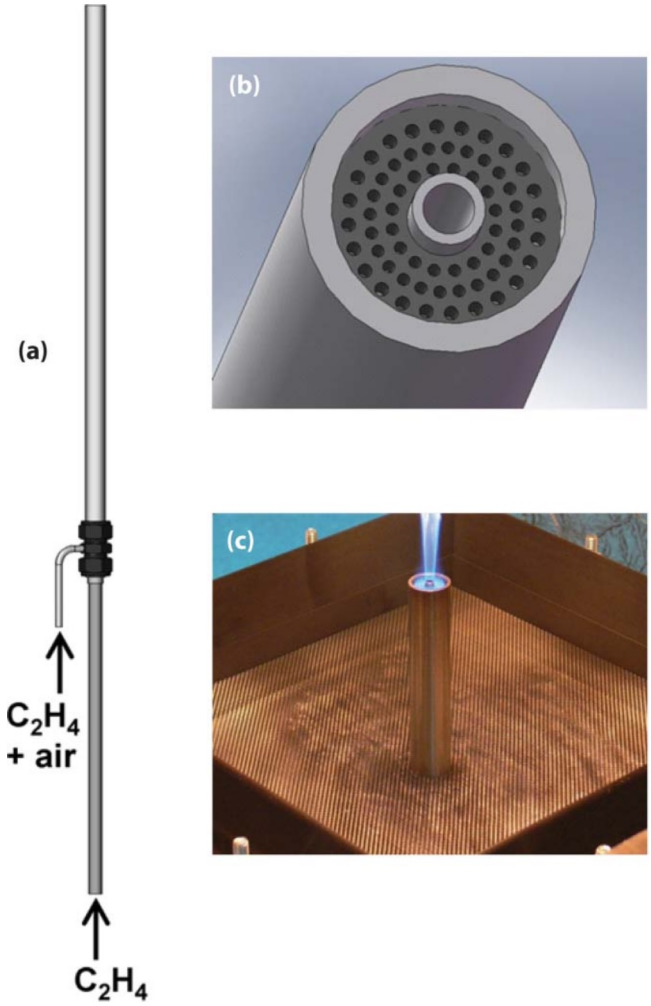

Figure 5.2: The piloted jet burner used for gaseous fuels: (a) drawing of the burner, with the central fuel tube supplying the fuel and the outer coannular tube supplying a premixed fuel-air mixture to an array of small pilot flames; (b) close-up view of the burner exit, showing the fuel tube surrounded by a perforated pilot plate; (c) base of a burning ethylene flame, with pilot flames appearing as small blue cones surrounding the main jet. Reproduced from [17]

Table (5.1). The corresponding two-dimensional axisymmetric computational domain for the Sandia ethylene burner is constructed with an inlet length of 100 mm and the domain extended 1000 mm downstream the nozzle for a total domain length of 1100 mm with a

Figure 5.3: Fast-shutter photograph of Sandia ethylene jet flame with Re=20000. Reproduced from [17]

radius of 150.0 mm. The computational domain is discretized into 81 cells in the radial direction and 700 cells in the axial direction. Also, the inlet pipe section is consisted of 5 $\times$ 60 cells. Therefore, the numerical domain is created of a total of 57,000 computational cells. In this study, the detailed chemical kinetic model developed by Blanquart et al. [148, 149] is used to model the complex gas-phase chemistry. Also, this mechanism takes into account all major pathways of PAH formation which will be used in the next chapter for soot formation modelling using PAH precursors. The mechanism contains 149 species and 1651 reactions (forward and backward reactions counted separately). This chemical mechanism is designed for the high temperature combustion of a wide range of hydrocarbon fuels ranging from methane to iso-octane. The emphasis is placed on developing an accurate model for the formation of soot precursors for realistic fuel surrogates for premixed and diffusion flames.

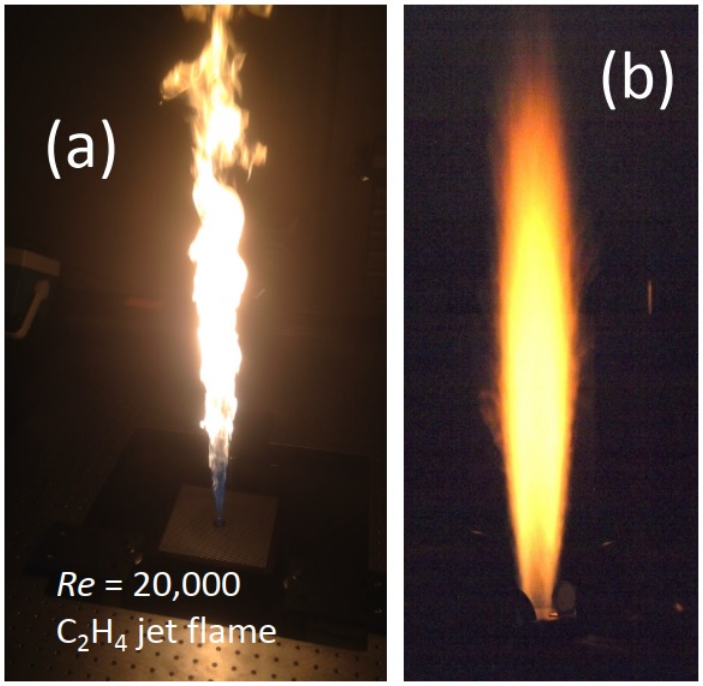

Figure 5.4: Digital photographs of the Re = 20,000 ethylene jet flame. A short-exposure is shown in (a), while a long-time average is shown in (b). Reproduced from [147].

Table 5.1: Burner configuration of the C_2H_4 turbulent jet flame [65].

Fuel jet inner diameter (D_{fi})	0.0032 m	Pilot inner Diameter (D_{pi})	0.0152 m
Fuel jet outer diameter (D_{fo})	0.0045 m	Pilot outer Diameter (D_{po})	0.0191 m
Fuel stream bulk velocity	54.7 m/s	Oxidizer stream bulk velocity	0.6 m/s
Fuel stream inlet temperature	294 K	Oxidizer stream inlet temperature	330 K
Reynolds Number (Re)	20000	Pilot stream bulk velocity	5.75 m/s

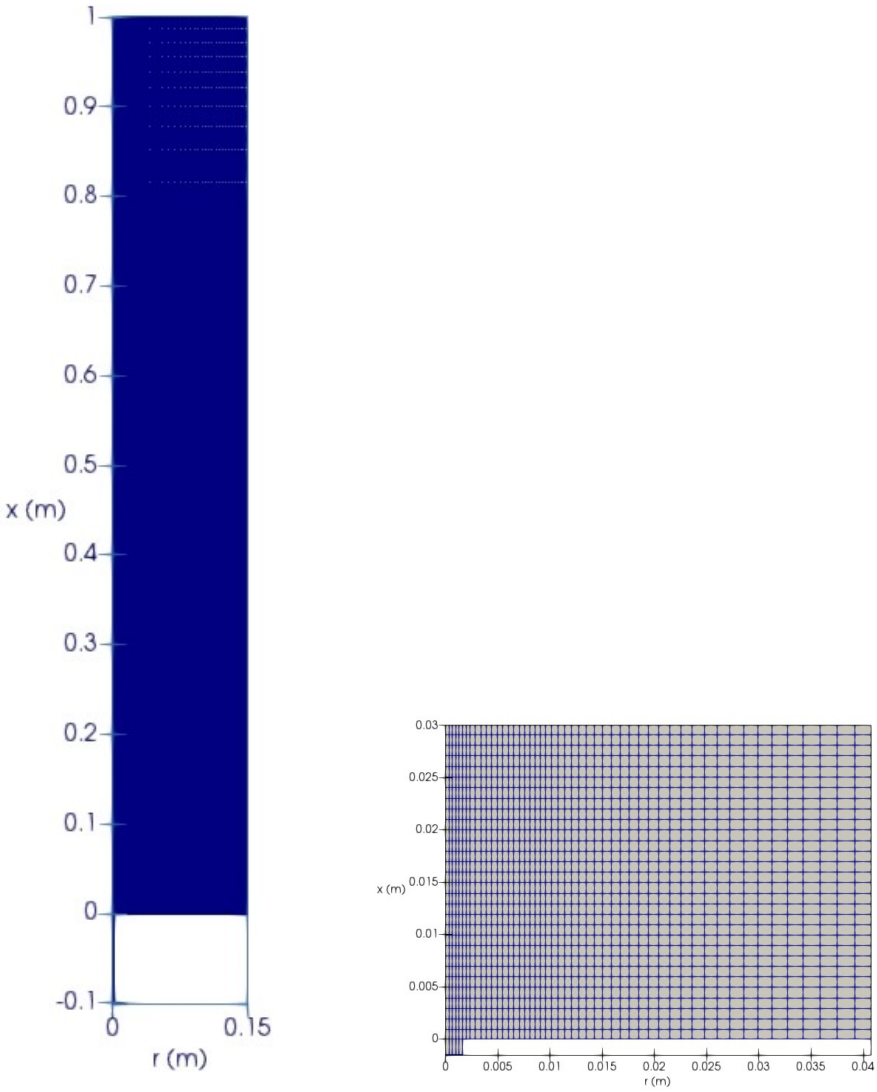

(a) Mesh

(b) Mesh enlarged

Figure 5.5: Images of the computational Mesh. (a) The entire domain (b) Enlarged image of the region close to the burner nozzle.

5.7 Results

Numerical simulation results of temperature and soot volume fraction for the Sandia ethylene burner using five-moment QMOM-Radau quadrature-based moment closures described above, is presented in this section. The CSE-QMOM simulation results are compared along side other results obtained using a standard acetylene based inception model [92] as well as to the available experimental data [65, 95] .

5.7.1 Temperature

Comparison of the predicted temperature with the available experimental results as well as previous simulations have been done. In Fig. (5.6) the centerline temperature is shown. Since the experimental centerline temperature is not given in the literature, the mean temperature predictions along the burner axis are compared with other numerical LES simulations [150, 151]. Radiation resulting from hot gaseous species as well as soot particles is included in the CSE numerical predictions. The other LES studies have also reported that soot and gaseous radiation was captured in their numerical predictions. The CSE peak temperature looks closer to the predictions of Xuan et al. where their peak value is approximately 1800 K and the current CSE predictions give a value of approximately 1750 K. This difference can be attributed to the different radiation model used in the two studies. Also, the predicted peak location is farther downstream compared to the CSE predictions. This may be associated to the turbulence model employed. In the current study the k-ε model with the default constants are used, and since no experimental data for mixture fraction is given, selecting the proper constants to achieve the best results in terms of mixture fraction was not possible. Adjusting the constants of the k-ε model would result in shifting the peak location, the peak temperature, and the width of the flame. Because the predictions of Jain et al. [150], have a peak value of greater than 2000 K, which seems to be a very high temperature for a radiating sooting flame, it might be the temperature without considering radiation. Therefore, the CSE temperature predictions without any radiation, are compared with the predictions of Jain et al. in Fig. (5.7). In Fig. (5.7), it can be seen that the maximum temperatures are approximately the same, although the location of the peak temperature is slightly different. This shows that the values reported in the work of Jain et al. might be the temperature predictions without considering radiation. By comparing the CSE predictions including radiation, Fig. (5.6), and without any radiation, Fig. (5.7) and subtracting the amount of peak temperatures, a difference of approximately 350 K can be observed. This means that the flame will emit a high value of radiative energy through gaseous species and soot, causing the flame tem-

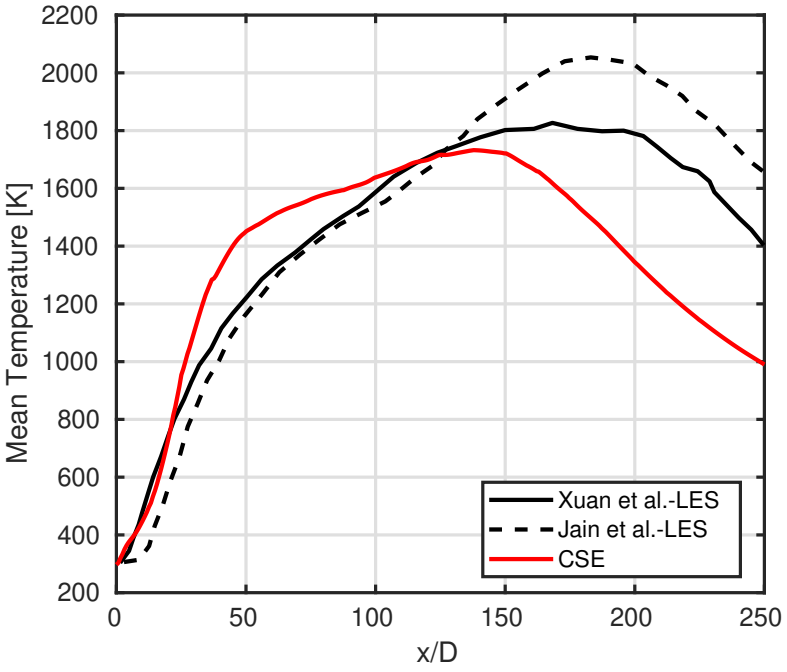

Figure 5.6: Centerline temperature of Sandia ethylene flame. Numerical CSE-QMOM predictions compared with the LES simulation results of Xuan et al. [151] and Jain et al. [150]

perature to decrease almost 350 K.
Moreover, the radial profiles of temperature at different downstream locations are illustrated in Fig. (5.8). No other numerical or experimental results were found for comparing the radial profiles. The only available numerical and experimental data for radial temperature are at the location x/D = 134 mm.

To better validate the temperature predictions, the numerical CSE-QMOM values are compared with the experimental data given at the location x/d = 134. Noting that this is the only experimental temperature profile given for this flame. This comparison is depicted in Fig. (5.9). It can be seen that for this location, the radial predictions of temperature match very well with the experimental data. They have approximately the same values and the trend of numerical profile is pretty similar to the trend of experimental values. The centerline value seems to be a bit higher and the width of the flame looks slightly wider than the experimental flame.

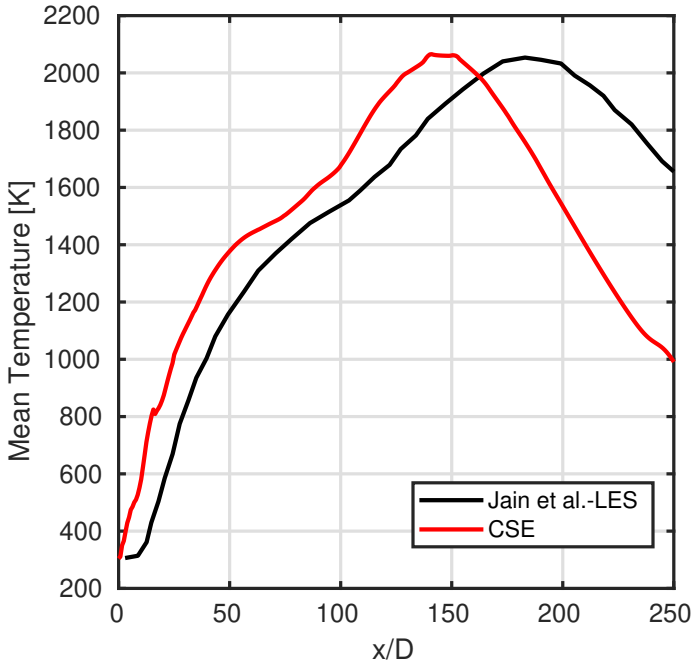

Figure 5.7: Centerline temperature of Sandia ethylene flame without considering radiation. Comparison between CSE numerical predictions and Jain et al. [150] LES numerical predictions.

5.7.2 Soot volume fraction

The centerline soot volume fraction, f_v, obtained from M_1 as given in Eq. (5.40) is compared with the experimental data and shown in Fig. (5.10). The soot distribution in this flame has been mapped via planar LII by Shaddix et al. [10]. It can be seen that the numerical predictions agree well with the experimental data. the peak experimental data is approximately 6.9×10^7 (0.69 ppm), while the maximum numerical predictions using the CSE-QMOM method give a value of approximately 5×10^7 (0.5 ppm) which corresponds to a difference of 27 %. The error reported for the experimental soot volume fraction values is $\sim 20\%$. The discrepancy can be related to the chemistry tables not taking into account the effect of radiation. It was shown in Chapter 4 that by using non-adiabatic tables the predictions can have improvements. Also, the error can be related to the mixing field but because no experimental data was provided for mixture fraction, further comparison is not possible. In Fig. (5.11) the radial profiles of soot volume fraction are shown and compared

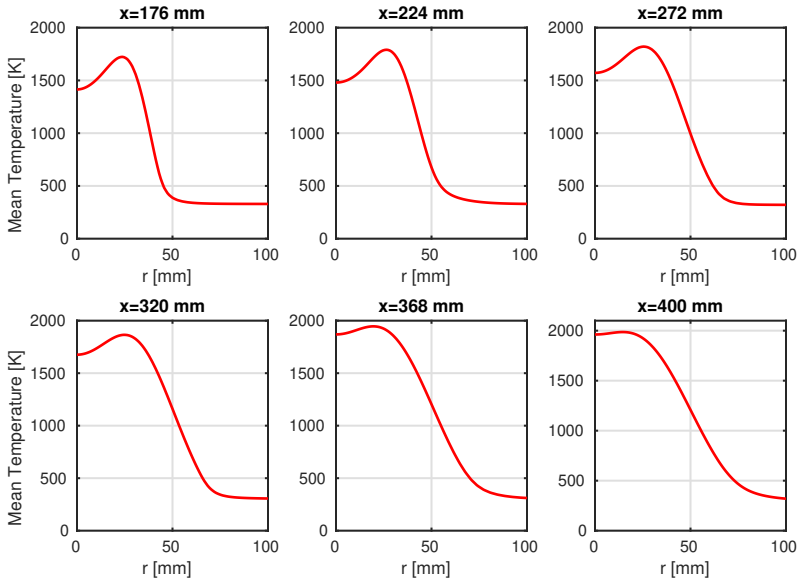

Figure 5.8: Radial temperature profiles at different axial locations

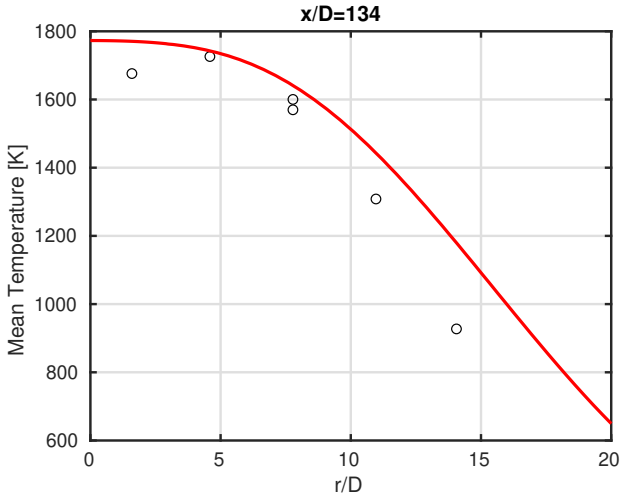

Figure 5.9: Radial temperature profile at axial location x/D=134 compared with experimental data [147]

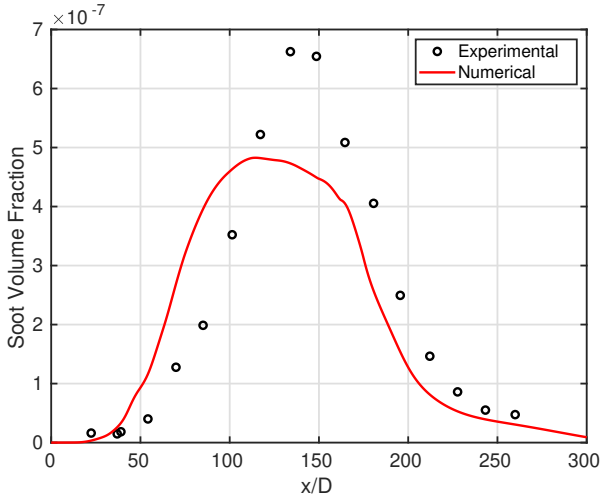

Figure 5.10: Centerline soot volume fraction profile compared with experimental data [152, 95].

with experimental data at different locations [95]. At x = 125 mm, the centerline value is close to the experimental value, but the peak location is lower by approximately 40 % and the peak occurs at a location slightly farther from the centerline (r = 15 mm) compared to the experimental value which occurs at r = 12 mm. At location x = 225 mm, the highest discrepancy is at the centerline where the numerical prediction is larger than the experimental value with a factor of 2.4. The peak value for experimental data occurring at r = 15 mm, is predicted at r = 12 mm and the peak value is over predicted with a discrepancy of 66 %. At x = 425 mm, the peak value occurs at the centerline and the numerical results show an under prediction of 25 % for the centerline value. Also, at x = 575 mm numerical predictions show the peak value of soot volume fraction at the centerline, similar to the experimental data, with an underprediction of approximately 30 %. It can be observed that in all of the radial profiles the soot region is predicted to be wider than the experimental measurements. this can also explain the under prediction of the peak centerline value. Because the soot particles have spread more in the radial direction, the peak value is less than the actual value. But overall, the numerical results show the good capability of the CSE-QMOM method in predicting the soot levels in a turbulent non-premixed sooting flame. Furthermore, the soot volume fraction contour is visualized in the numerical domain as presented in Fig. (5.12). In addition, the experimental instantaneous, mean, and rms soot volume fractions [152] measured by LII imaging in the Sandia ethylene turbulent flame are given in Fig. (5.13). By comparing Figs. (5.12 and 5.13) the size of the soot

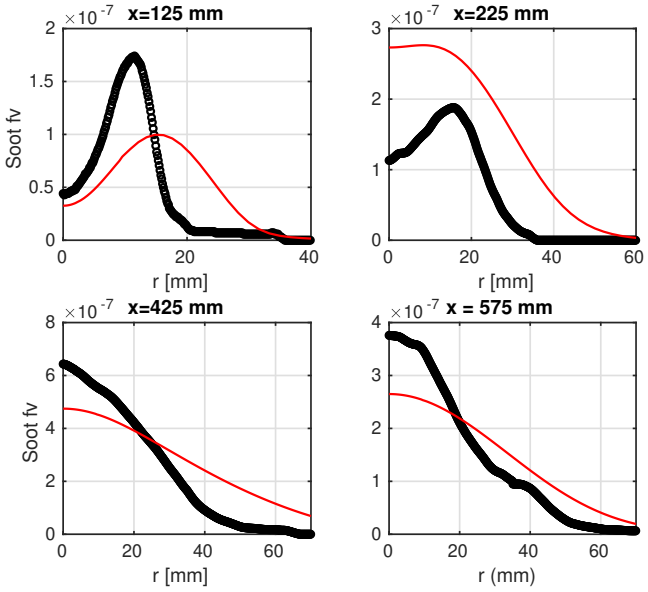

Figure 5.11: Radial soot volume fraction profiles. The black symbols show the experimental value and the red lines show numerical predictions.

region can be compared. In Fig. (5.13), the soot region starts at x = 160 mm and ends at x = 700 mm, whereas for the CSE predictions shown in Fig. (5.12), the start and end point are at 100 mm and 650 mm respectively.

Finally, for comparison of the prediction capability of CSE-QMOM model with CSE-semi-empirical approach, the soot volume fraction predictions obtained from the Leung et al. model [92] are shown and compared with the predictions of the CSE-QMOM method in Fig. (5.14). It can be seen that the semi-empirical model provides lower values of f_v in comparison to the CSE-QMOM method. the peak value is calculated to be approximately 0.3 ppm, with an error of ∼56 %, while the CSE-QMOM predicts a value of approximately 0.5 ppm, with an error of ∼27 %. Also, the location of the peak point is much more closer to the jet nozzle compared to the experimental values and the soot region has finished at x/d =200, while the experimental data show that the soot region extends up to x/d = 250. However, the CSE-QMOM has predicted the sooting region up to x/d = 300 and shows a better match with the experimental data.

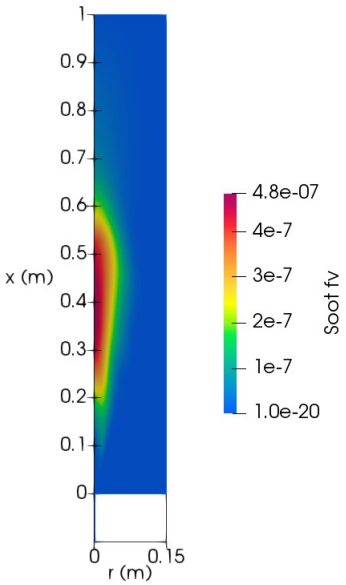

Figure 5.12: Soot volume fraction contours obtained from CSE-QMOM simulation

5.8 Summary

In this chapter, the aerosol dynamics required for soot modelling is described. The method of moments (MOM) and specifically the quadrature method of moments (QMOM) are described. The QMOM method has been implemented in the CSE turbulent combustion approach for the prediction of soot in turbulent flames. The developed CSE-QMOM code is tested on a turbulent ethylene diffusion flame. The numerical predictions show very good agreement with the experimental data. Moreover, the method shows great improvement compared to the semi-empirical soot model presented in Chapter 3.

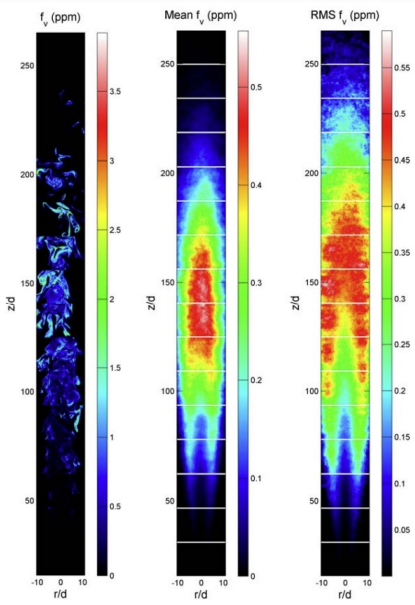

Figure 5.13: Instantaneous, mean, and rms soot volume fractions measured by LII imaging in the Sandia ethylene turbulent non-premixed ethylene jet flame (Re = 20,000). The mean and rms statistics are computed from 500 instantaneous images taken at each height. Taken from [152].

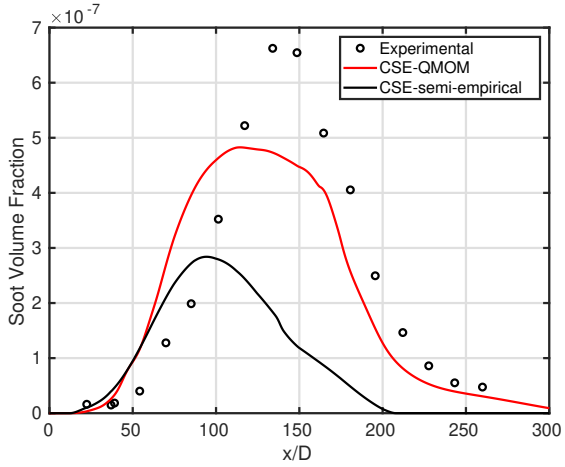

Figure 5.14: Soot volume fraction predictions along the centerline using the CSE-semi-empirical model of Leung et al. [92] compared with the predictions of the CSE-QMOM method.

Chapter 6

PAH precursors for soot nucleation

In Chapters 3, 4, and 5 an acetylene based model for soot nucleation step was considered. In this chapter, soot formation simulation based on Poly cyclic Aromatic Hydrocarbons (PAH) for the nucleation procedure is considered. First, a two-equation model that takes into account the nucleation step based on two and three ringed aromatics is considered. Then, soot formation using moment closure method with a detailed PAH based model with PAH species ranging from naphthalene to cyclo[cd]pyrene as soot precursors is implemented and compared with experimental data and previous predictions from an acetylene-based inception model. The predictions are conducted for the Sandia ethylene-air, turbulent co-flow diffusion flame introduced in Chapter 5. The performance of the PAH-based precursor model is investigated and compared with acetylene-based models.

6.1 Introduction

The inception of soot particles in chemical reacting flows depends on the presence of different chemical species, known as precursors. The existence and formation of these precursors depends on the fuel and flow conditions. Different species have been suggested in the literature to be used as precursors when modelling soot formation in turbulent diffusion flames. In the early studies of soot formation, acetylene was usually selected as the precursor for soot inception. More recent studies have found the relation between soot nucleation and the presence of PAHs. Although pyrene (A4), a four ringed PAH, has been widely used as a precursor in soot models, there is a lack of consensus concerning which PAH species should be used as precursors in order to accurately predict the formation of soot in turbu-

lent flames. In this chapter, two different PAH based models are introduced and coupled with the CSE code to predict soot formation in Sandia turbulent ethylene diffusion flame.

6.2 Two-equation PAH-based soot model

There are various two-equation semi-empirical soot models available which are mostly based on acetylene for the nucleation step. Hall et al. [90] on their study of laminar methane flames, proposed another two-equation semi-empirical model that is based on PAH species. Wen et al. [88] extended this model and used an oxidation model proposed by Lee et al. [118]. In this model the inception (nucleation) step is based on the formation of two-ringed and three-ringed aromatics from single ring aromatic species, as opposed to the Leung et al. model [92] that is a soot inception due to acetylene. The resulting inception model is a function of acetylene (C_2H_2), benzene (C_6H_6), phenyl radical (C_6H_5) and temperature. This model takes into account nucleation, coagulation, growth, and oxidation. The model is similar to the Leung et al. model [92] and solves two equations for soot particle number density (N) and the soot mass density (M). The source terms for N and M are given as

$$\dot{\omega}_N = \dot{\omega}_{N,nuc} + \dot{\omega}_{N,coag}, \tag{6.1}$$

$$\dot{\omega}_M = \dot{\omega}_{M,nuc} + \dot{\omega}_{M,grow} + \dot{\omega}_{M,oxid}, \tag{6.2}$$

where different expressions are available for each of these terms that will be presented in the next section.

6.2.1 Soot nucleation

The nucleation step is based on the formation rates of two and three ringed aromatics ($C_{10}H_7$ and $C_{14}H_{10}$) from acetylene (C_2H_2), benzene(C_6H_6), and phenyl radical (C_6H_5) based on the following reactions

$$2\,C_2H_2 + C_6H_5 \longrightarrow C_{10}H_7 + H_2 \tag{6.3}$$

and

$$C_2H_2 + C_6H_6 + C_6H_5 \longrightarrow C_{14}H_{10} + H + H_2 \tag{6.4}$$

They proposed based on their laminar methane flame data, that the nucleation rate for soot particles would be eight times the formation rate of species $C_{10}H_7$ and $C_{14}H_{10}$ given as

$$\begin{aligned}\dot{\omega}_{N,nuc} = 8.c_2 \frac{N_A}{M_P}\left[\rho^2\left(\frac{Y_{C_2H_2}}{W_{C_2H_2}}\right)^2 \frac{Y_{C_6H_5}W_{H_2}}{W_{C_6H_5}Y_{H_2}}\right] e^{\frac{-4378}{T}} \\ +8.c_3 \frac{N_A}{M_P}\left[\rho^2 \frac{Y_{C_2H_2}Y_{C_6H_6}Y_{C_6H_5}W_{H_2}}{W_{C_2H_2}W_{C_6H_6}W_{C_6H_5}Y_{H_2}}\right] e^{\frac{-6390}{T}},\end{aligned} \tag{6.5}$$

where $c_2 = 127 \times 10^{8.88}$ and $c_3 = 178 \times 10^{9.50}$.
The rate of change of soot mass density is related to the particle number density as

$$\dot{\omega}_{M,nuc} = \frac{M_P}{N_A}\dot{\omega}_{N,nuc}, \tag{6.6}$$

where M_P is the molar mass of soot nucleus, and by considering soot is consisted of 100 carbon atoms [92], it would have a value of 1200 kg/kmol, and N_A is Avogadro's number (6.022045×10^{26} /kmol).

6.2.2 Soot Coagulation

Coagulation of soot particles is caused by their collision with each other. If it is assumed that a collision is completely effective and would lead to joining of the soot particles, then the coagulation rate would be equal to collision frequency. This is specified by the size of particles and the mean free path of the gas surrounding the particles [88]. By assuming that the particles are spherical and mono-dispersed and by using the collision frequency presented by Puri et al. [153] the coagulation rate is given as

$$\dot{\omega}_{N,coag} = -\left(\frac{24R}{\rho_{soot}N_A}\right)^2 \left(\frac{6}{\pi\rho_{soot}}\right)^{1/6} T^{1/2}M^{1/6}N^{11/6}, \tag{6.7}$$

where R is the universal gas constant and $\rho_{soot} = 2000\ kg/m^3$.

6.2.3 Soot surface growth

This source term was based on the work of Frenklach et al. [73] and Harris et al. [154] that showed that the growth of soot particles is mainly by the addition of acetylene. This

term depends on the concentration of acetylene and the active sites on the surface of soot particles, which is a function of the soot surface area. The soot surface growth rate is given as

$$\dot{\omega}_{M,grow} = c_4 \left(\frac{\rho Y_{C_2H_2}}{W_{C_2H_2}}\right) e^{\frac{-12100}{T}} \left[(\pi N)^{1/3} \left(\frac{6M}{\rho_{soot}}\right)^{2/3}\right], \tag{6.8}$$

where $c_4 = 9000.6\ kg.m.kmol^{-1}.s^{-1}$ [88].

6.2.4 Soot oxidation

It is known that OH radical and O_2 are the most important species responsible for soot oxidation. In this model the oxidation rate for OH is taken from Neoh et al. [155] and for O_2 oxidation rate, the expression of Lee et al. [118] is used. Therefore, the soot oxidation rate is given as

$$\begin{aligned}\dot{\omega}_{M,oxid} = -c_5 \eta \rho \frac{Y_{OH}}{W_{OH}} \sqrt{T} (\pi N)^{1/3} \left(\frac{6M}{\rho_{soot}}\right)^{2/3} \\ -c_6 \eta \rho \frac{Y_{O_2}}{W_{O_2}} exp\left(-19778/T\right) \sqrt{T} (\pi N)^{1/3} \left(\frac{6M}{\rho_{soot}}\right)^{2/3},\end{aligned} \tag{6.9}$$

where η is the collision efficiency referring to the fraction of collisions that lead to the complete removal of a single carbon atom and is considered 0.13, $c_5 = 105.81\ kg.m.kmol^{-1}.K^{-1/2}.s^{-1}$, and $c_6 = 8903.51\ kg.m.kmol^{-1}.K^{-1/2}.s^{-1}$.

6.2.5 Soot transport equations

In this model two equations are solved for soot mass density (M) and soot particle number density (N). The general form of the transport equation for any dependent variable is given as

$$\frac{\partial}{\partial t}\left(\overline{\rho}\widetilde{\phi}\right) + \frac{\partial}{\partial x_i}\left(\overline{\rho}\widetilde{u_i}\widetilde{\phi}\right) = \frac{\partial}{\partial x_i}\left(\frac{\mu_t}{Sc_t}\frac{\partial \widetilde{\phi}}{\partial x_i}\right) + \overline{\dot{\omega}}. \tag{6.10}$$

The source terms $\dot{\omega}_N$ and $\dot{\omega}_M$ are calculated based on Eqs. (6.5 - 6.9) and similar to the procedure explained in Chapter 3.

6.2.6 Results

Mean temperature

The profile of mean temperature at the flame centerline is shown in Fig. (6.1). The predictions of previous LES studies of Xuan et al [151]. and Jain et al. [150] are depicted for comparison. It should be noted that the previous LES works are carried out using laminar flamelet/progress variable model and using Direct Quadrature Method of Moments (DQMOM). The CSE-semi-empirical-model using Hall PAH-based inception model has the same trend as the previous LES results up to x/D = 125, but then decreases faster. The peak temperature is approximately 1700 K and the location of the peak occurs at x/D = 140. Also the temperature contours for the Sandia ethylene flame using CSE-semi-empirical-model are shown in Fig. (6.2) and the flame temperature distribution inside the flame can be seen in this figure. The peak temperature is at the centerline and at a height between 400 - 500 mm from the jet nozzle.

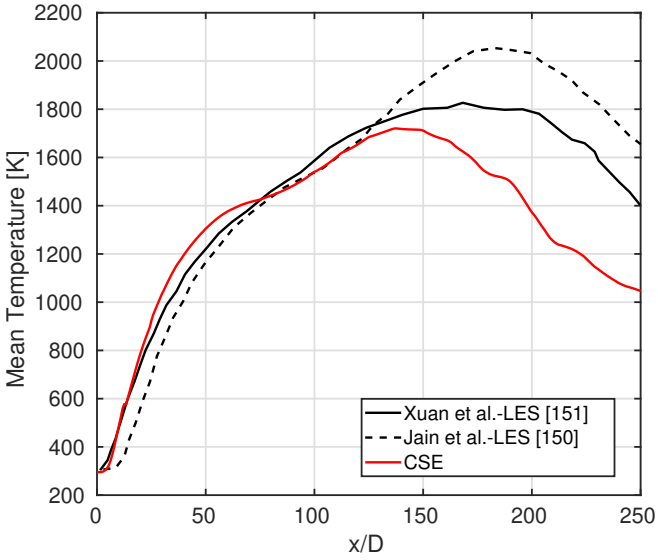

Figure 6.1: Centerline temperature for Sandia turbulent ethylene flame.

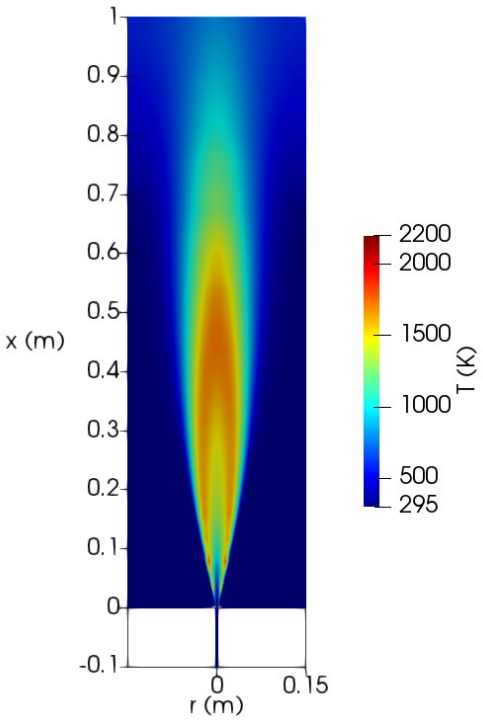

Figure 6.2: Flame temperature distribution in the numerical domain.

Soot volume fraction

The centerline soot volume fraction is shown in Fig. (6.3). It can be seen that the numerical predictions using Hall et al. model give higher values for soot fv than the experimental results by a factor of 1.7 and the peak location is closer to the jet nozzle. The peak soot volume fraction should be at x = 450 mm according to experimental results, while the numerical predictions show the peak at x = 290 mm. In Fig. (6.4) the radial profiles of soot volume fraction are presented for three downstream locations. At x = 125 mm, the numerical predictions show good agreement with the experimental data and the trend of the profile matches well with experimental data. But for locations x = 225 and 425 mm, because a shift exists in the centerline soot volume fraction profile compared with the experimental data, the radial numerical profiles and experimental values do not show good agreement with each other. At x = 425 mm, the CSE-semi-empirical solver shows underprediction for the centerline value approximately 6 times lower. Furthermore, the soot volume fraction region is shown in Fig. (6.5). It can be seen that the soot region starts from x = 100 mm and extends up to x = 400 mm, and therefore a smaller soot region is predicted by this numerical model compared to the xeperimental results. Furthermore, similar to [88], the centerline profile of soot volume fraction is plotted for the case where the inception rate is divided by 8 (Fig. (6.6)). This shows the sensitivity of the predicted soot volume fraction to the inception rate. It can be observed that by removing the factor of 8 in the inception rate, soot volume fraction decreases by a factor of approximately 6. In both cases, the peak soot volume fraction occurs at x = 280 mm, where the experimental peak is located at x = 450 mm. Also, it can be seen that by using the two different inception rates the soot region expands up to x = 420 mm, giving a shorter soot region compare to the experimental data where the soot region exists up to x =800 mm. A shorter sooting region can be related to the soot oxidation constants and also to the temperature field. But because no additional information about the experimental temperature is given, comparison of the temperature at the oxidation region, i.e, the tip of the flame is not possible. In terms of oxidation rate, Hall et al. have used a higher value for OH oxidation than Kronenburg et al. [33]. In the model used by Kronenburg et al. the constant (pre-exponential factor, A) for OH oxidation is 0.36, while the constant used for OH oxidation in Hall et al. model is 13.75 and this leads to higher soot oxidation at downstream locations, and as a result no soot will be observed at downstream locations.

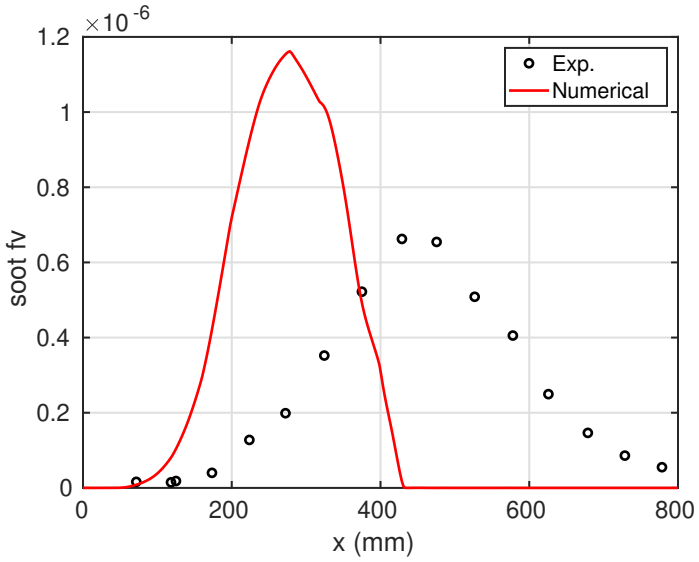

Figure 6.3: Centerline soot volume fraction for Sandia turbulent ethylene flame.

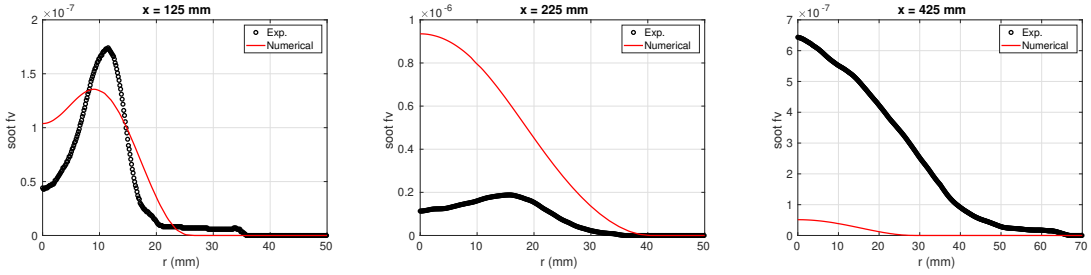

(a) (b) (c)

Figure 6.4: Radial soot volume fraction profiles at (a) x = 125 mm (b) x = 225 mm (c) x = 425 mm compared with experimental results [95, 152]

.

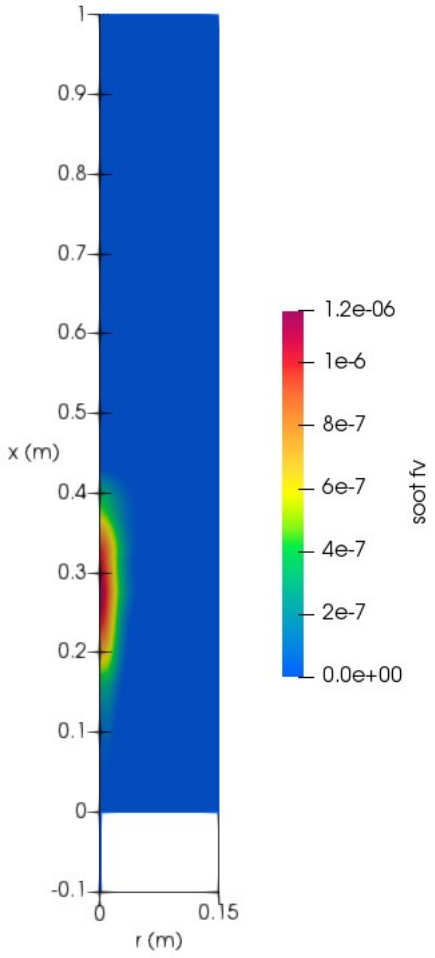

Figure 6.5: Soot volume fraction region inside the numerical domain.

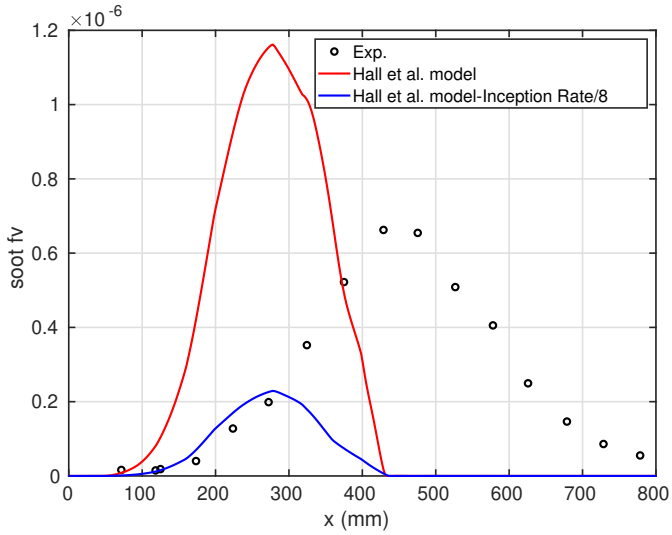

Figure 6.6: Centerline soot volume fraction for Sandia turbulent ethylene flame. Comparison between the predictions using two different inception rates based on the Hall et al. model

6.3 Detailed PAH-based models

In this section another approach for detailed soot modelling using PAH precursors is considered. The model is proposed by Blanquart and Pitsch [156] and considers soot nucleation from the dimerization of PAH species. This model is based on method of moments (MOM) presented in Chapter 5. The source terms used in the moments transport equations for different processes in soot formation and oxidation are explained in the following section.

6.3.1 Nucleation

In the soot model of Blanquart and Pitsch [156], it is assumed that the first soot particle is formed from the collision of two PAH dimers. In the model, dimerization for PAH molecules ranging in size from naphtalene to cyclopental[cd]pyrene is considered. Due to the large concentration of dimers, it is assumed that they either collide with each other or with the existing soot particles. The first case is known as nucleation, while the second case is referred to as condensation (Fig. 6.7).

Nucleation of soot particles is commonly modeled as the collision and subsequent coa-

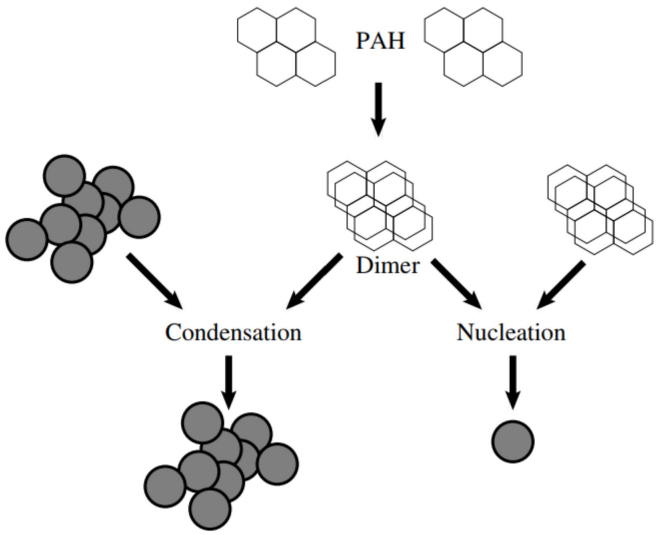

Figure 6.7: Nucleation and condensation of soot from dimers, taken from [157]

lescence of two heavy PAH molecules [157]. The rate of self collisions for a certain type of PAH molecule is given by the kinetic gas theory as [156]

$$\dot{\omega}_{PAH} = \sqrt{\frac{4\pi kT}{m}} d^2 [\mathrm{PAH}]^2, \tag{6.11}$$

where k is the Boltzmann constant, d and m are the molecule diameter and mass respectively. Because the dimer lifetime is very small, the effective rate of dimer formation is much smaller than the value predicted by kinetic gas theory, and a sticking coefficient γ is introduced. The species used for nucleation are given in Table (6.1) with their mass and sticking coefficient.

Also, the diameters of the PAHs are estimated by assuming that PAH molecules are spherical with the density of soot. The effective rate of dimerization of PAH molecules is given by

$$\dot{\omega}_{dimer} = \sum_i \gamma_i \sqrt{\frac{4\pi kT}{m}} \left(\frac{6m_i}{\pi \rho_s}\right)^{2/3} [\mathrm{PAH}_i]^2. \tag{6.12}$$

In the PAH model, the removal of dimers is by nucleation and condensation. The source terms of nucleation and condensation depend on the PAH concentration dimers. The dimer

Table 6.1: List of species used for dimerization with their mass (in amu) and sticking coefficient [157]

Species name	Formula	m_i	γ_i
naphthalene (A2)	$C_{10}H_8$	128	0.0010
acenaphthylene (A2R5)	$C_{12}H_8$	152	0.0030
biphenyl (P2)	$C_{12}H_{10}$	154	0.0085
phenathrene (A3)	$C_{14}H_{10}$	178	0.0150
acephenanthrylene (A3R5)	$C_{16}H_{10}$	202	0.0250
pyrene (A4)	$C_{16}H_{10}$	202	0.0250
fluoranthene (FLTN)	$C_{16}H_{10}$	202	0.0250
cyclo[cd]pyrene (A4R5)	$C_{18}H_{10}$	226	0.0390

concentration can then be calculated as the solution of a quadratic equation as

$$\dot{\omega}_{dimer} = \beta_N[\text{DIMER}]^2 + \left(\sum_{i=1}^{N_V} \beta_{C_i} n_i\right)[\text{DIMER}]. \tag{6.13}$$

By setting Eqs.(6.12) and (6.13) equal, the concentration of dimer, [DIMER], can be obtained. The nucleation source term for the kth moment is given as

$$\dot{M}_{k,nuc} = \frac{1}{2}\beta_N[\text{DIMER}]^2 V_0^k, \tag{6.14}$$

where [DIMER] is the concentration of dimers and β_N is the collision rate of dimers. Also, V_0 is the volume of the smallest soot particles and are defined as the nucleated size. The size of the smallest soot particles is given by

$$V_0 = 2W_C C_{dimer}/\rho_{soot}, \tag{6.15}$$

where W_C is the molar mass of carbon, C_{dimer} is the average number of carbon atoms per dimer, and ρ_{soot} ($= 2000\ kg/m^3$) is the density of soot. The collision rate of dimers occurring in a free molecular regime is given as [158]

$$\beta_N = \epsilon_{nu}\left(\frac{3}{4\pi}\right)^{1/6}\sqrt{\frac{6kT}{\rho_s}}4\sqrt{2}v_d^{1/6}, \tag{6.16}$$

where ϵ_{nu} is an amplification factor due to Van der Waals interactions.

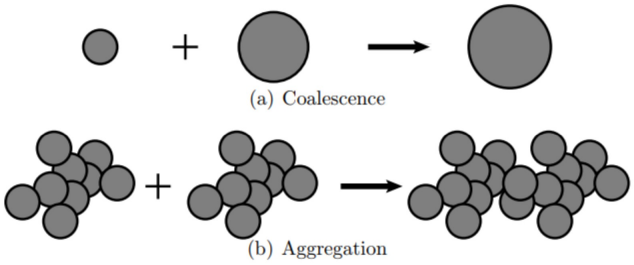

Figure 6.8: Two different cases of coagulation: (a) coalescence, (b) aggregation, taken from [157]

6.3.2 Coagulation

Coagulation is the process of collision of two particles. When the resulting particle from the collision of two smaller particles is a sphere, the coagulation is known as coalescence. But when the colliding particles maintain their original structure, and the resulting particle preserves the structure of the colliding particles, an aggregate is formed. In this case, coagulation is referred to as aggregation [157]. These two different processes are shown in Fig. (6.8). Since a univariate description for soot number density is selected in this study, all soot particles are assumed to be spherical. The rate of coagulation is a function of the size of the particles involved in the collision process. Small particles evolve in the free molecular regime and are characterized with a large Knudsen number (Kn $\gg$ 1). In contrast, large aggregates, evolve in a continuum regime and are characterized by a small Knudsen number. The Knudsen number is defined as the ration of mean free path to the collision diameter ($Kn = \lambda/d_c$). Kazakov and Frenklach [159] proposed expressions for the collision rates for both free molecular and continuum regimes as

$$\beta_{i,j}^{f.m.} = 2.2\sqrt{\frac{\pi kT}{2m_{ij}}}(d_{c_i} + d_{c_j})^2, \tag{6.17}$$

$$\beta_{i,j}^{cont.} = \frac{2kT}{3\mu}\left(\frac{C_i}{d_{m_i}} + \frac{C_j}{d_{m_j}}\right)(d_{c_i} + d_{c_j}), \tag{6.18}$$

where $m_{ij} = m_i m_j/(m_i + m_j)$ is the reduced mass, μ is the dynamic viscosity of the gas, d_{c_i}, d_{c_j} are the collision diameters, and d_{m_i}, d_{m_j} are the mobility diameters. Also, the Cunningham slip correction factor is given as $C_i = 1 + 1.257Kn_i$. Finally, the source terms

for the moments of the NDF for coagulation step are given as

$$\dot{M}_{k,coag} = \frac{1}{2}\sum_{i=1}^{N_V}\sum_{j=1}^{N_V}\beta_{i,j}n_i n_j\left(V_{i+j}^k - V_i^k - V_j^k\right), \tag{6.19}$$

where V_{i+j} is the volume of a newly formed soot particle.

6.3.3 Surface growth

In this model the H-abstraction C_2H_2-addition (HACA) mechanism is used to account for the chemical reactions taking place on the surface of soot particles. The HACA mechanism is consisted of several steps that are shown in Table. (6.2) with the rate constants in the Arrhenius form. The source terms for surface growth process, are given as

$$\dot{M}_{k,sg} = \sum_{i=1}^{N_V} r_{sg}S_i n_i\left(V_{sg}^k - V_i^k\right), \tag{6.20}$$

where V_{sg} is calculated as

$$V_{sg} = V_i + dV_{sg}, \tag{6.21}$$

and dV_{sg} is given as

$$dV_{sg} = \frac{2W_c}{\rho_s \times N_A}. \tag{6.22}$$

6.3.4 Oxidation

Another surface reaction that occurs on the surface of the soot particles is oxidation. The most important species for soot oxidation are known to be O_2 and OH, since they account for most of the soot mass loss [157]. The main product from the process of soot oxidation is carbon monoxide CO. Similar to Chapter 5, here the oxidation of the soot particles by O_2 is modelled herein using the reaction rate derived by Lee et al. [118]. Reaction rate constants for OH oxidation acting on soot particles are taken from Bradley et al. [146]

Table 6.2: Rate coefficients for the surface reactions in Arrhenius form ($k = AT^n exp(-E/RT)$). Units are in cm^3, K, mol, s, and kJ. [157]

Reactions	A	n	E
Soot - H + H $\leftrightarrow$ Soot* + H_2	1.0×10^8	1.80	68.42
	8.68×10^4	2.36	25.46
Soot - H + OH $\leftrightarrow$ Soot* + H_2O	6.72×10^1	3.33	6.09
	6.44×10^{-1}	3.79	27.96
Soot - H $\leftrightarrow$ Soot* + H	1.13×10^{16}	-0.06	476.05
	4.17×10^{13}	0.15	0.00
Soot* + C_2H_2 $\leftrightarrow$ Soot - H	2.52×10^9	1.77	13.54

with assuming a collision efficiency of 0.04 [119, 33]. The source terms for oxidation step, are given as

$$\dot{M}_{k,oxid} = \sum_{i=1}^{N_V} r_{oxid} S_i n_i \left(V_{oxid}^k - V_i^k \right), \tag{6.23}$$

where V_{oxid} is calculated as

$$V_{oxid} = V_i + dV_{oxid}, \tag{6.24}$$

and dV_{oxid} is given as

$$dV_{oxid} = \frac{-2W_c}{\rho_s \times N_A}. \tag{6.25}$$

6.3.5 Results

The centerline soot volume fraction profile is shown in Fig. (6.9). The numerical predictions show very good agreement with experimental data at regions close to the nozzle, but farther downstream underprediction can be seen. The peak location of the soot volume fraction is at x = 400 mm, while the numerical results have predicted the peak at x = 300 mm. The maximum value of soot volume fraction is approximately 0.7 ppm, while the numerical results show a maximum value of 0.2 ppm which corresponds to an error in an order of 2.3. It should be noted that in the current simulations the effect of condensation has not been included and the lower value of soot volume fraction could be related to this process. Also,

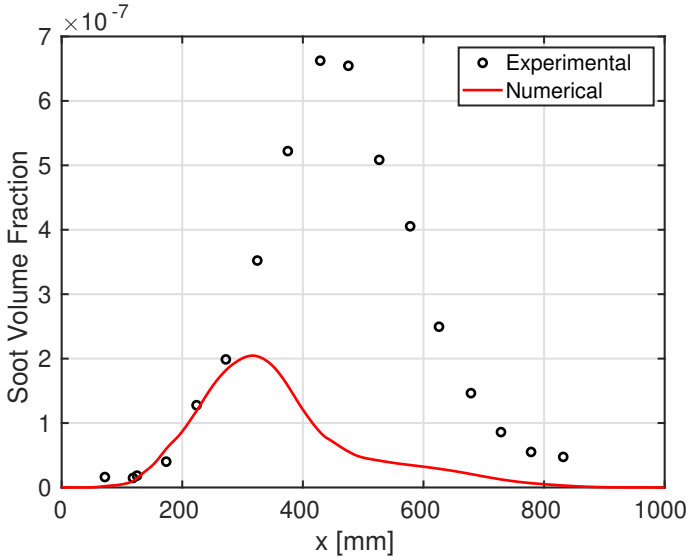

Figure 6.9: Centerline soot volume fraction profile

the mixing field can have an effect on the location of the peak and the value of soot volume fraction. Another important factor is that in this study, soot simulations are done using a univariate description for soot, which is the volume of soot particles. This description does not allow to track the fractal and aggregate shape of soot particles and as a result the soot surface area and the active site for surface reactions are much lower, resulting in lower predictions of soot. Furthermore, the radial profiles of soot volume fraction are shown in Fig.(6.10). It can be seen that the centerline value is well predicted for the first two locations but underpredicted for the last two locations, similar to Fig. (6.9). At x = 125 mm the width of the soot region is larger than the experimental one, the experimental data show soot value up to a radius of 20 mm, while numerical predictions show soot volume fraction up to r = 30 mm. At x = 225 mm the profiles peak is at the centerline, whereas the experimental data have a peak at r = 17 mm. This is due to the fact that this location is close to the numerical peak value for soot volume fraction, and the peak location is expected at the centerline. In addition the soot volume fraction contours are shown in Fig. (6.11). It can be seen that the soot region starts from x = 150 mm and ends at a location of x = 600 mm.

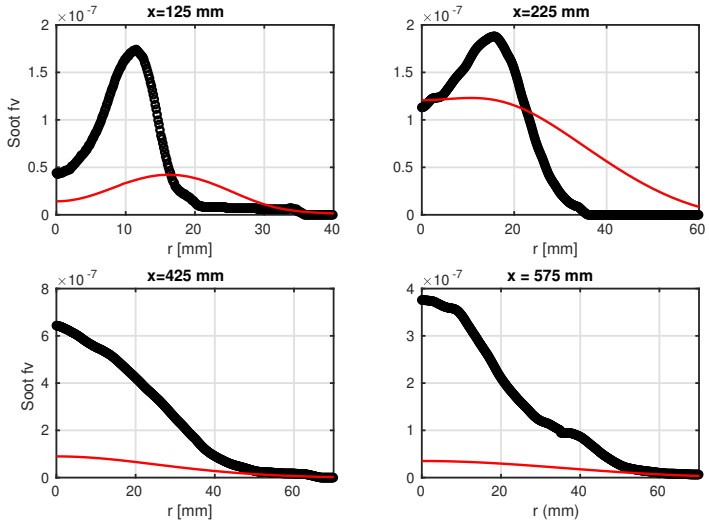

Figure 6.10: Centerline soot volume fraction profile

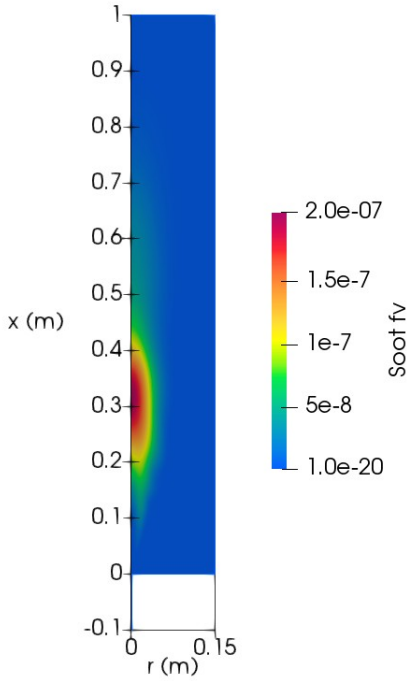

Figure 6.11: Soot volume fraction contours in the numerical domain

6.4 Summary

In this chapter, PAH species are considered as the precursor of soot nucleation. Two different PAH models are presented and coupled with the CSE solver to see the predictions for soot levels in the Sandia turbulent ethylene flame. The first model, is a semi-empirical two equation model from Hall et al. [90] and later presented by Wen et al. [88]. The results of this model show overprediction for the amount of soot volume fraction and also predict the peak location closer to the jet nozzle compared to experimental data. Also, a sensitivity analysis is done for the predicted soot volume fraction to the inception rate. In the first case the original constants of Hall et al. model [90] are used, while in the second case the factor of 8 is removed from the inception model to see the effect of this process on the soot volume fraction. The second PAH model that is coupled with the CSE code is a detailed PAH-based model of Blanquart and Pitsch [156]. This method is based on the moment methods described in Chapter 5. The model is implemented in the CSE framework using a univariate description for soot particles, V. Therefore, all soot particles are assumed to be spherical and the aggregate structure of soot particles is not considered. The results show good agreement with experimental data although some underprediction can be seen for the soot volume fraction. The discrepancies are explained and the possible sources of error are described. Overall, CSE coupled with a PAH-based inception model shows promising results and suggests future work with accounting more details and the usage of bivariate/multivariate descriptions of soot for more accurate predictions.

Chapter 7

Conclusions

The main objective of the present dissertation is to provide an assessment of CSE turbulent combustion method coupled with different soot modelling approaches for predicting soot in turbulent flames. The main findings and conclusions are presented in the current chapter, followed by some recommendations for future work.

7.1 Summary of main findings

In Chapter 3, CSE was coupled with a two-equation semi-empirical model soot model of Leung et al. [92] in order to simulate soot formation in two confined non-premixed turbulent methane flames one operating at atmospheric pressure and another one at 3 atm. The simulations were done using RANS and a modified k-ε model. It was found that a modified value of $C_{\varepsilon 1}$=1.47 would provide good agreement with experimental data for the flames under investigation. Also, it was found that 24 ensembles were sufficient for correctly conducting CSE simulations. The predictions for mixture fraction and temperature were in very good agreement with experimental data for the 1 atm case. The soot volume fraction was also well predicted with some underprediction in the experimental uncertainty range. For the 3 atm flame, the overall temperature predictions were good but overprediction was observed especially at the peak locations. The values of soot volume fraction showed underprediction compared to experimental data. Different sources for error were explained but the main issue seemed to be related to the temperature. Because the temperature was not correctly predicted and the effects of radiation were not included in the tabulated chemistry tables, discrepancies could be observed in the temperature and soot predictions. Furthermore, the amount of radiation, i.e. temperature change, due to gaseous products

and soot were identified for the two flames.

In Chapter 4, the effect of non-adiabatic tables on the temperature predictions and soot values was investigated. Because the flames under investigation, especially the 3 atm flame, was a highly radiating flame, it was necessary to include the effects of radiation into the chemistry tables, that would as a result, provide more accurate species mass fractions, species reaction rates, and temperature values. The method for generating the non-adiabatic TGLDM tables, based on different values of enthalpy, was explained and used for the CSE simulations. The results showed significant improvement for temperature and soot volume fraction predictions and a very good agreement with experimental data.

In Chapter 5, a more detailed soot model, the Quadrature Method of Moments (QMOM), that takes into account soot aerosol dynamics was considered and implemented in the CSE framework. This method solves transport equations for the moments of the population balance equation and closure must be found for the source terms of the moments. the closure problem was solved using quadrature approximation. The Sandia turbulent ethylene diffusion flame which is one of the benchmark flames introduced in the International Sooting Flame (ISF) workshop [95] was selected. This flame has higher values of soot compared to the low sooting flame of methane at 1 atm, and is known as a moderate sooting flame. The predictions of soot volume fraction using the CSE-QMOM method were in very good agreement with experimental data. Also, the simulations were done using the Leung et al. [92] semi-empirical model to compare the two methods in predicting the soot amounts. It was found that the CSE-QMOM provides much better results than the semi-empirical model.

In Chapter 6, Polycyclic Aromatic Hydrocarbons (PAH) based models for soot inception were used and implemented in the CSE code. The previous simulations done in Chapters 3, 4, and 5 were using a conventional acetylene based inception model. In the more recent soot studies, PAH species such as pyrene (A4) are found to have the main contribution in soot formation. Therefore, as a next step for improving the CSE soot model, PAH species were utilized. In order to take into account PAH species with larger carbon contents, the GRI-Mech could no longer be used because it only includes species up to two carbons in their chemical formula. Therefore a new kinetic mechanism, Blanquart et al. mechanism [149] that was designed for PAH formation and includes PAH species up to cyclo[cd]pyrene, was selected and the TGLDM chemistry tables were generated. In the first part of Chapter 6, a semi-empirical soot model, known as the Hall et al. model [90] was selected and coupled

with CSE. Over prediction was observed in the soot volume fraction predictions. In order to see the effect of the inception model and its sensitivity to the values of soot, the factor of 8 included in the inception reaction rate was removed. It was shown that the peak soot volume fraction decreases by approximately a factor of 6. By using the modified Hall et al. model, the predictions for soot volume fraction show better agreement in the region close to the nozzle, but do not reach the peak experimental data with an error of the order 3. In the second part of Chapter 6, the detailed PAH model of Blanquart and Pitsch [156] was selected and implemented in the CSE-QMOM code. The reults for soot volume fraction showed under prediction compared to the experimental data and also predicted the peak value closer to the jet nozzle. The discrepancy could be related to the usage of k-ε model and the inaccuracy of the mixing field, not including PAH condensation in the model, and using a univariate description for soot.

7.2 Summary of accomplishments

A list of the main outcomes is provided here:

- Generating a CSE-soot model for predicting soot in turbulent non-premixed flames and performing numerical simulations for soot formation in Brookes and Moss [15] turbulent methane flames for both 1 atm and 3 atm flames.
- CSE-soot simulations were performed using the generated non-adiabatic chemistry tables to assess the effect of radiation on the chemistry tables. The results showed significant improvement for the case that non-adiabatic tables were used compared to the case were adiabatic ones were utilized.
- The CSE-soot framework was extended to take into account a detailed aerosol model for soot dynamics. The Quadrature-based Method of Moments (QMOM) approach was selected and coupled with the CSE method. The resulting CSE-QMOM code provided very good predictions for soot volume fraction.
- PAH-based soot inception models were added to the CSE-soot and CSE-QMOM frameworks as an improvement for the nucleation submodel used in these codes. The Hall et al. model [90] was added to the CSE-soot model and the Blanquart and Pitsch model [156] model was added to the CSE-QMOM model as a more advanced nucleation step rather than the conventional acetylene based model.

7.3 Future work

This work was done using RANS simulations and some discrepancies in the temperature and soot predictions were likely due to the k-ε model and the mixing field. It would be interesting to carry out the soot simulations in LES to see if the more advanced method would provide better results.

As a first CSE-soot study, all of the soot simulations and modelling were done using a univariate description of soot particles. Recent studies [84, 85, 144] try to use bi-variate or multi-variate descriptions of soot in order to be capable of accounting for aggregate structures of soot. Since the aggregate structures are more likely to occur in non-premixed flames, and the surface area available for soot surface reactions would be much higher, resulting in more accurate soot predictions. Therefore, future studies should include variables such as soot surface area, primary particle diameter, etc. in addition to particle volume.

In this study, methane and ethylene flames were considered. The next step could be performing simulations for more complex/heavier fuels, or liquid fuels that produce more soot and are used in aero engines such as kerosene or Jet A fuels. Also some studies use surrogates representing complex fuels for fuels like diesel. Therefore, spray models should also be coupled in the case of liquid fuels. The simulation of soot formation in these heavy fuels is also of interest.

The soot simulations were done for simple geometries in this dissertation. Simulations could be conducted in practical combustion chambers and engines to assess the models for industrial applications.

The simulations were done up to a pressure of 3 atm. The soot simulations can also be done for higher pressures resembling the pressures that occur in actual engines and combustion chambers.

References

[1] N. Abas, A. Kalair, N. Khan, Review of fossil fuels and future energy technologies, Futures 69 (2015) 31–49.

[2] J. Conti, P. Holtberg, J. Diefenderfer, A. LaRose, J. T. Turnure, L. Westfall, International energy outlook 2016 with projections to 2040, Tech. rep., USDOE Energy Information Administration (EIA) (2016).

[3] V. Manieniyan, M. Thambidurai, R. Selvakumar, Study on energy crisis and the future of fossil fuels, Proc. SHEE 10 (2009) 2234–3689.

[4] T. R. Barfknecht, Toxicology of soot, Prog. Energy Combust. Sci. 9 (1983) 199–237.

[5] N. Kulkarni, N. Pierse, L. Rushton, J. Grigg, Carbon in airway macrophages and lung function in children, N. Engl. J. Med. 355 (2006) 21–30.

[6] M. Z. Jacobson, Strong radiative heating due to the mixing state of black carbon in atmospheric aerosols, Nature 409 (2001) 695.

[7] J. Hansen, L. Nazarenko, Soot climate forcing via snow and ice albedos, Proc. Natl. Acad. Sci. 101 (2004) 423–428.

[8] Z. Mansurov, Soot formation in combustion processes, Combust. Explos. Shock Waves 41 (2005) 727.

[9] S. Gövert, D. Mira, J. Kok, M. Vázquez, G. Houzeaux, Turbulent combustion modelling of a confined premixed jet flame including heat loss effects using tabulated chemistry, Appl. Energ. 156 (2015) 804–815.

[10] J. Appel, H. Bockhorn, M. Frenklach, Kinetic modeling of soot formation with detailed chemistry and physics: laminar premixed flames of c2 hydrocarbons, Combust. Flame 121 (2000) 122–136.

[11] M. Balthasar, M. Frenklach, Detailed kinetic modeling of soot aggregate formation in laminar premixed flames, Combust. Flame 140 (2005) 130–145.

[12] J. W. Labahn, C. B. Devaud, Investigation of conditional source-term estimation applied to a non-premixed turbulent flame, Combust. Theor. Model 17 (5) (2013) 960–982.

[13] J. Labahn, D. Dovizio, C. Devaud, Numerical simulation of the delft-jet-in-hot-coflow (DJHC) flame using conditional source-term estimation, Proc. Combust. Inst. 35 (3) (2015) 3547–3555.

[14] J. Labahn, C. Devaud, Large eddy simulations (LES) including conditional source-term estimation (CSE) applied to two delft-jet-in-hot-coflow (DJHC) flames, Combust. Flame 164 (2016) 68–84.

[15] S. Brookes, J. Moss, Measurements of soot production and thermal radiation from confined turbulent jet diffusion flames of methane, Combust. Flame 116 (1-2) (1999) 49–61.

[16] J. Labahn, Investigation of conditional source-term estimation approach to modelling MILD combustion, Ph.D. thesis, University of Waterloo (2016).

[17] J. Zhang, C. R. Shaddix, R. W. Schefer, Design of "model-friendly" turbulent non-premixed jet burners for C_2+ hydrocarbon fuels, Review of Scientific Instruments 82 (7) (2011) 074101.

[18] T. Poinsot, D. Veynante, Theoretical and numerical combustion, Edwards, 2005.

[19] B. E. Launder, D. B. Spalding, The numerical computation of turbulent flows, in: Numerical prediction of flow, heat transfer, turbulence and combustion, Elsevier, 1983, pp. 96–116.

[20] T. Echekki, E. Mastorakos, Turbulent Combustion Modeling: Advances, New Trends and Perspectives., Springer, 2011.

[21] R. Bilger, S. Pope, K. Bray, J. Driscoll, Paradigms in turbulent combustion research, Proc. Combust. Inst. 30 (1) (2005) 21 – 42.

[22] B. Magnussen, B. Hjertager, On mathematical modeling of turbulent combustion with special emphasis on soot formation and combustion, Symp. (Int.) Combust. 16 (1) (1977) 719 – 729.

[23] D. Spalding, Mixing and chemical reaction in steady confined turbulent flames, Symp. (Int.) Combust. 13 (1) (1971) 649 – 657.

[24] N. Peters, Local quenching due to flame stretch and non-premixed turbulent combustion, Combust. Sci. Technol. 30 (1-6) (1983) 1–17.

[25] R. Cant, E. Mastorakos, An Introduction to Turbulent Reacting Flows, Imperial College Press, 2008.

[26] V. Kuznetsov, Effect of turbulence on the formation of large superequilbrium concentration of atoms and free radicals in diffusion flames, Mehan. Zhidkosti Gasa 6 (1982) 3–9.

[27] F. A. Williams, Turbulent Mixing in Nonreactive and Reactive Flows, Springer New York, 1975, Ch. Recent Advances in Theoretical Descriptions of Turbulent Diffusion Flames, pp. 189–208.

[28] N. Peters, Tubulent Combustion, Cambridge University Press, 2000.

[29] K. Bray, J. Moss, A unified statistical model of the premixed turbulent flame, Acta Astronautica 4 (3) (1977) 291 – 319.

[30] R. W. Bilger, Conditional moment closure for turbulent reacting flow, Phys. Fluids 5 (2) (1993) 436–444.

[31] A. Y. Klimenko, Multicomponent diffusion of various admixtures in turbulent flow, Fluid Dyn. 25 (3) (1990) 327–334.

[32] A. Klimenko, R. Bilger, Conditional moment closure for turbulent combustion, Prog. Energy Combust. Sci. 25 (1999) 595 – 687.

[33] A. Kronenburg, R. Bilger, J. Kent, Modeling soot formation in turbulent methane–air jet diffusion flames, Combust. Flame 121 (1) (2000) 24 – 40.

[34] R. M. Woolley, M. Fairweather, Yunardi, Conditional moment closure modelling of soot formation in turbulent, non-premixed methane and propane flames, Fuel 88 (3) (2009) 393 – 407.

[35] S. B. Pope, Lagrangian PDF methods for turbulent flows, Ann. Rev. Fluid Mech. 26 (1994) 23–26.

[36] S. Pope, PDF methods for turbulent reactive flows, Prog. Energy Combust. Sci. 11 (2) (1985) 119 – 192.

[37] L. Valiño, A field Monte Carlo formulation for calculating the probability density function of a single scalar in a turbulent flow, Flow Turbul. Combust. 60 (2) (1998) 157–172.

[38] V. Sabel'nikov, O. Soulard, Rapidly decorrelating velocity-field model as a tool for solving one-point fokker-planck equations for probability density functions of turbulent reactive scalars, Phys. Rev. E 72 (2005) 163001–163022.

[39] A. Y. Klimenko, S. B. Pope, The modeling of turbulent reactive flows based on multiple mapping conditioning, Phys. Fluids 15 (7) (2003) 1907–1925.

[40] M. Cleary, A. Klimenko, J. Janicka, M. Pfitzner, A sparse-lagrangian multiple mapping conditioning model for turbulent diffusion flames, Proc. Combust. Inst. 32 (1) (2009) 1499 – 1507.

[41] K. Vogiatzaki, A. Kronenburg, M. Cleary, J. Kent, Multiple mapping conditioning of turbulent jet diffusion flames, Proc. Combust. Inst. 32 (2) (2009) 1679 – 1685.

[42] C. Straub, A. Kronenburg, O. T. Stein, G. Kuenne, J. Janicka, R. S. Barlow, D. Geyer, Multiple mapping conditioning coupled with an artificially thickened flame model for turbulent premixed combustion, Combust. Flame 196 (2018) 325 – 336.

[43] S. K. Ghai, S. De, Numerical investigation of flow and scalar fields of piloted, partially-premixed dimethyl ether/air jet flames using stochastic multiple mapping conditioning approach, Combust. Flame 208 (2019) 480 – 491.

[44] H. Steiner, W. K. Bushe, Large eddy simulation of a turbulent reacting jet with conditional source-term estimation, Phys. Fluids 13 (2001).

[45] D. Dovizio, M. Salehi, C. Devaud, RANS simulation of a turbulent premixed bluff body flame using conditional source-term estimation, Combust. Theor. Model. 17 (2013) 935–959.

[46] J. Labahn, C. Devaud, Investigation of conditional source-term estimation applied to a non-premixed turbulent flame, Combust. Theory Model. 17 (5) (2013) 960–982.

[47] D. Dovizio, J. W. Labahn, C. B. Devaud, Doubly conditional source-term estimation (DCSE) applied to a series of lifted turbulent jet flames in cold air, Combust. Flame 162 (5) (2015) 1976 – 1986.

[48] H. Steiner, W. K. Bushe, Large eddy simulation of a turbulent reacting jet with conditional source-term estimation, Phys. Fluids 13 (3) (2001) 754–769.

[49] R. W. Grout, W. K. Bushe, C. Blair, Predicting the ignition delay of turbulent methane jets using conditional source-term estimation, Combust. Theory Model. 11 (2007) 1009–1028.

[50] M. Wang, J. Huang, W. Bushe, Simulation of a turbulent non-premixed flame using conditional source-term estimation with trajectory generated low-dimensional manifold, Proc. Combust. Inst. 31 (2) (2007) 1701 – 1709.

[51] W. Erickson, G. Williams, H. Hottel, Light scattering measurements on soot in a benzene air flame, Combust. Flame 8 (2) (1964) 127–132.

[52] W. Dalzell, G. Williams, H. Hottel, A light-scattering method for soot concentration measurements, Combust. Flame 14 (2) (1970) 161–169.

[53] B. L. Wersborg, J. B. Howard, G. C. Williams, Physical mechanisms in carbon formation in flames, in: Symp. Combust. Proc., Vol. 14, Elsevier, 1973, pp. 929–940.

[54] F. Xu, K.-C. Lin, G. Faeth, Soot formation in laminar premixed methane/oxygen flames at atmospheric pressure, Combust. Flame 115 (1-2) (1998) 195–209.

[55] C. Megaridis, R. Dobbins, Soot aerosol dynamics in a laminar ethylene diffusion flame, in: Symp. Combust. Proc., Vol. 22, Elsevier, 1989, pp. 353–362.

[56] Ü. Ö. Köylü, G. M. Faeth, T. L. Farias, M. d. G. Carvalho, Fractal and projected structure properties of soot aggregates, Combust. Flame 100 (4) (1995) 621–633.

[57] I. Glassman, Soot formation in combustion processes, in: Symp. Combust. Proc., Vol. 22, Elsevier, 1989, pp. 295–311.

[58] I. M. Kennedy, Models of soot formation and oxidation, Prog. Energy Combust. 23 (2) (1997) 95–132.

[59] H. B. Palmer, C. F. Cullis, The formation of carbon from gases, Chemistry and physics of carbon 1 (1965) 265–325.

[60] B. S. Haynes, H. G. Wagner, Soot formation, Prog. Energy Combust. 7 (4) (1981) 229–273.

[61] M. Frenklach, Reaction mechanism of soot formation in flames, Physical chemistry chemical Physics 4 (11) (2002) 2028–2037.

[62] H. Omidvarborna, A. Kumar, D.-S. Kim, Recent studies on soot modeling for diesel combustion, Renewable and Sustainable Energy Reviews 48 (2015) 635–647.

[63] S. Yang, Effects of fuel doping and fuel chemistry on soot formation in co-flow laminar diffusion flames at elevated pressures, Ph.D. thesis, University of Toronto (Canada) (2020).

[64] H. Bockhorn, A short introduction to the problem—structure of the following parts, in: Soot formation in combustion, Springer, 1994, pp. 3–7.

[65] Q. Zhang, Detailed modeling of soot formation/oxidation in laminar coflow diffusion flames, University of Toronto Toronto, Canada, 2009.

[66] K. H. Homann, H. G. Wagner, Some new aspects of the mechanism of carbon formation in premixed flames, in: Symp. Combust. Proc., Vol. 11, Elsevier, 1967, pp. 371–379.

[67] H. F. Calcote, Mechanisms of soot nucleation in flames—a critical review, Combust. Flame 42 (1981) 215–242.

[68] J. A. Miller, C. F. Melius, Kinetic and thermodynamic issues in the formation of aromatic compounds in flames of aliphatic fuels, Combust. Flame 91 (1) (1992) 21–39.

[69] S. E. Stein, J. A. Walker, M. M. Suryan, A. Fahr, A new path to benzene in flames, in: Symp. Combust. Proc., Vol. 23, Elsevier, 1991, pp. 85–90.

[70] R. Kern, K. Xie, Shock tube studies of gas phase reactions preceding the soot formation process, Prog. Energy Combust. 17 (3) (1991) 191–210.

[71] C. F. Melius, M. E. Colvin, N. M. Marinov, W. J. Pit, S. M. Senkan, Reaction mechanisms in aromatic hydrocarbon formation involving the c5h5 cyclopentadienyl moiety, in: Symp. Combust. Proc., Vol. 26, Elsevier, 1996, pp. 685–692.

[72] W. Sun, A. Hamadi, S. Abid, N. Chaumeix, A. Comandini, A comprehensive kinetic study on the speciation from propylene and propyne pyrolysis in a single-pulse shock tube, Combustion and Flame 231 (2021) 111485.

[73] M. Frenklach, D. W. Clary, W. C. Gardiner Jr, S. E. Stein, Detailed kinetic modeling of soot formation in shock-tube pyrolysis of acetylene, in: Symp. Combust. Proc., Vol. 20, Elsevier, 1985, pp. 887–901.

[74] M. Frenklach, D. W. Clary, W. C. Gardiner Jr, S. E. Stein, Effect of fuel structure on pathways to soot, in: Symp. Combust. Proc., Vol. 21, Elsevier, 1988, pp. 1067–1076.

[75] W. Wang, T. Echekki, Investigation of lifted jet flames stabilization mechanism using RANS simulations, Fire Saf. J. 46 (5) (2011) 254–261.

[76] A. E. Karatas, High-pressure soot formation and diffusion flame extinction characteristics of gaseous and liquid fuels, University of Toronto (Canada), 2014.

[77] M. Frenklach, H. Wang, Detailed modeling of soot particle nucleation and growth, in: Symp. Combust. Proc., Vol. 23, Elsevier, 1991, pp. 1559–1566.

[78] M. Frenklach, H. Wang, Detailed mechanism and modeling of soot particle formation, in: Soot formation in combustion, Springer, 1994, pp. 165–192.

[79] M. Balthasar, M. Kraft, A stochastic approach to calculate the particle size distribution function of soot particles in laminar premixed flames, Combust. Flame 133 (3) (2003) 289–298.

[80] F. Gelbard, J. H. Seinfeld, Simulation of multicomponent aerosol dynamics, J. Colloid Interface Sci. 78 (2) (1980) 485–501.

[81] M. Smooke, C. McEnally, L. Pfefferle, R. Hall, M. Colket, Computational and experimental study of soot formation in a coflow, laminar diffusion flame, Combust. Flame 117 (1-2) (1999) 117–139.

[82] M. Frenklach, S. J. Harris, Aerosol dynamics modeling using the method of moments, J. Colloid Interface Sci. 118 (1) (1987) 252–261.

[83] M. Frenklach, Method of moments with interpolative closure, Chemical Engineering Science 57 (12) (2002) 2229–2239.

[84] M. Mueller, G. Blanquart, H. Pitsch, Hybrid method of moments for modeling soot formation and growth, Combust. Flame 156 (6) (2009) 1143–1155.

[85] M. E. Mueller, G. Blanquart, H. Pitsch, A joint volume-surface model of soot aggregation with the method of moments, Proc. Combust. Inst. 32 (1) (2009) 785–792.

[86] S. T. Chong, V. Raman, M. E. Mueller, P. Selvaraj, H. G. Im, Effect of soot model, moment method, and chemical kinetics on soot formation in a model aircraft combustor, Proc. Combust. Inst. 37 (1) (2019) 1065–1074.

[87] S. Brookes, J. Moss, Predictions of soot and thermal radiation properties in confined turbulent jet diffusion flames, Combust. Flame 116 (4) (1999) 486–503.

[88] Z. Wen, S. Yun, M. Thomson, M. Lightstone, Modeling soot formation in turbulent kerosene/air jet diffusion flames, Combust. Flame 135 (3) (2003) 323–340.

[89] P. R. Lindstedt, Simplified soot nucleation and surface growth steps for non-premixed flames, in: Soot formation in combustion, Springer, 1994, pp. 417–441.

[90] R. J. Hall, M. D. Smooke, M. B. Colket, Predictions of soot dynamics in opposed jet diffusion flames, in: F. Dryer, R. Sawyer (Eds.), Physical and Chemical Aspects of Combustion: A Tribute to Irvin Glassman, Gordon & Breach Science Publishers, 1997, pp. 189–229.

[91] M. Bolla, Y. M. Wright, K. Boulouchos, G. Borghesi, E. Mastorakos, Soot formation modeling of n-heptane sprays under diesel engine conditions using the conditional moment closure approach, Combust. Sci. Technol. 185 (5) (2013) 766–793.

[92] K. M. Leung, R. P. Lindstedt, W. Jones, A simplified reaction mechanism for soot formation in nonpremixed flames, Combust. Flame 87 (3-4) (1991) 289–305.

[93] N. Qamar, Z. Alwahabi, Q. Chan, G. Nathan, D. Roekaerts, K. King, Soot volume fraction in a piloted turbulent jet non-premixed flame of natural gas, Combust. Flame 156 (7) (2009) 1339–1347.

[94] A. Coppalle, D. Joyeux, Temperature and soot volume fraction in turbulent diffusion flames: measurements of mean and fluctuating values, Combust. Flame 96 (3) (1994) 275–285.

[95] International Sooting Flame (ISF) Workshop, https://www.adelaide.edu.au/cet/isfworkshop (2019).

[96] H. Steiner, W. Bushe, Large eddy simulation of a turbulent reacting jet with conditional source-term estimation, Phys. Fluids 13 (3) (2001) 754–769.

[97] M. Mortada, C. Devaud, Large eddy simulation of lifted turbulent flame in cold air using doubly conditional source-term estimation, *Combust. Flame* 208 (5) (2019) 420–435.

[98] D. Dovizio, J. W. Labahn, C. B. Devaud, Doubly conditional source-term estimation (dcse) applied to a series of lifted turbulent jet flames in cold air, Combust. Flame 162 (5) (2015) 1976–1986.

[99] D. Dovizio, M. M. Salehi, C. B. Devaud, Rans simulation of a turbulent premixed bluff body flame using conditional source-term estimation, Combust. Theor. Model 17 (5) (2013) 935–959.

[100] W. K. Bushe, H. Steiner, Conditional moment closure for large eddy simulation of nonpremixed turbulent reacting flows, Phys. Fluids 11 (7) (1999) 1896–1906.

[101] S. Pope, U. Maas, Simplifying chemical kinetics: Trajectory-generated low-dimensional manifolds, Mechanical and Aerospace Engineering Report, Ithaca, NY, Report No. FDA (1993) 93–11.

[102] J. Huang, W. Bushe, Simulation of transient turbulent methane jet ignition and combustion under engine-relevant conditions using conditional source-term estimation with detailed chemistry, Combust. Theor. Model 11 (6) (2007) 977–1008.

[103] J. Van Oijen, L. De Goey, Modelling of premixed laminar flames using flamelet-generated manifolds, Combust. Sci. Technol. 161 (1) (2000) 113–137.

[104] S. Girimaji, Assumed β-pdf model for turbulent mixing: Validation and extension to multiple scalar mixing, Combust. Sci. Technol. 78 (4-6) (1991) 177–196.

[105] S. Stårner, R. Bilger, J. Frank, D. Marran, M. Long, Mixture fraction imaging in a lifted methane jet flame, Combust. Flame 107 (3) (1996) 307 – 313.

[106] P. C. Hansen, Numerical tools for analysis and solution of Fredholm integral equations of the first kind, Inverse Probl. 8 (6) (1992) 849–872.

[107] J. W. Labahn, C. B. Devaud, T. A. Sipkens, K. J. Daun, Inverse analysis and regularisation in conditional source-term estimation modelling, Combust. Theory Model. 18 (3) (2014) 474–499.

[108] A. Tikhonov, V. Arsenin, Solution of ill-posed problems, Halsted Press, 1977.

[109] B. Jin, R. Grout, W. K. Bushe, Conditional source-term estimation as a method for chemical closure in premixed turbulent reacting flow, Flow Turbul. Combust. 81 (4) (2008) 563–582.

[110] M. Salehi, W. Bushe, K. Daun, Application of the conditional source-term estimation model for turbulence-chemistry interactions in a premixed flame, Combust. Theory Model. 16 (2012) 301–320.

[111] J. Labahn, C. Devaud, Large eddy simulations (LES) including conditional source-term estimation (CSE) applied to two Delft-Jet-in-Hot-Coflow (DJHC) flames, Combust. Flame 164 (2016) 68 – 84.

[112] P. Smith, D. Golden, M. Frenklach, N. Moriarty, B. Eiteneer, M. Goldenberg, C. Bowman, R. Hanson, S. Song, W. Gardiner, J. V. Lissianski, Z. Qin, GRI-Mech 3.0 (1995).

[113] J. Warnatz, U. Maas, R. Dibble, Combustion: Physical and Chemical Fundamentals, Modeling and Simulation, Experiments, Pollutant Formation, Springer, 2006.

[114] S. Pope, U. Maas, Simplifying chemical kinetics: trajectory-generated low-dimensional manifolds, Tech. rep., Cornell University Report FDA (1993).

[115] J. Ignizio, T. Cavalier, Linear programming, Prentice Hall Int. Series Indust. Sys. Eng. (1994).

[116] A. Hussien, C. B. Devaud, Simulations of turbulent acetone spray flames using the conditional source term estimation (cse) approach, Combust. Theor. Model 25 (2) (2021) 269–292.

[117] R. Renka, Tripack: a constrained two-dimensional delaunay triangulation, ACM Trans. Math. softw. 22 (1996) 1 – 8.

[118] K. Lee, M. Thring, J. Beer, On the rate of combustion of soot in a laminar soot flame, Combust. Flame 6 (1962) 137–145.

[119] R. Puri, R. J. Santoro, K. C. Smyth, The oxidation of soot and carbon monoxide in hydrocarbon diffusion flames, Combust. Flame 97 (2) (1994) 125–144.

[120] https://www.sandia.gov/TNF/radiation.html (2018).

[121] J. F. Widmann, Evaluation of the planck mean absorption coefficients for radiation transport through smoke, Combust. Sci. Technol. 175 (12) (2003) 2299–2308.

[122] OpenFOAM (The open source CFD toolbox) (2022).

[123] B. Launder, B. Sharma, Application of the energy-dissipation model of turbulence to the calculation of flow near a spanning disc, Lett. Heat Mass Trans. 1 (1974) 131–138.

[124] F. MAUSS, K. Netzell, H. Lehtiniemi, Aspects of modeling soot formation in turbulent diffusion flames, Combust. Sci. Technol. 178 (10-11) (2006) 1871–1885.

[125] R. P. Lindstedt, S. A. Louloudi, Joint-scalar transported pdf modeling of soot formation and oxidation, Proc. Combust. Inst. 30 (1) (2005) 775–783.

[126] J. W. Labahn, I. Stanković, C. B. Devaud, B. Merci, Comparative study between conditional moment closure (cmc) and conditional source-term estimation (cse) applied to piloted jet flames, Combust. Flame 181 (2017) 172–187.

[127] D. L. Marchisio, R. O. Fox, Computational models for polydisperse particulate and multiphase systems, Cambridge University Press, 2013.

[128] S. K. Friedlander, et al., Smoke, dust, and haze, Oxford university press, 2000.

[129] P. Mitchell, M. Frenklach, Particle aggregation with simultaneous surface growth, Phys. Rev. E 67 (6) (2003) 061407.

[130] M. Balthasar, M. Frenklach, Monte-carlo simulation of soot particle coagulation and aggregation: the effect of a realistic size distribution, Proc. Combust. Inst. 30 (1) (2005) 1467–1475.

[131] J. Singh, M. Balthasar, M. Kraft, W. Wagner, Stochastic modeling of soot particle size and age distributions in laminar premixed flames, Proc. Combust. Inst. 30 (1) (2005) 1457–1465.

[132] M. Gautier, V. Rohani, L. Fulcheri, Direct decarbonization of methane by thermal plasma for the production of hydrogen and high value-added carbon black, Int. J. Hydrog. Energy 42 (47) (2017) 28140–28156.

[133] S. Kumar, D. Ramkrishna, On the solution of population balance equations by discretization—i. a fixed pivot technique, Chem. Eng. Sci. 51 (8) (1996) 1311–1332.

[134] S. Park, S. Rogak, A novel fixed-sectional model for the formation and growth of aerosol agglomerates, J. Aerosol Sci. 35 (11) (2004) 1385–1404.

[135] D. L. Marchisio, J. T. Pikturna, R. O. Fox, R. D. Vigil, A. A. Barresi, Quadrature method of moments for population-balance equations, AIChE Journal 49 (5) (2003) 1266–1276.

[136] A. Wick, T.-T. Nguyen, F. Laurent, R. O. Fox, H. Pitsch, Modeling soot oxidation with the extended quadrature method of moments, Proc. Combust. Inst. 36 (1) (2017) 789–797.

[137] R. McGraw, Description of aerosol dynamics by the quadrature method of moments, Aerosol Science and Technology 27 (2) (1997) 255–265.

[138] J. Xing, C. Groth, J. Hu, On the use of fractional-order quadrature-based moment closures for predicting soot formation in laminar flames, Combust. Sci. Technol. (2019) 1–23.

[139] C. Chalons, R. Fox, M. Massot, A multi-gaussian quadrature method of moments for gas-particle flows in a les framework, in: Proceedings of the Summer Program, Center for Turbulence Research, 2010, pp. 347–358.

[140] C. Yuan, F. Laurent, R. Fox, An extended quadrature method of moments for population balance equations, J. Aerosol Sci. 51 (2012) 1–23.

[141] C. Yuan, R. O. Fox, Conditional quadrature method of moments for kinetic equations, J. Comput. Phys. 230 (22) (2011) 8216–8246.

[142] R. G. Gordon, Error bounds in equilibrium statistical mechanics, Journal of Mathematical Physics 9 (5) (1968) 655–663.

[143] J. C. Wheeler, Modified moments and gaussian quadratures, Rocky Mt. J. Math. 4 (2) (1974) 287–296.

[144] S. Salenbauch, A. Cuoci, A. Frassoldati, C. Saggese, T. Faravelli, C. Hasse, Modeling soot formation in premixed flames using an extended conditional quadrature method of moments, Combust. Flame 162 (6) (2015) 2529–2543.

[145] G. Blanquart, H. Pitsch, Analyzing the effects of temperature on soot formation with a joint volume-surface-hydrogen model, Combust. Flame 156 (8) (2009) 1614–1626.

[146] D. Bradley, G. Dixon-Lewis, S. Habik, E. Mushi, Twentieth symposium (int.) on combustion (1984).

[147] S. P. Kearney, D. R. Guildenbecher, C. Winters, P. A. Farias, T. W. Grasser, J. C. Hewson, Temperature, oxygen, and soot-volume-fraction measurements in a turbulent c2h4-fueled jet flame, Tech. rep., Sandia National Lab.(SNL-NM), Albuquerque, NM (United States) (2015).

[148] G. Blanquart, P. Pepiot-Desjardins, H. Pitsch, Chemical mechanism for high temperature combustion of engine relevant fuels with emphasis on soot precursors, Combust. Flame 156 (3) (2009) 588–607.

[149] Blanquart et al. Kinetic Mechanism, https://authors.library.caltech.edu/16218 (2022).

[150] A. Jain, Y. Xuan, Effects of large aromatic precursors on soot formation in turbulent non-premixed sooting jet flames, Combust. Theor. Model 23 (3) (2019) 439–466.

[151] Y. Xuan, G. Blanquart, Effects of aromatic chemistry-turbulence interactions on soot formation in a turbulent non-premixed flame, Proc. Combust. Inst. 35 (2) (2015) 1911–1919.

[152] C. R. Shaddix, J. Zhang, R. W. Schefer, J. Doom, J. C. Oefelein, S. Kook, L. M. Pickett, H. Wang, Understanding and predicting soot generation in turbulent non-premixed jet flames, Sand2010-7178, Sandia Report (2010).

[153] R. Puri, T. Richardson, R. Santoro, R. Dobbins, Aerosol dynamic processes of soot aggregates in a laminar ethene diffusion flame, Combust. Flame 92 (3) (1993) 320–333.

[154] S. J. Harris, A. M. Weiner, R. J. Blint, Formation of small aromatic molecules in a sooting ethylene flame, Combust. Flame 72 (1) (1988) 91–109.

[155] K. Neoh, J. Howard, A. Sarofim, Particulate carbon formation during combustion, Plenum 261 (1981).

[156] G. Blanquart, H. Pitsch, A joint volume-surface-hydrogen multi-variate model for soot formation, Combustion generated fine carbonaceous particles (2009) 437–463.

[157] G. Blanquart, Chemical and statistical soot modeling, Ph.D. thesis, Stanford University (2008).

[158] P. Rodrigues, B. Franzelli, R. Vicquelin, O. Gicquel, N. Darabiha, Coupling an les approach and a soot sectional model for the study of sooting turbulent non-premixed flames, Combust. Flame 190 (2018) 477–499.

[159] A. Kazakov, M. Frenklach, Dynamic modeling of soot particle coagulation and aggregation: Implementation with the method of moments and application to high-pressure laminar premixed flames, Combust. Flame 114 (3-4) (1998) 484–501.

Nomenclature

Greek symbols

$\vec{\alpha}$	Conditional-averaged mass fraction vector
$\vec{\alpha}_0$	*a priori* knowledge of the solution $\vec{\alpha}$
β	Temperature exponent/ Coagulation kernel
χ	Scalar Dissipation Rate (1/s)
δ	Dirac delta function
$\Delta h^o{}_{f,k}$	Enthalpy of formation of species k (J/kg)
δ_{ij}	Kronecker's delta
ε	Dissipation rate of the turbulent kinetic energy (m^2/s^3)
η	Mixture fraction sample space/ Soot collision efficiency
γ	Soot sticking coefficient
λ	Regularization parameter/ Thermal conductivity (W/m.K)
μ	Absolute viscosity (Pa.s)
μ_t	Turbulent viscosity (Pa.s)
ν_t	Turbulent kinematic viscosity (m^2/s)

ρ	Density (kg/m^3)
ρ_{soot}	Soot density (kg/m^3)
σ	Stefan-Boltzmann constant (W/m^2.K^4)
σ_b	Boltzmann constant (J/K)
σ_k	Standard k-ε model constant
σ_ε	Standard k-ε model constant
τ_{ij}	Viscous stress tensor (Pa)
$\widetilde{\phi}$	Favre-averaged ϕ
ϕ''	Fluctuation of the Favre-averaged ϕ
$\dot{\omega}_k$	Chemical source-term of species k (kg/m^3.s)
$\dot{\omega}_F$	Fuel mass reaction rate (kg/m^3.s)
$\dot{\omega}_{N_s}$	Soot number density reaction rate (1/m^3.s)
$\dot{\omega}_{Y_s}$	Soot mass fraction reaction rate (kg/m^3.s)

Roman symbols

A	Integrated joint Probability Density Function (PDF) matrix/ The pre-exponential constant
$\vec{b}$	Unconditional averaged mass fraction vector
C_B	Eddy Break-Up model constant
c	Reaction progress variable
C_μ	Standard k-ε model constant
$C_{\varepsilon 1}$	Standard k-ε model constant
$C_{\varepsilon 2}$	Standard k-ε model constant
d	The main fuel jet inlet diameter

D_t	The turbulent diffusivity
$f_{k,i}$	Body force along i acting on species k (N)
$f_{j/i}$	Mass fraction of element j in species i
f_v	Soot volume fraction
h_{abs}	Absolute enthalpy (J/kg)
h_s	Sensible enthalpy (J/kg)
I	Identity matrix
Kn	Knudsen Number
k	Turbulent kinetic energy (m^2/s^2)
$K_{P,i}$	Planck mean absorption coefficient for species i (1/m)
$K_{P,soot}$	Planck mean absorption coefficient of soot (1/m)
Le	Lewis number
M	Number of column in matrix A/ Soot mass density (kg/m^3)
M_k	k^{th} moment of the number density function
M_p	Mass of soot nucleus (kg)
N	Number of rows in matrix A/ number of species/ Number of Dirac delta functions/ Soot particle number density ($1/m^3$)
N_s	Soot particle number density (1/kg)
n_α	Weights of the quadrature approximation
N_A	Avogadro's number (1/mol)
N_V	Number of Dirac delta functions

P	Probability Density Function
p	Pressure (Pa)
P_k	Production term in turbulent kinetic energy transport equation
Pr_t	Turbulent Prandtl number
$\dot{Q}_{rad}$	Heat source-term due to radiation (W)
q_i	Heat flux in i direction (W/m^2)
$\dot{q}_{react}$	Chemical source term of sensible enthalpy equation (W/m^3)
Re	Reynolds number
R	Universal gas constant (J/K.Kmol)
S	Oxidizer-fuel stoichiometric mass ratio
Sc_t	Turbulent Schmidt number
t	Time (s)
Tr	Trace of a matrix
T_A	Activation temperature (K)
u_i	Velocity component in i direction (m/s)
V_α	Abscissas (nodes) of the quadrature approximation
$V_{k,i}$	Diffusion velocity of species k in i direction (m/s)
V_T	Thermophoretic velocity (m/s)
W_k	Molar mass od species k (kg/kmol)
x_i	Spatial component in i direction (m)
Y_k	Mass fraction of species k

Y_F	Fuel mass fraction
Y_O	Oxidizer mass fraction
Y_s	Soot mass fraction
Y_i	Mass fraction of element i in the local mixture
$Y_{i,o}$	Mass fraction of element i in the oxidizer
$Y_{i,f}$	Mass fraction of element i in the fuel
$Y_e(j)$	Mass fraction of element j
Z	Mixture fraction